DUAL SOLVER COMPUTATIONAL MODELING OF SHIP-HELICOPTER DYNAMIC INTERFACE AEROMECHANICS

A Dissertation
Presented to
The Academic Faculty

By

Alex Moushegian

In Partial Fulfillment
of the Requirements for the Degree
Doctor of Philosophy in the
School of Engineering
Department of Aerospace Engineering

Georgia Institute of Technology

May 2022

DUAL SOLVER COMPUTATIONAL MODELING OF SHIP-HELICOPTER DYNAMIC INTERFACE AEROMECHANICS

Thesis committee:

Dr. Marilyn J. Smith
Aerospace Engineering
Georgia Institute of Technology

Dr. Jürgen Rauleder
Aerospace Engineering
Georgia Institute of Technology

Dr. Jonnalagadda V. R. Prasad
Aerospace Engineering
Georgia Institute of Technology

Dr. Susan A. Polsky
Applied Aerodynamics Branch
Naval Air Warfare Center Aircraft Division, Patuxent River

Dr. Glen R. Whitehouse
Co-CEO & Senior Associate
Continuum Dynamics, Inc.

Date approved: April 29, 2022

Dedicated to my mother and father, whose love and sacrifices have made me who I am.

ACKNOWLEDGMENTS

Special thanks are given to the SMART scholarship program for providing funding for tuition and living expenses during the development of this work. Computational resources were provided by the Department of Defense High-Performance Computing Modernization Program (DOD HPCMP) through S/AAA's Roger Strawn, Odessa Murray, and Meghan Goldsborough. The guidance of my advisor, Marilyn Smith; Daniel Wachspress and Glen Whitehouse from Continuum Dynamics; Jennifer Abras from the HPCMP CREATE program; Josh Butler, Eric Hayden, David Farish, Mark Silva, Eric Lynch, and James Forsythe from NAWCAD-PR; and those on my advisory committee is gratefully acknowledged.

TABLE OF CONTENTS

LIST OF TABLES

LIST OF FIGURES

SUMMARY OF NOTATION

a	=	speed of sound
B	=	body force vector
b	=	specific body force vector
C_1, C_2, C_3, C_4	=	Sutherland constants
C_P	=	power coefficient, $\Pi/\left(\rho_\infty n^3 D^5\right)$ for propellers, $\Pi/(\rho_\infty U_{tip}^2 \pi R^3)$ for rotors
C_p	=	pressure coefficient, $(p - p_{ref})/(1/2\rho_{ref} U_{ref}^2)$
C_T	=	thrust coefficient, $T/\left(\rho_\infty n^2 D^4\right)$ for propellers, $T/(\rho_\infty U_{tip}^2 \pi R^2)$ for rotors
cc	=	convergence criterion
D	=	diameter
e_0	=	specific stagnation energy
e_{ijk}	=	Levi-Civita symbol
F	=	force vector
h_0	=	specific stagnation enthalpy
h	=	specific enthalpy
i, j, k	=	data indices
M	=	Mach number
$\boldsymbol{M}$	=	preconditioning matrix
$\hat{n}$	=	normal unit vector
n	=	propeller speed (rotations per second)
p	=	static pressure
Q_c	=	Q-criterion
Q	=	vector of state variables
R_g	=	specific gas constant
R	=	radius

$\hat{r}$	=	radial unit vector
S	=	strain rate tensor
T_{ij}	=	Component i, j of tensor T
T	=	thrust
t	=	time
U	=	velocity magnitude
u	=	velocity vector
u, v, w	=	Cartesian velocity components
v_i	=	i^{th} component of vector v
$\boldsymbol{X}$	=	right eigenvector matrix
x	=	spatial position vector
x, y, z	=	Cartesian coordinates
α	=	angle of attack
β	=	preconditioning factor
Γ	=	total circulation
γ_p	=	ratio of specific heats
γ	=	circulation distribution
δ	=	Kronecker delta
Θ	=	static temperature
θ	=	phase angle
κ	=	thermal conductivity
$\boldsymbol{\Lambda}$	=	eigenvalue matrix
λ_b	=	bulk viscosity
λ	=	eigenvalue
μ	=	molecular viscosity
ν	=	kinematic viscosity

Ω	=	vorticity tensor
ω	=	vorticity vector
Π	=	power
ρ	=	density
σ	=	solidity
ϕ	=	vorticity potential function
τ	=	viscous stress tensor
$\hat{\psi}$	=	azimuthal unit vector

LIST OF ACRONYMS

AAM Advanced Air Mobility
ABL Atmospheric Boundary Layer
ADI Alternating Direction Implicit
AIAA American Institute of Aeronautics and Astronautics
AMR Automatic Mesh Refinement
AUSM Advection Upstream Splitting Method
AV Air Vehicles
BCVE Basic Curved Vortex Elements
BVI Blade-Vortex Interactions
CASTLE® Controls Analysis and Simulation Test Loop Environment
CBC Characteristic Boundary Condition
CDI Continuum Dynamics, Inc.
CFD Computational Fluid Dynamics
CFL Courant–Friedrichs–Lewy
CPF Canadian Patrol Frigate
CPU Central Processing Unit
CREATE™ Computational Research and Engineering Acquisition Tools and Environments
CSD Computational Structural Dynamics
CVC Constant Vorticity Contour
D3ADI Diagonalized Diagonal Dominant Alternating Direction Implicit
DDES Delayed Detached Eddy Simulation
DES Detached Eddy Simulation
DI Dynamic Interface
DIVE Dynamic Interface Virtual Environment
DoD Department of Defense
EFP Elevated Fixed Platform
FPI Force-Predictive Interpolation
GPU Graphical Processing Unit
HFM Helicopter Flight Mechanics
HLLC Harten-Lax-van Leer-Contact
HLLE Harten-Lax-van Leer-Einfeldt
HMB Helicopter Multi-Block
HPC High Performance Computing
HPCMP High-Performance Computing Modernization Program
IGE In Ground Effect

KCFD Kestrel Computational Fluid Dynamics
LBM Lattice Boltzmann Methods
LDA Laser Doppler Anemometry
LDD Limited Directed Difference
LES Large Eddy Simulations
LHA Landing Helicopter Assault
LMP Low Mach Preconditioning
LOIDR Low-Speed Object-Induced Downwash Recirculation
LSWT Low-Speed Wind Tunnel
LU-SGS Lower Upper-Symmetric Gauss Seidel
ML Machine Learning
MS Multi-Scale
NASA the National Aeronautics and Space Administration
NAWCAD-PR Naval Air Warfare Command Aircraft Division - Patuxent River
OGE Out of Ground Effect
PIV Particle Image Velocimetry
PWAM Parallel Wake Analysis Module
PWM Potential Wake Methods
RANS Reynolds-Averaged Navier-Stokes
RCAS Rotorcraft Comprehensive Analysis System
RMS Root-Mean-Squared
SA Spalart-Allmaras
SAS Stability Augmentation System
SGB Single-Gridded-Blade
SGS Sub-Grid-Scale
SHOL Ship-Helicopter Operating Limits
SSOR Symmetric Successive Over-Relaxation
SST Shear-Stress Transport
TVD Total Variation Diminishing
TVF Tip Vortex Filament
UAS Unmanned Aircraft Systems
uRANS unsteady Reynolds-Averaged Navier-Stokes
VF Vortex Filaments
VL Vortex Lattice
VPI Velocity-Predictive Interpolation
VTM Vorticity Transport Methods
VVPM Viscous Vortex Particle Methods
WENO Weighted Essentially Non-Oscillatory
WENOM Weighted Essentially Non-Oscillatory Mapped
WIPP Workshop for Integrated Propeller Prediction
WOD Wind-Over-Deck

SUMMARY

Shipboard landings are a fundamental capability of naval aircraft operations and present a unique challenge to helicopter pilots due to the complex aerodynamic interactions between the ship airwake and the helicopter aerodynamics, known as the Dynamic Interface (DI). As such, detailed analysis and testing must be done to establish the range of safe conditions at which these maneuvers can be performed, as well as to train pilots to perform them. With the advancement of computational power in the last two to three decades, computational tools have been investigated as a way to supplement flight testing for characterization of the DI. Hybrid Computational Fluid Dynamics (CFD) techniques have been developed in recent years with the intent of reducing the cost of rotorcraft CFD simulations through coupling of a uRANS solver with various lower-order computational aerodynamic solvers. Particularly promising for DI applications is the hybrid uRANS/free-vortex wake methodology, which uses uRANS to compute the rotor wake in the near-field and a potential flow model in the far-field. This technique allows wake-body and wake-wake interactions in the DI to be modeled without the need for a highly resolved uRANS domain in the large region between the ship and the helicopter.

This research describes the necessary improvements and extensions of a hybrid uRANS/free-wake solver, OVERFLOW-CHARM, required to accurately characterize DI aerodynamics. These improvements are demonstrated and validated on model problems which include fundamental physics of the DI. First, OVERFLOW-CHARM is applied to analysis of an integrated propulsion system where interactional aerodynamics influence the performance of both the propeller and the wing. Second, OVERFLOW-CHARM is applied to rotors in ground effect, where its capabilities are quantified at a range of rotor scales. This verifies that OVERFLOW-CHARM will be able to accurately capture the interaction of the rotor wake with the ship deck during shipboard landing simulations. Finally, OVERFLOW-CHARM simulations replicating a flight test of the UH-60L helicopter op-

erating within the influence of a model LPD-17 hangar face are performed to investigate OVERFLOW-CHARM's capabilities at capturing LOIDR effects which impact helicopter performance in the dynamic interface.

CHAPTER 1

BACKGROUND AND LITERATURE REVIEW

1.1 Motivation

Following the success of the aircraft carrier for projecting military strength across the globe in World War II, naval aircraft operations have been a key capability of the United States Navy and Coast Guard and have also seen application in civilian ventures and disaster relief efforts. The defining characteristic of these missions is that take-off and landing occurs from a ship deck rather than the conventional airfield runway. Shipboard landing presents a particular set of challenges that must be included in the design of the ship, aircraft, training procedures, and mission guidelines. For shipboard landings of rotorcraft in particular, the complex environment which a pilot must navigate during this difficult maneuver is commonly referred to as the Dynamic Interface (DI) between the rotorcraft and the ship. To characterize the DI, data about the operating environment in shipboard landing scenarios must be gathered, either through full-scale testing, wind-tunnel experiments, or computational modeling. Roscoe and Wilkinson [1] describe in detail the importance of accurate modeling of the DI for naval rotorcraft operational readiness and safety. Testing of the DI by any method is characterized by layers of complexity which must be accounted for to ensure that collected data is accurate and well-informed design decisions can be made [2, 3].

1.1.1 Dynamic Interface Characteristics

The first layer of complexity is the motion of the shipboard due to ocean waves. The aircraft must be able to control its trajectory such that it is able to match the motion of the shipboard upon landing to prevent a strong impact which could damage the landing gear, vehicle, or pilot. While even at the highest levels of analysis fidelity this effect is often neglected due to implementation difficulties, it still drives the need for accurate characterization of ship and aircraft aerodynamics so that robust aircraft control systems can be properly designed. At high Wind-Over-Deck (WOD) speeds in particular, the modeled fidelity of the relative motion between the shipboard and the aircraft significantly impacts a pilot's perception of the quality of simulated landing scenarios [4].

The second layer is the presence of the ship airwake, created by the irregular geometry of the ship superstructure. Even very simple ship geometries produce highly complex flow topologies, as illustrated in Figure 1.1. In general, ship airwakes are characterized by large regions of separation, large-scale turbulent eddies, areas of both high and low frequency unsteadiness, and low speed, high Reynolds number flow. There is a large body of research on the efficacy of various modeling approaches at accurately and cost-efficiently capturing these features of the ship airwake. Full-scale, in-situ experimental methods employ data acquisition techniques such as ship-mounted anemometers [5–8], smoke visualization [9], and, more recently, Unmanned Aircraft Systems (UAS) surveys [10]. Otherwise, wind tunnel models of the ship are utilized with a wider variety of flow measurement techniques including smoke visualization [11–15], helium soap bubbles [11, 12, 15, 16], oil film visualization [17], Particle Image Velocimetry (PIV) [17–20], Laser Doppler Anemometry (LDA) [17], and hot wire anemometry [15, 21–23]. Computational modeling of ship airwakes is generally performed with Reynolds-Averaged Navier-Stokes (RANS) analysis where it has been generally concluded that unsteady techniques are required [24–28] with careful treatment of the low Mach number flow conditions [24]. High wind-over-deck angles and speeds are the most difficult to accurately model [29], and grid resolution in the separated flow region is key [30] where viscous effects play an important role [26, 31] and turbulence models tailored to detached flows should be employed [28, 32, 33]. Small features of the ship superstructure have also been shown to have a non-negligible impact on the airwake characteristics [34–37]. In the DI, the ship airwake creates unsteady inflow

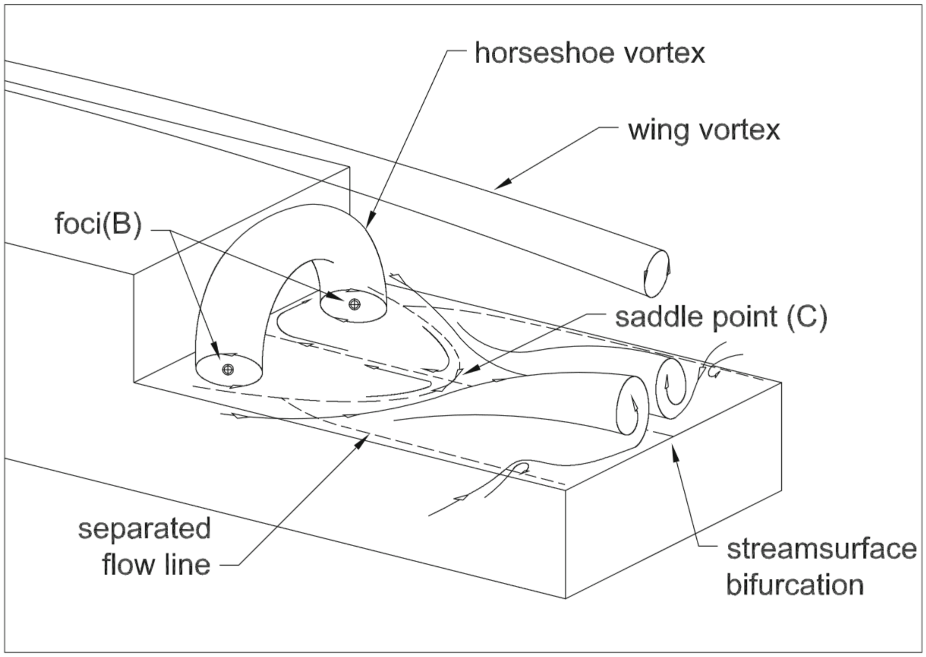

Figure 1.1: Diagram of the flow topology behind a simplified ship geometry [41].

conditions incident on the rotorcraft which impact the required pilot response to maintain a proper trajectory. The ship airwake can also couple with the rotorcraft aerodynamics to produce large deviations in the expected trajectory and significantly increase pilot workload [27, 38–40].

The third layer is the presence of the Atmospheric Boundary Layer (ABL), which develops as a result of the atmosphere's interaction with the sea surface through viscous and thermal phenomena. The ABL includes extremely large-scale velocity gradients and turbulent flow structures which can influence the properties of the ship and aircraft aerodynamics. Wind tunnel and computational modeling of the ABL has determined that it has a moderate impact on the large-scale nature of the ship-airwake, but turbulence present in the ABL does not generally impact the turbulence in the ship airwake, which is dominated by turbulent eddies generated by features of the ship superstructure [12, 16, 36, 42–46]. Figure 1.2 demonstrates the impact of modeling the ABL on ship airwake topology.

Finally, there is a coupling between the ship airwake, ship geometry, and the aircraft wake which becomes increasingly important to model as the aircraft approaches the ship-

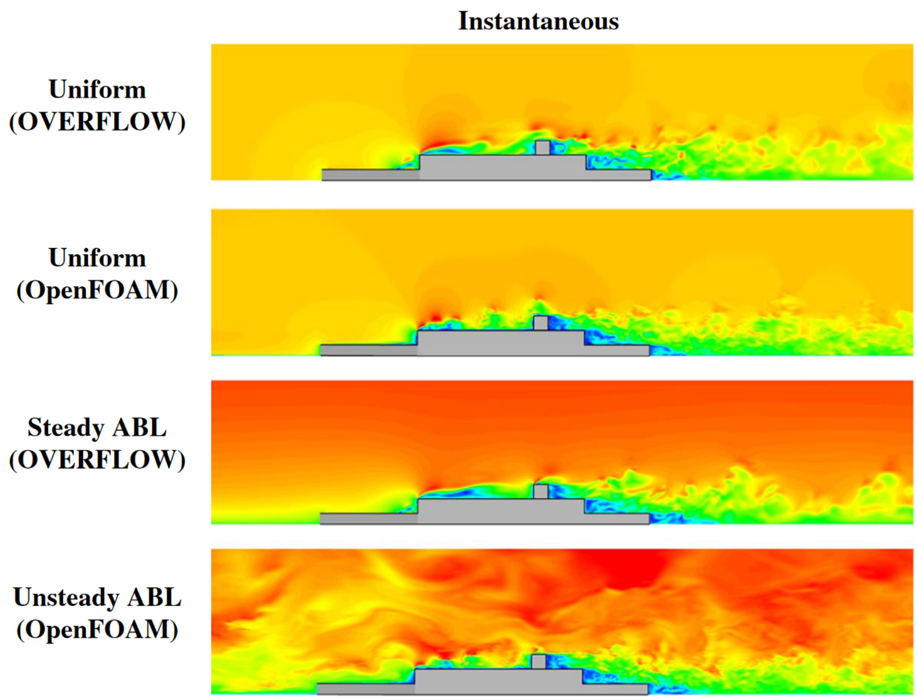

Figure 1.2: Impact of modeling the ABL on ship airwake predictions [44].

board. Rotorcraft in particular exacerbate these issues, as the rotor wake itself is already highly unsteady. The coupling begins with the rotor inflow being influenced by the ship airwake, which impacts the resulting rotor wake. This rotor wake can then impinge on the ship geometry, deflecting and impacting the flow conditions near the rotorcraft. These altered flow conditions then impact the rotor inflow again, including possible re-ingestion of the rotor wake, and the coupling cycle continues. This effect can account for large shifts in the dynamics of the aircraft as it approaches landing, and must be captured if accurate landing dynamics and pilot workloads are to be predicted.

1.1.2 Applications of Dynamic Interface Modeling

All of these layers are condensed into a single set of guidelines for pilots operating in the DI, called the WOD envelope, which gives the set of wind speeds and directions relative to the ship axis where aircraft operations can be safely performed. Figure 1.3 shows a typical WOD envelope. Inadequate testing techniques can lead to either overly conserva-

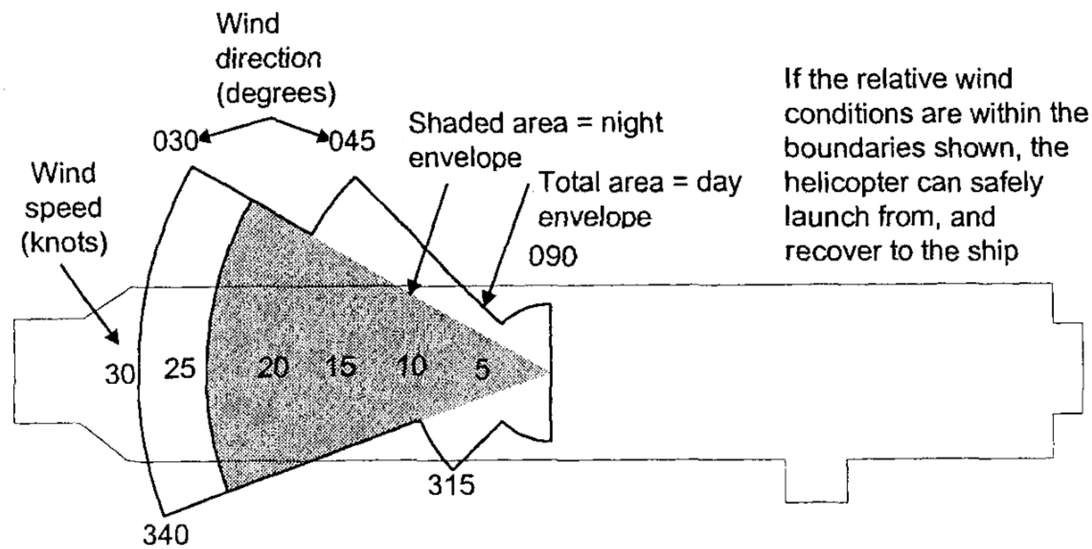

Figure 1.3: A typical wind-over-deck envelope [47].

tive envelopes, limiting operational readiness of the fleet, or overly relaxed restrictions, potentially placing pilots and equipment in danger. Additionally, these envelopes must be generated for every combination of ship and aircraft, meaning that any cost reduction in analysis goes a long way toward rapid approval of new platforms.

Modeling of the DI is also of interest for developing high fidelity flight simulators for pilot training. This provides a safer alternative to in-flight training for new pilots who will be performing shipboard landings. However, the simulation must be as realistic as possible if the training is to translate into improved performance in real operations. Because flight simulations must be performed in real-time, reduced-order models must be developed which accurately capture the vehicle dynamics during all stages of the shipboard landing maneuver. Development of these reduced-order models requires large amounts of high-quality data, so that the analysis technique used to generate the data must strike a fine balance between turn-around time, cost, data density, and modeling fidelity.

1.2 Unified Simulations of the Dynamic Interface

The most basic and physically consistent approach to simulating the DI is to resolve the aerodynamics of the entire system with a unified method. Full-scale testing meets this description and is the current ultimate step when developing WOD envelopes. While full-scale testing provides the closest analog to in-situ DI conditions, it is expensive, time-consuming and difficult to schedule. Also, the full set of operating conditions may not be reproducible during the scheduled test [9, 24]. These factors are indicative of the drawbacks of unified simulation techniques in general. Efforts have been made to model the DI using wind tunnel models of the ship and rotorcraft [48–55]. Lee and Zan correlated aerodynamic loading of the CH-123 Sea King helicopter fuselage to an estimate of pilot workload and generated Ship-Helicopter Operating Limits (SHOL) by varying the relative locations of the helicopter and ship as well as the WOD speed and angle [56]. This work achieves the basic goal of DI modeling to supplement full-scale testing at a reduced cost, however, wind tunnel time is very competitive, so alternative methods must also be explored.

1.2.1 Fully Resolved Navier-Stokes Methods

The highest fidelity computational option for prediction of the aerodynamics of the DI involves the use of Computational Fluid Dynamics (CFD) solvers which solve the unsteady Reynolds-Averaged Navier-Stokes (uRANS) equations on a finite grid of evaluation points. Because uRANS methods resolve the fundamental physics of fluid motion, there is no theoretical limitation to their application to the DI problem. However, due to the large range of time and length scales present in DI flows, a highly resolved computational grid and a very small time step are required to capture the relevant physics. Various simplifications to the uRANS modeling have been attempted, including inviscid and steady-state assumptions [57–59], however, the decreased computational cost did not justify the loss of fidelity in these cases.

Crozon et al. [60] demonstrate the abilities and challenges of tackling the DI problem with a fully-resolved uRANS method when including rotating blades in the computational setup. This study simulated a landing procedure of the Sea King helicopter onto the Canadian Patrol Frigate (CPF) with a resolved-blades uRANS simulation using the Helicopter Multi-Block (HMB) uRANS solver to model the aerodynamics. The motion of the helicopter and the pilot control inputs were modeled through coupling with the Helicopter Flight Mechanics (HFM) code. The study was limited by computational resources to the extent that the computational grid was under-resolved, the time step was fairly large (one degree azimuth of rotor rotation), and aeroelastic modeling was omitted. While the results obtained with this method are promising, it is clear that the computational cost is a limiting factor when applied to practical, repeated analysis.

Actuator Disk/Blade/Line Methods

As demonstrated by the work of Crozon et al., resolution of the rotor blades directly with the uRANS grid is extremely expensive when attempting to simulate the DI due to the small time steps and dense grids the approach requires. One solution to this problem is to use blade-element momentum theory to estimate the blade loads based on the local inflow velocity and communicate their effect using momentum source terms or a pressure jump boundary condition in the uRANS domain.

Actuator disk methods smear the estimated blade loads across the entire rotor disk, which permits steady-state calculations, but fails to capture the helical structure of the rotor wake. Actuator disks have been employed for decades in investigative studies of the DI [40, 57, 58, 61–66]. Crozon et al. [59] compared DI calculations of the Sea King helicopter in the wake of the CPF employing a steady-state actuator disk and time-accurate resolved blades. They found that the actuator disk method was able to capture broad characteristics of the flow field, but missed unsteady effects of the interacting ship and rotor wakes that contribute to pilot workload. Yongjie et al. [67] performed a similar comparison of the

DI between the LPD17 and LHA ships and the Dolphin model helicopter. They found that velocities were predicted within one meter per second between the actuator disk and resolved blades approaches in all areas of the flow field except around the rotor at less than one tenth the computational cost. This indicates actuator disks can be an effective technique when modeling features of the DI such as rotor outwash effects on the flight deck where the near-rotor flow field is not of interest, but are not sufficient when detailed aircraft performance effects of the DI are needed.

Instead of smearing the blade loads across the entire rotor disk, momentum sources can instead follow simulated blade motion in the uRANS solution through the use of actuator blade or actuator line methods. Actuator blade methods distribute the blade forces along the planform of the blade, whereas actuator line methods condense the blade loads onto the quarter-chord line. Both of these methods are able to better capture the unsteady nature of the rotor wake when compared to actuator disk methods, but require time-accurate simulations. Alpman et al. [58] performed DI computations for the UH-60A helicopter in the wake of an Landing Helicopter Assault (LHA) class ship and compared the capabilities of the actuator blade method with those of an actuator disk. They found that the actuator disk showed good agreement for the hovering rotor, but was not able to model blade azimuthal, flapping, or lead-lag motion, whereas the actuator blade did have this capability. Polsky [64] quantified the additional cost incurred by the need to resolve rotor blade motion in actuator blade methods, with such simulations requiring a ten-fold decrease in the time step compared to an actuator disk method. Forsythe et al. [38] simulated the DI using Controls Analysis and Simulation Test Loop Environment (CASTLE®), a flight dynamics tool, to predict the motion of a generic “Example Helicopter” loosely based on the UH-60A airframe with the aerodynamics in the DI predicted using High-Performance Computing Modernization Program (HPCMP) Computational Research and Engineering Acquisition Tools and Environments (CREATE™)-Air Vehicles (AV) Kestrel to manage the uRANS solution. While the ship airwake and fuselage aerodynamics are predicted directly by the uRANS solver, blade aerodynamic modeling is simplified through coupling with the blade-element model in CASTLE®. This treatment of the blades loosens the restriction on the physical time step in the simulation compared to fully-resolved blades, but sacrifices the ability to capture three-dimensional and interactional aerodynamics and is unable to predict the helical structure of the rotor wake. The simulated landing scenario took five days on 384 processors, indicating that full computations of the DI are still extremely expensive for state-of-the-art uRANS methods. Oruc et al. [68] present results using a very similar methodology with a larger time step and coarser computational grid, though computational cost is still too restrictive for most applications. Linton and Thornber [69] present an actuator surface method for DI simulations, which is similar to an actuator line method with a more advanced determination of the blade-element inflow velocity based on a potential flow model of the rotor wake. Both the actuator line momentum sources and potential wake model are coupled to the uRANS solution which resolves the ship airwake and rotor wake interactions. While computational cost savings are comparable with other actuator line methods, quantification of the accuracy of DI simulations employing this method has yet to be performed. All of these methods make two-dimensional, steady-state assumptions when converting the local inflow velocity to blade sectional forces, and there is some ambiguity in the interpretation of the local uRANS flow field as a single inflow velocity, especially when coupling via source terms.

1.2.2 Lattice Boltzmann Methods

Rather than solve the continuity equations for a continuous medium on a grid as in continuum-based Navier-Stokes methods, Lattice Boltzmann Methods (LBM) track particle velocities in a lattice by computing their advection and collisions through a distributed probability density function. These methods are more easily parallelizable than continuum-based methods, which in the future may allow for very fast turn-around times on Graphical Processing Unit (GPU) architectures. LBM have been used to compute coarse rotor wakes in the influence of ship superstructures [70, 71] using actuator disk models of the rotor aerodynamics. However, viscous wall boundary conditions in LBM are non-trivial, and thus require immersed boundary treatment where adaptive grid refinement techniques tend to create very small cells in the viscous boundary layer [72]. Thus, for cases with large and complicated solid bodies such as shipboard landing scenarios, the size of the computational grid can grow to billions of points. If the rotor blades are resolved, the frequency of grid adaptation will also be quite high. Additionally, accurate turbulence modeling in LBM requires similar levels of grid refinement as continuum-based uRANS methods [73]. Also, the presence of compressibility effects in the rotor wake requires a higher-order formulation of the LBM equations, increasing the cost compared to the more common "weakly compressible"/"essentially incompressible" LBM formulation [74]. Finally, the primary advantage of LBM methods, namely the ease of parallelization, cannot be utilized unless sufficient GPU resources are available and the method is written in the proper code format, neither of which are widespread at the time of writing. While promising for future study, the demand for cost savings on contemporary computing hardware means that alternative methods to LBM need to be explored.

1.2.3 Potential Flow Methods

With the assumption of inviscid and irrotational flow, the Navier-Stokes equations can be simplified to the potential flow equations which can be solved very efficiently, with some analytical solutions existing for simple flows. Within this formulation, the lift generated by a body can be transformed into a spanwise circulation distribution, which is then shed into the wake in a variety of ways, including as a sheet of horseshoe vortices, a Vortex Lattice (VL), or as Vortex Filaments (VF). A horseshoe vortex method is a lifting line formulation which involves segmenting the lifting body into a series of horseshoe vortices which trail infinitely behind the body and are connected by a small vortex segment on the body surface. The strength of each segment is based on the lift distribution along the span of the body. A

VL method models the lifting body as a series of lifting panels, each with a corresponding horseshoe vortex and a bound vortex. As the simulation progresses, these panels can be released into the wake of the body to model the shed vorticity, where they can be convected and deformed according to the freestream velocity and combined induced velocity due to all vortices in the simulation. A VF method assumes that all vorticity in the flow field is concentrated in vortex filaments with a singularity at the center of the filament. These filaments are shed from various locations along the body, usually from the root and tip of a wing or rotor blade. A so-called "full-span" VF method generates filaments along the entire span of the lifting body based on the circulation distribution over the span. More discussion on these three methods are provided by the National Aeronautics and Space Administration (NASA) [75], and particularly Bliss et al. [76], who describe the implementation of the free-vortex wake model leveraged in this research. While the derivation of potential flow methods makes an inviscid assumption, viscous dissipation can be approximated post-hoc using corrections to the vortex wake models. Potential flow models are most readily applied to fixed-wing and rotorcraft wake prediction due to the predictable shedding of vorticity at the wing or blade trailing edge. However, because the production of vorticity is primarily a viscous effect for these applications, circulation distributions must be prescribed or modeled using algebraic or experimental data fitting methods, which can miss the higher-order aerodynamic effects present in rotor wakes, especially. Preliminary work has applied a free-vortex wake model to DI predictions, however the complexity of the ship geometry and flow field makes this a particularly difficult challenge, as again, the production of vorticity by the ship superstructure must be modeled separately and prescribed in the potential flow solver [77].

1.3 One-Way Coupled Simulations of the Dynamic Interface

To address the extreme cost of unified computational DI simulations, it is common for investigators to decouple simulations into two separate problems. The first is the prediction of the ship airwake, which is nearly universally performed using computational fluid dynamics methods due to the complex nature of the geometry and flow field. It is then common to extract a time history of the flow field at a set of evaluation points and use them to influence a separate computation of the rotorcraft aerodynamics. This approach circumvents the need to update the ship airwake at the small time scales required to capture the motion of the rotor blades, but sacrifices resolution of the full two-way coupling between the aerodynamics of the ship and rotorcraft. Depending on the method, the aerodynamic interactions between the rotor wake, ship wake, and ship superstructure can still be modeled in a one-way coupled simulation. Bridges et al. [40], compared one-way and two-way coupling between a uRANS solver and a flight dynamics solver and found that one-way coupled simulations were sufficient to characterize pilot workload, especially when the rotor wake was convected away from the rotorcraft. Accurate pilot response in this framework is still a concern, however, particularly for flight simulation applications [58]. Assuming the ship airwake has been precomputed, the following sections will describe various approaches to the further modeling required to build up a DI computation.

1.3.1 Flight Dynamics Models/Flight Simulators

Flight dynamics models and flight simulators are optimized for real-time applications and thus tend to use relatively simple models of rotorcraft aerodynamics. Therefore, it is easy to incorporate the effect of the ship airwake into these methods. This approach to simulating the DI has been extensively studied for the last 3 decades and is characterized by the primary advantage of real-time simulation capability. However, this method cannot predict aerodynamic coupling due to the presence of the ship in the simulation, including aerodynamic coupling between the rotor wake and the ship airwake and the influence of the ship superstructure on the rotor wake. This results in discrepancies as the rotorcraft approaches the shipboard and completely fails to capture rotor wake reingestion effects, which can have a significant influence on handling qualities. While there have been many studies of this methodology in the literature [39, 58, 78–87], Polsky et al. [88] describe the implementation of DI effects into a flight simulator. Time-accurate ship airwake data is pre-computed with the Cobalt uRANS solver using the MILES turbulence modeling approach [89] to cost-effectively preserve the unsteadiness of the airwake turbulence. A time-history of the airwake velocities is saved and queried based on the location of the rotorcraft in the CASTLE® flight dynamics software. The saved velocities determine the velocity incident on the rotorcraft aerodynamic model and forces and moments are computed accordingly. Finally, the pilot model attempts to overcome these aerodynamic forces and moments to maintain the desired trajectory. This method presents the same deficiencies as described previously for the one-way coupled uRANS/flight dynamics DI simulation framework, and Polsky et al. acknowledge these as limitations of the approach.

1.3.2 Machine-Learning-Assisted One-Way Coupled Simulations

The explosion in development of Machine Learning (ML) techniques in recent years has provided opportunities in nearly every field of study. ML has recently been investigated in DI calculations by Yu et al. [90]. They performed uRANS simulations of a ship airwake and applied ML to characterize the dynamics of the vortex structures in the flow field. Whether generating training data for the ML technique is less expensive than performing the computations directly has yet to be addressed. This study did not include any analysis of the technique when a rotor wake is present in the solution, so further work is needed to quantify its capabilities in tackling the DI problem directly, especially when desired results begin to deviate from the training data provided.

1.4 Dual-Solver CFD Methods

An approach that reduces the cost of performing uRANS analysis of rotorcraft operations is to employ a dual-solver methodology that optimizes the relative advantages of multiple solvers in a single framework. Dual-solver approaches are common even within pure

Navier-Stokes CFD methods where the computational domain is split into a near-body, which is resolved by conventional uRANS solvers, and an off-body, which is resolved by efficient Cartesian uRANS solvers [91]. This idea has been taken further by resolving the off-body domain with vorticity-based solvers, which can more cost-effectively preserve vorticity-dominated flow fields. There are a plethora of approaches that have been developed, each with their own advantages and disadvantages that will be weighed when considering their application to the DI. The dual-solver approach also alleviates the difficulty in modeling the production of vorticity by solid bodies within vorticity-based solvers [92, 93].

1.4.1 URANS-VTM Methods

The most general way to resolve vorticity-dominated flows is by solving the vorticity transport equations on a computational grid, called Vorticity Transport Methods (VTM). The vorticity transport equations are identical to the incompressible Navier-Stokes equations, but are recast in terms of vorticity instead of velocity. The cost per grid point of VTM is comparable to that of conventional RANS methods, however cost savings arise by alleviating the requirement of RANS methods for highly refined grids to avoid numerical dissipation of vorticity. VTM solvers have been coupled to RANS solvers by the so-called "boundary condition method," where flow variables are passed from one solver to the other through a boundary interface somewhere in the flow volume that separates the two computational domains. The dual-solver code "FUN3D-VorTran-M2", for example, couples the NASA-developed unstructured uRANS solver FUN3D with the VTM solver VorTran-M2 developed by Continuum Dynamics, Inc. (CDI). FUN3D and VorTran-M2 are coupled at a boundary between their respective computational domains, where FUN3D converts its flow variables into the form required by VorTran-M2, and vice-versa (see Figure 1.4). This method has been demonstrated to improve the preservation of vorticity for model problems and isolated rotor problems [94], rotor-fuselage problems [95], and ship airwake problems

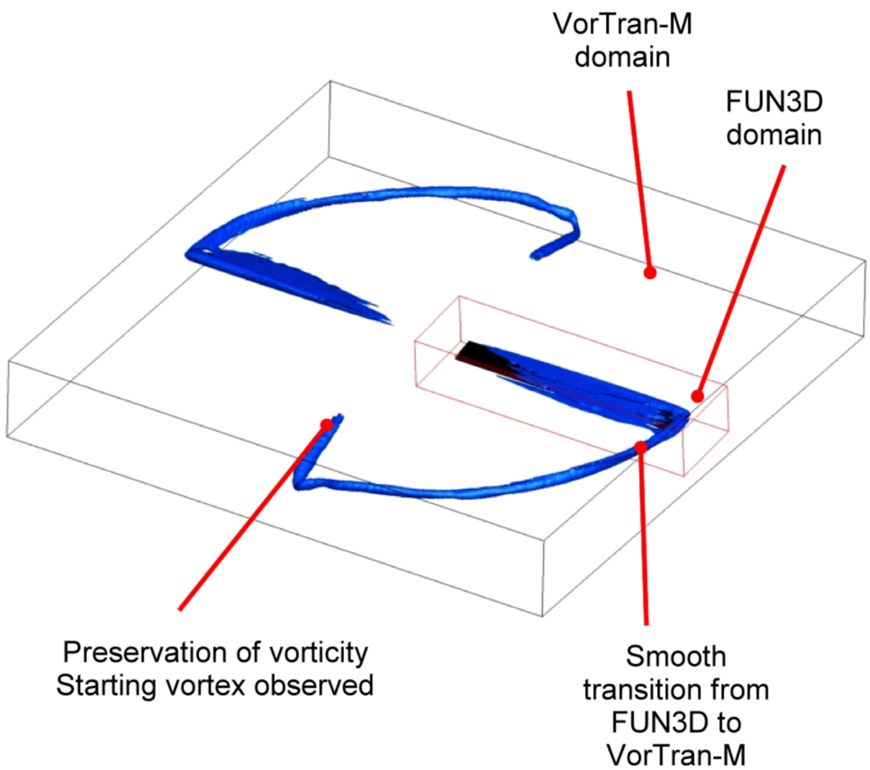

Figure 1.4: Diagram of the uRANS and VTM domains in a FUN3D-VorTran simulation [94].

[96], but is still relatively expensive compared to other dual-solver methods, as it is still solving a form of the Navier-Stokes equations in the VorTran-M domain. uRANS-VTM methods have yet to be applied to the DI problem, and while this method may provide moderate cost savings, specific implementation and parallelization concerns have yet to be fully assessed.

1.4.2 uRANS-VVPM Methods

Viscous Vortex Particle Methods (VVPM) solve the vorticity transport equations by representing the vorticity field as a set of particles with discrete vorticity, location, and distribution function. A detailed discussion of how these particles are used to compute time-accurate flow fields is described by He and Zhao [97]. The production of these particles can be modeled by coupling VVPM to a uRANS solver which resolves solid bodies in the flow field. VVPM are less general than VTM, but can still accurately represent vorticity fields of arbitrary structure. An early implementation of uRANS-VVPM is presented by Anusonti [98]. The boundary condition for the uRANS domain is set to the flow conditions induced by the VVPM solution. The uRANS flow field is converted to vortex particles in the VVPM simulation. The implementation of the boundary condition assumed free-stream density everywhere, which introduced errors near the rotor tip where compressibility effects should not be ignored. The pressure was also purely extrapolated from the uRANS domain, with no direct influence from the VVPM solution.

A more recent implementation of uRANS-VVPM that avoids these nonphysical effects was developed by Advanced Rotorcraft Technology, Inc. and was validated for aeromechanical analysis of the UH-60A rotor [99–101]. Their methodology acknowledges various implementation decisions required for coupling uRANS to VVPM solvers, both in the uRANS-to-VVPM interface and the VVPM-to-uRANS interface. They determine that optimal results are obtained by translating vorticity from the uRANS solution to the VVPM through the "distributed vorticity source method" and employing the "boundary surface method" for communicating VVPM-induced flow conditions into the uRANS solution [100]. There remain some deficiencies in this implementation however, in that oscillations in the VVPM solution at the VVPM update frequency persist at very long wake ages, and no effort is made to smooth the induced boundary condition between VVPM update steps. The communication between the VVPM and uRANS solution is also performed via file I/O, and density and pressure are approximated with isentropic relations, which has been shown to cause errors in dual-solver CFD simulations [102]. Computational cost improvements compared to conventional uRANS methods have yet to be studied in detail.

1.4.3 URANS-PWM Methods

By leveraging some of the expected features of rotor-generated wakes, vorticity-based solvers can be further optimized by representing the vorticity field with structured vorticity elements by making the assumption of potential flow, called Potential Wake Methods (PWM). One example of a PWM is to represent the rotor wake as a lattice of vortex filaments (VL) which are shed from the rotor blades based on their aerodynamics. Coupling a VL solver to a uRANS solver allows these aerodynamics to be predicted from first principles rather than aerodynamic tables or algebraic models. Hybridizations between uRANS and VL solvers have been applied to prediction of rotorcraft aerodynamics in the past, where the uRANS solver is used in a domain very close to the blades to predict blade loads and Blade-Vortex Interactions (BVI). These loads are used to update the bound vorticity in the VL wake model, which can freely deform based on the self-induced velocity of the vortex filaments on themselves. Finally, the wake geometry is used to compute boundary values for the uRANS domain.

GT-Hybrid represents one current implementation of a uRANS-VL method. This solver has been applied to aeroelastic rotors [103], coaxial rotors [104], and tandem rotors [105], but has had difficulty predicting accurate blade pitching moments and structural loads. Additionally, the vortex lattice becomes increasingly chaotic far from the rotor, and its ability to model wake-body interactions has not been assessed in a hybrid solver context, which is important for accurate characterization of the DI. It also employs an inaccurate approach to the boundary condition treatment for hybrid uRANS/free-wake simulations. Free-wake elements within the uRANS domain are not included when computing the induced conditions on the domain boundary in an attempt to prevent double-counting of vorticity predicted by both the uRANS and free-wake solutions. It also employs a characteristic boundary condition based on Riemann invariants to mitigate reflection of outgoing waves. However, these two decisions mean that inflow boundary conditions are not influenced by the rotor wake within the uRANS domain, since the boundary conditions are set to the conditions induced solely by the free-wake solution, which is neglected within the uRANS domain. Outflow boundary conditions do not include the influence of the rotor wake outside the uRANS domain, since the boundary conditions are extrapolated from the interior uRANS solution.

This will result in non-physical or inaccurate conditions at the uRANS domain boundary [106].

The PWM can optionally consist of only a Tip Vortex Filament (TVF), which dominates the dynamics of the wake far from the blades. However, this means that very close to the blade, the effect of the shed vortex sheet is not modeled at all, which is problematic when the uRANS domain is very small. Considering that reducing the size of the uRANS domain is the primary goal of this kind of hybrid method, a potential method which is able to model the vortex sheet is desirable.

OVERTURNS-PWAM is a hybrid uRANS-TVF methodology developed at the University of Maryland which couples the in-house uRANS solver OVERTURNS to the free-vortex wake solver Parallel Wake Analysis Module (PWAM) [107]. The uRANS and free-wake solutions are coupled using a field velocity approach, which superimposes the induced velocities from the free-wake solution onto the entire uRANS domain. This approach can potentially lead to double counting of wake-induced velocities, since both the complete shed vorticity predicted by the uRANS solver and the solitary tip vortex predicted by PWAM influence the velocities in the uRANS domain. It is also much more computationally expensive to compute induced velocities on every point in the flow field, rather than just on the uRANS domain boundary. Thus an improved implementation is necessary for application to the DI problem.

1.5 Thesis Objectives

1.5.1 Shortcomings in Current Approaches for DI Simulation

While full-scale and wind-tunnel testing are viable methods for establishing safe operating limits of ship-helicopter operations, they benefit from supplementation with computational models due primarily to their expense and the competitiveness of wind-tunnel time, respectively. Computational models of the ship-helicopter DI are also required for the development of high-fidelity flight simulators. However, current conventional computational methods which are accurate enough to characterize the DI, such as Navier-Stokes and Lattice-Boltzmann methods, are currently too expensive to be applied to to above problems.

Approaches to computational modeling of the DI can be categorized into unified and one-way coupled DI simulations. In general, unified simulations are hindered by the large range of time and length scales present in the DI flow field when attempting to capture both the ship and helicopter aerodynamics simultaneously. Attempts to simplify the aerodynamic models in a unified simulation will be hindered by the difficulty of characterizing the ship aerodynamics with a mid-fidelity model.

Established methods for one-way coupled simulations of the DI are limited to direct input of the ship airwake into flight simulators, resulting in poor capture of the nonlinear aerodynamic effects which occur as the helicopter approaches the shipboard. While cost-effective, there is a need to improve on this method so that flight simulator training for shipboard-landing is more valuable to new pilots. Additionally, those same nonlinear aerodynamics will define the operating limits of ship-helicopter combinations, and thus must be at least partially accounted for in the modeling technique.

Dual-solver CFD methods present an opportunity to address the exorbitant computational cost of unified DI simulations while improving on the accuracy of one-way coupled DI simulations. However, first-generation dual-solver CFD methods have made implementation decisions that make them inaccurate or inflexible in analysis of complex aircraft configurations and are therefore not suitable to application in a DI analysis context.

1.5.2 Thesis Objectives

This thesis sets out to develop and validate of a hybrid uRANS/free-vortex wake solver to enable its application to the DI. This method will be assessed for its ability to accurately model the complex aerodynamic interactions present in the DI while leveraging the various advantages of its component solvers. In comparison with uRANS methods, this dual-solver methodology seeks to significantly reduce the cost of simulation the full range of DI conditions for a given ship/helicopter pair. To accomplish this, the following objectives will be met:

1. Extend a baseline hybrid uRANS/free-wake solver, OVERFLOW-CHARM, to efficiently predict rotor and fuselage loads and aerodynamic interactions between the rotor, fuselage, and ship superstructure with the necessary accuracy to characterize the DI.
2. Improve the implementation of the free-wake boundary condition on the uRANS domain to maximize the accurate capture of unsteady aerodynamics by OVERFLOW-CHARM.
3. Validate the efficacy of improvements to OVERFLOW-CHARM using representative Advanced Air Mobility (AAM) problems that contain important features of the DI: an integrated propulsion system and a rotor in hover in ground effect
4. Demonstrate the capability of the improved OVERFLOW-CHARM code to be applied to calculations of the DI by simulating a UH-60L operating near an on-land analog of an LPD-17 hangar face, validating with flight test data of the same configuration.

CHAPTER 2

COMPUTATIONAL TOOLS

This research involves the development and extension of a hybrid unsteady Reynolds-Averaged Navier-Stokes (uRANS)/free-vortex wake methodology which couples together two existing aerodynamic solvers. This chapter will describe the governing equations of these component solvers, their native capabilities, and their use in this work. Finally, the capabilities of the hybrid solver prior to this research will be described to contextualize the work required to apply it to the Dynamic Interface (DI) problem. A discussion of Kestrel, the third-party uRANS tool that was utilized to produce airwake data for DI simulations, is also provided.

2.1 Navier-Stokes Solver

2.1.1 Governing Equations

Solutions to the uRANS equations resolve the fundamental physics which govern fluid motion with modeling of turbulent effects. As such, they are able to provide accurate, detailed flow fields in the near-wake region close to rotor blades. This set of equations can be solved numerically on engineering-scale computational grids. The governing equations are as follows:

Conservation of mass for a continuous medium can be expressed in tensor notation as:

$$\frac{\partial \rho}{\partial t} + \frac{\partial}{\partial x_j}\left(\rho u_j\right) = 0, \tag{2.1}$$

conservation of momentum in the i^{th} direction can be written:

$$\frac{\partial \rho u_i}{\partial t} + \frac{\partial}{\partial x_j}\left(\rho u_i u_j + p\delta_{ij} - \tau_{ij}\right) = B_i, \tag{2.2}$$

and conservation of energy is:

$$\frac{\partial \rho e_0}{\partial t} + \frac{\partial}{\partial x_j}\left(\rho h u_j + p u_j - \kappa \frac{\partial \Theta}{\partial x_j} - \tau_{ij} u_i\right) = 0, \tag{2.3}$$

where the viscous stress tensor τ_{ij} can be expanded to:

$$\tau_{ij} = -p\delta_{ij} + 2\mu S_{ij} + \delta_{ij}\lambda_b \frac{\partial u_k}{\partial x_k}\delta_{ij}. \tag{2.4}$$

The Stokes hypothesis is commonly invoked to simplify this expression by enforcing equality between the mechanical and thermodynamic pressure.

$$\lambda_b = -\frac{2}{3}\mu. \tag{2.5}$$

The viscous stress tensor can then be simplified to:

$$\tau_{ij} = 2\mu\left(S_{ij} - \frac{1}{3}\frac{\partial u_k}{\partial x_k}\delta_{ij}\right). \tag{2.6}$$

The strain rate tensor S_{ij} can be written in terms of the fluid velocity components as:

$$S_{ij} = \frac{1}{2}\left(\frac{\partial u_i}{\partial x_j} + \frac{\partial u_j}{\partial x_i}\right). \tag{2.7}$$

To determine the molecular viscosity and thermal conductivity as a function of the fluid temperature, it is standard practice to invoke Sutherland's kinetic theory, which states that:

$$\mu = C_1 \frac{\Theta^{\frac{3}{2}}}{\Theta + C_2} \tag{2.8}$$

and that:

$$\kappa = C_3 \frac{\Theta^{\frac{3}{2}}}{\Theta + C_4}, \tag{2.9}$$

where C_1, C_2, C_3, and C_4 are Sutherland's constants. Using the definitions of total energy

$e_0 = \frac{p}{\rho(\gamma_p - 1)} + \frac{1}{2} u_k u_k$ and total enthalpy $h_0 = e_0 + \frac{p}{\rho}$, the equations can be closed using an equation of state for the fluid, usually the ideal gas law for subsonic Mach regimes:

$$p = \rho R_g \Theta. \tag{2.10}$$

Numerical solutions to the Navier-Stokes equations for many real flows involve very small-scale flow structures whose influence on the large-scale flow is non-negligible. As such, very fine computational grids are required to adequately resolve these structures. Simulations like this, called “Direct Numerical Simulations” (DNS), are extremely expensive and are not practical for engineering applications, especially at the high Reynolds numbers present in shipboard landing applications.

Below a certain size, the small flow structures, called “turbulent eddies” or simply “turbulence”, can be modeled as small deviations from a statistical mean value of the flow at a given location. The Navier-Stokes equations can be written in terms of these mean flow variables as follows:

$$\frac{\partial \overline{\rho}}{\partial t} + \frac{\partial}{\partial x_j} \left(\overline{\rho u_j} \right) = 0, \tag{2.11}$$

$$\frac{\partial \overline{\rho u_i}}{\partial t} + \frac{\partial}{\partial x_j} \left(\frac{\overline{\rho u_i}\, \overline{\rho u_j}}{\overline{\rho}} + \overline{p} \delta_{ij} + \overline{\rho u_i' u_j'} - \overline{\tau_{ij}} \right) = 0, \tag{2.12}$$

$$\frac{\partial \overline{\rho e_0}}{\partial t} + \frac{\partial}{\partial x_j} \left(\frac{\overline{\rho h_0}\, \overline{\rho u_j}}{\overline{\rho}} + \overline{p u_j'} + \overline{\rho e_0' u_j'} + \kappa \frac{\partial \overline{\Theta}}{\partial x_j} - \overline{u_i \tau_{ij}} \right) = 0, \tag{2.13}$$

where $[]' = [] - \frac{\overline{\rho []}}{\overline{\rho}}$, and $\overline{[]}$ is an ensemble (“Reynolds”) average of quantity $[]$. This results in unclosed terms that describe the effect of turbulence on the mean flow. In engineering-scale applications, these terms can be modeled with various formulations, called “turbulence models” or “turbulence closures”, which provide varying levels of fidelity and computational cost and each have their own advantages and disadvantages. With the closure of the Reynolds Stress term, the resulting system is known as the “uRANS equations”.

Instead of ensemble averaging, the flow field turbulence can be filtered into grid-scale and Sub-Grid-Scale (SGS) turbulence. The resulting system of equations looks the same, but instead of solving for Reynolds-averaged quantities, these equations resolve large-scale eddies and model SGS eddies, hence they are called "Large Eddy Simulations (LES)". LES models have stricter grid resolution requirements to obtain accurate results in the boundary layer where turbulence scales of interest are very small. They are, however, more adept at capturing the unsteady nature of the resolved flow field, especially in regions of separated flow when compared to Reynolds-Averaged Navier-Stokes (RANS)-based turbulence models.

2.1.2 Solver Formulation: OVERFLOW

OVERFLOW is developed and supported by the National Aeronautics and Space Administration (NASA) and solves the uRANS equations on a given computational domain. The computational domain can be divided into subset grids that have points ordered in three-dimensional lists (J,K,L), known as "structured" grids. Where the grids overlap, the flow solution is communicated between them via high-order interpolation methods. This formulation is called a structured overset (chimera) solver. Oversetting allows fluid domains with complex geometries to be resolved with surface-conforming structured grids and fast, high-order spatial differencing algorithms. OVERFLOW provides a wide array of solution techniques that can be specified by the user depending on the desired application. For inviscid flux algorithms, OVERFLOW includes second-, fourth-, and sixth-order central differencing with smoothing, Yee symmetric Total Variation Diminishing (TVD), Advection Upstream Splitting Method (AUSM)+ upwind, third-order Roe upwind, third-order Harten-Lax-van Leer-Contact (HLLC) upwind, and fifth-order Weighted Essentially Non-Oscillatory (WENO) and Weighted Essentially Non-Oscillatory Mapped (WENOM) upwind with Koren, Minmod, or van Albada flux limiters. The implicit solvers for left-hand side terms are Beam-Warming block tridiagonal solver with either central difference or upwind Steger-Warming flux Jacobians, Steger-Warming two-factor scheme, Alternating Direction Implicit (ADI) Pulliam-Chaussee scalar pentadiagonal solver, Lower Upper-Symmetric Gauss Seidel (LU-SGS) solver, Diagonalized Diagonal Dominant Alternating Direction Implicit (D3ADI) diagonalized solver, and Symmetric Successive Over-Relaxation (SSOR) solver. Turbulence can be modeled using Baldwin-Lomax algebraic model with wake model, Baldwin-Barth one-equation transport model, Spalart-Allmaras one-equation transport model, Spalart-Allmaras Detached Eddy Simulation (DES) and Delayed Detached Eddy Simulation (DDES) hybrid RANS/LES models, k-ω two-equation transport model, Shear-Stress Transport (SST) two-equation transport model, SST DES and SST DDES two-equation transport hybrid RANS/LES models, and SST Multi-Scale (MS) two-equation transport hybrid RANS/LES model with wall functions, rotation and curvature corrections, and temperature corrections for the appropriate models [108].

2.1.3 Current Usage

In this research, the strengths of OVERFLOW will be leveraged by using it to compute the flow physics very near the rotor blades so that accurate interactional aerodynamics and integrated loads can be computed. While OVERFLOW, like all body-fitted uRANS solvers, requires a highly refined computational grid in order to accurately capture the flow physics, this approach mitigates this cost through a dual-solver coupling methodology described in section 2.3. Numerical schemes and turbulence models are chosen on an application-to-application basis, based on parametric studies and existing literature to provide the optimal compromise between computational cost and fidelity. It is also used to establish a baseline reference for computational cost and fidelity of conventional uRANS methods applied to the configurations of interest, as in Figure 2.1.

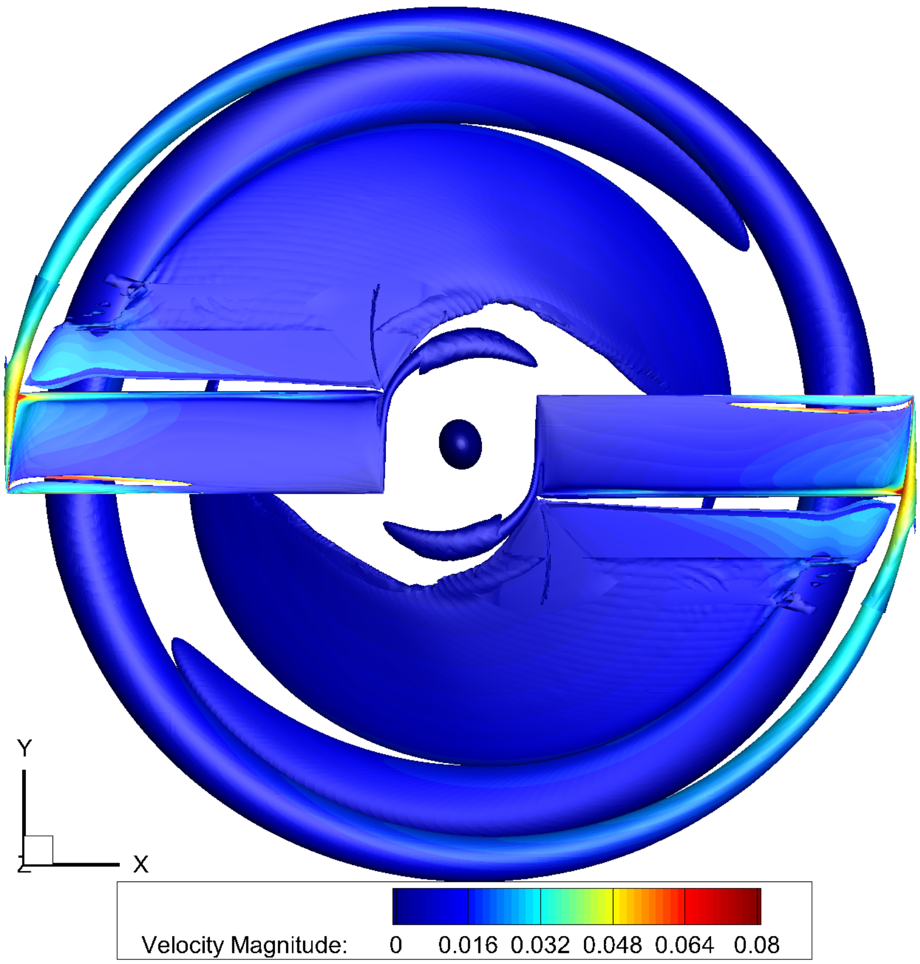

Figure 2.1: OVERFLOW prediction of the wake geometry of an isolated, two-bladed rotor in hover, visualized with an isosurface of nondimensional Q-criterion = 0.0001.

2.2 Potential Flow Solver

2.2.1 Governing Equations

Lagrangian free-vortex wake algorithms offer a low-cost mid-fidelity method for performing rotorcraft aerodynamic analysis. They are based on the representation of the aerodynamic field as vortex elements whose behavior is governed by the potential flow equations, specifically as extensions of Prandtl's lifting line method. The potential flow equations are the inviscid, irrotational form of the Navier-Stokes equations, and can be written in unsteady compressible form as:

$$-\frac{1}{a^2}\left(\frac{\partial}{\partial t}\left(\nabla\phi \bullet \nabla\phi\right)+\frac{\partial^2\phi}{\partial t^2}\right)+\left(1-M_x^2\right)\frac{\partial^2\phi}{\partial x^2}+\left(1-M_y^2\right)\frac{\partial^2\phi}{\partial y^2}+\left(1-M_z^2\right)\frac{\partial^2\phi}{\partial z^2}$$
$$-2M_xM_y\frac{\partial^2\phi}{\partial x\partial y}-2M_yM_z\frac{\partial^2\phi}{\partial y\partial z}-2M_zM_x\frac{\partial^2\phi}{\partial z\partial x}=0, \quad (2.14)$$

where Φ is the velocity potential function, a is the local speed of sound, and

$$M_x=\frac{1}{a}\frac{\partial\phi}{\partial x}, M_y=\frac{1}{a}\frac{\partial\phi}{\partial y}, M_z=\frac{1}{a}\frac{\partial\phi}{\partial z}. \quad (2.15)$$

2.2.2 Solver Formulation: CHARM

The CHARM Wake-Panel Module is the aerodynamic component of the CHARM rotorcraft analysis tool developed and supported by Continuum Dynamics, Inc. (CDI). For brevity, the CHARM Wake-Panel Module will henceforth be referred to as "CHARM". CHARM is a full-span free-vortex Constant Vorticity Contour (CVC) wake method, and the aerodynamic principles the method is based on will be briefly described. In Prandtl lifting line theory, the lift along the span of a wing or, more pertinently, a rotor blade is represented by a circulation distribution $\Gamma(r,t)$ with r along the span as shown in Figure 2.2a.

The wake of the blade is composed of a continuous sheet of shed vorticity:

$$\vec{\gamma} = \frac{\partial \Gamma}{\partial r}\hat{r} + \frac{\partial \Gamma}{\partial t}\hat{\psi}. \tag{2.16}$$

As the blade rotates and the circulation distribution changes, the shed vortex evolves into a sheet with continuous variation of the shed vorticity vector. Assuming this sheet remains planar, it can be visualized with contour lines of constant vorticity, as in Figure 2.2b. These lines are "released" from the blade so that the circulation between successive lines is constant, or:

$$\frac{\partial \Gamma}{\partial r} \simeq \frac{\Delta \Gamma}{\Delta r}. \tag{2.17}$$

This means that constant vorticity contour lines are concentrated near high gradients in the circulation distribution. A full-span CVC free-vortex wake method represents the rotor wake as vortex filaments which approximate these contours of constant vorticity. First, the wake is initialized with a prescribed geometry, and the lines of constant vorticity are computed based on the blade circulation variation with span and azimuth angle. They are then converted into vortex filaments and allowed to deform freely according to the freestream velocity and the Biot-Savart induced velocity integrated over all vortex elements in the domain. The Biot-Savart law states that the velocity $d\vec{u}_i$ induced by an infinitesimal vortex filament $\vec{dl}$ with strength γ at a distance $\vec{r}$ is:

$$d\vec{u}_i = \frac{\gamma}{4\pi}\frac{\vec{dl} \times \vec{r}}{|\vec{r}^3|} \tag{2.18}$$

CHARM is able to perform the Biot-Savart integration efficiently by using Basic Curved Vortex Elements (BCVE). BCVEs have a parabolic shape as opposed to the conventional linear elements used in many other free-wake solvers. As such, the rotor wake can be represented accurately with fewer vortex elements, which has a positive impact on the computational efficiency of CHARM. Detailed discussions of the merits and implementation of this method can be found in Bliss et al. [76] and Quackenbush et al. [109].

CHARM has been successfully applied to problems related to rotor aeroelasticity [110, 111], DI [112–114], fixed-wing flight simulation [115], Unmanned Aircraft Systems (UAS) aeroacoustics [116–118], integrated propulsion systems [119], main/tail rotor interactions [120], rotor fuselage interactions [121], and rotor hover performance [122–124].

2.2.3 Current Usage

In this research, CHARM is used to compute far-wake aerodynamics, including wake-body interactions, of rotors, rotorcraft, and rotating systems in the hybrid uRANS/free-wake framework discussed in section 2.3. Interactions with ground planes are modeled using an image plane method, and more complex geometries are represented with doublet panels. Lifting bodies shed Morino [125] wake panels into the flow field, which interact with the free-vortex wake. Ship airwake coupling is supported through a variety of methods, of which the primary method is through a database. The number of vortex elements and update frequency in the CHARM rotor wake model are chosen based on the application so that the relevant aerodynamics are sufficiently resolved. The CHARM component of a simulation of a wing-integrated propeller configuration is shown in Figure 2.3.

2.3 Hybrid CFD Methodology

2.3.1 Motivation

OVERFLOW and CHARM represent the state of the art in uRANS and free-wake analysis. However, these solvers have downsides inherent to their basic formulation. OVERFLOW, as with all uRANS methods, has a high computational cost per point and is dissipative when high-gradient regions are not well resolved. CHARM, as with all free-wake methods, is not able to capture complex viscous phenomena, e.g. separation, and must model blade loads using blade-element momentum theory instead of from first principles. For rotorcraft flows, there are well-defined regions where each of the solvers are expected to perform

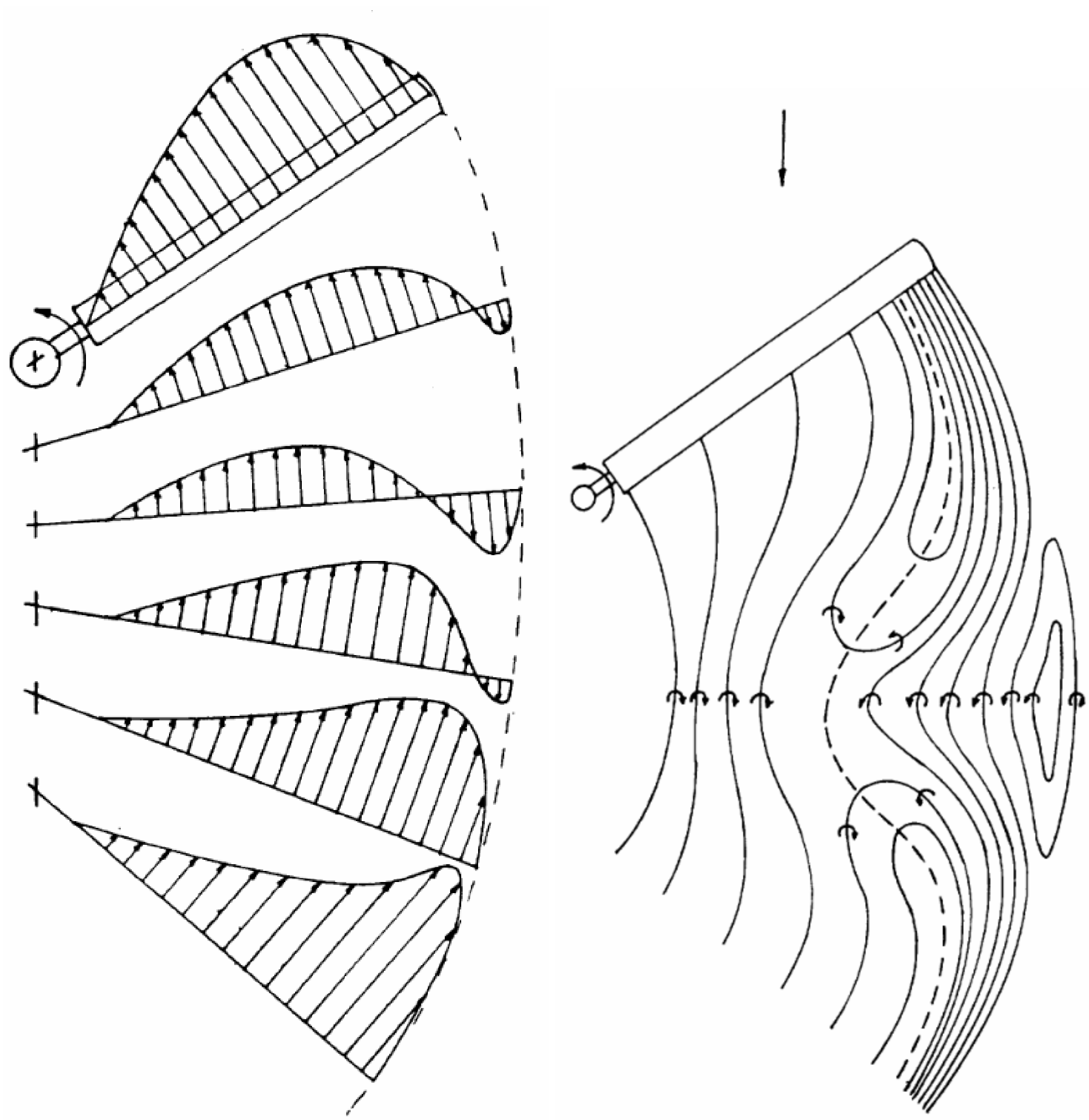

(a) **Typical Blade Circulation Distribution** (b) **Resulting Constant Vorticity Contours**

Figure 2.2: How variation of blade circulation distribution impacts contours of constant vorticity in the shed vorticity sheet, from Quackenbush et al. [109].

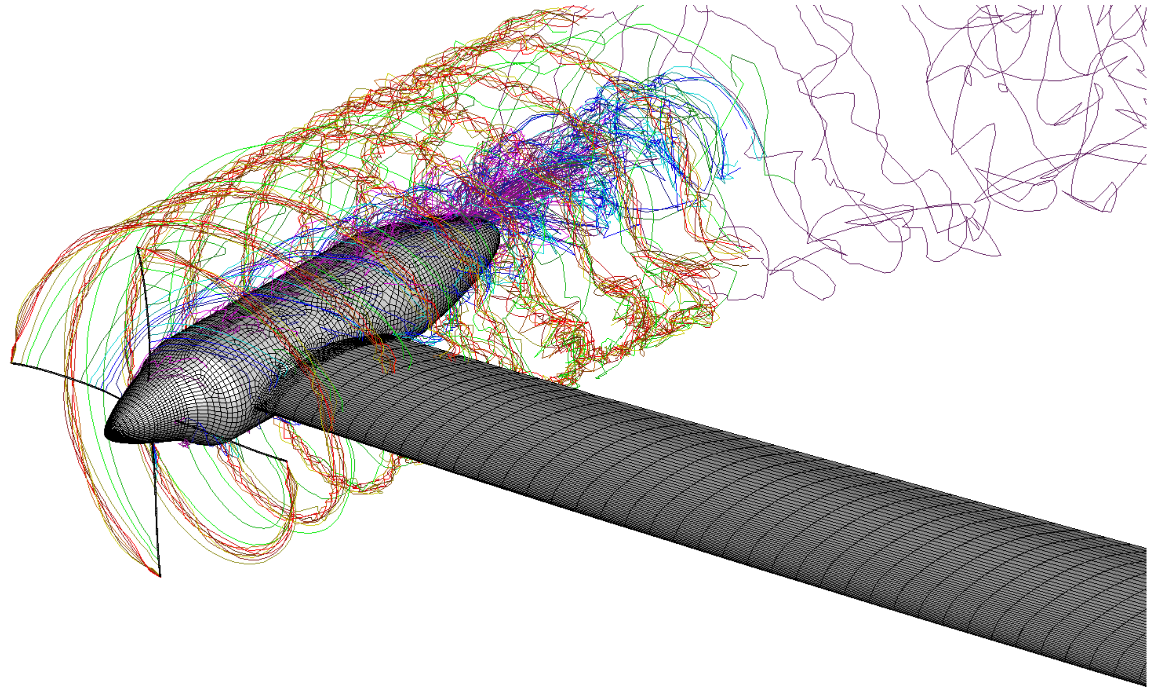

Figure 2.3: CHARM prediction of the wake geometry of a wing-integrated propeller system, visualized with vortex elements colored by release location.

well and other regions where their downsides are expected to manifest. A methodology which allows the two solvers to compute in parallel to capture the rotor aerodynamics can efficiently allocate computational resources to the solver which is best suited to the flow conditions in each region.

2.3.2 Solver Formulation: OVERFLOW-CHARM

OVERFLOW-CHARM is a dual-solver Computational Fluid Dynamics (CFD) framework which couples OVERFLOW to CHARM. OVERFLOW acts in a near-wake region where blade loads can be accurately computed, and these loads are used to set the bound vorticity distribution on the blades in the rotor model within CHARM. CHARM then sheds CVC BCVEs from the full span of the blade based on the local bound vorticity, and these filaments are convected by the freestream and an integration of the Biot-Savart induced velocities due to the other filaments in the wake model. The resulting wake model is used to compute fluid properties on the boundary of the OVERFLOW domain. The implementation

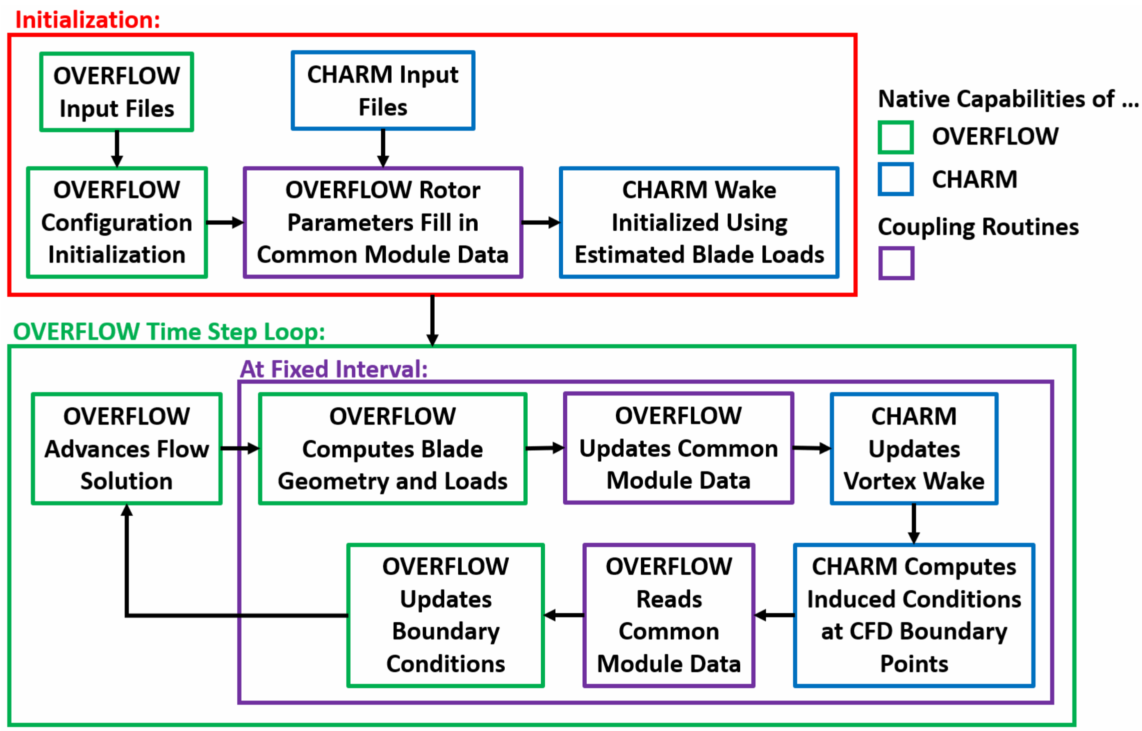

Figure 2.4: Diagram detailing the OVERFLOW-CHARM coupling process.

of this process is detailed visually in Figure 2.4.

2.3.3 Current Usage

OVERFLOW-CHARM is applied in theis research to compute detailed rotorcraft aeromechanics at significantly reduced computational cost when compared to a conventional uRANS simulation. This is achieved by reducing the uRANS domain to a region very close to the blades. The uRANS domain reduction can be tailored to provide the most favorable trade-off between cost and fidelity, depending on the simulation configuration. Elements of the configuration which are not modeled by the uRANS are included in the CHARM aerodynamic model, including wings, fuselages, ground planes, shipboards, and ship airwakes.

2.3.4 Capabilities Prior to this Research

The basic formulation of OVERFLOW-CHARM was developed prior to this effort, though it was relatively limited in terms of its capabilities and flexibility. There was also room for additional improvement in the accuracy of the boundary condition that serves as the interface between the two solvers, particularly for unsteady aerodynamic effects. Despite these limitations, it was validated for basic rotor aerodynamic and aeroelastic analysis. It was employed to predict the effect of tip geometry variation on hover performance of the 7A rotor where it was able to predict figure of merit curves on par with conventional CFD methods with up to 94% reduced computational cost [126, 127]. It was also applied in an investigation of the aeroelastic loads of the UH-60a rotor in forward flight and was found to predict aerodynamic and structural loads within 4% of conventional CFD/Computational Structural Dynamics (CSD) methods at up to 70% reduced computational cost [128, 129]. While these studies validated the efficacy of the general approach of OVERFLOW-CHARM, multiple improvements were necessary to apply OVERFLOW-CHARM to the DI problem.

2.4 Airwake Simulation

2.4.1 Motivation

To best demonstrate the one-way coupled nature of the ship airwake and rotorcraft simulations in this approach, which is the primary contributor to its cost-effectiveness, airwake simulations are performed with an entirely different solver. Ideally, this solver should be well-validated in ship airwake computations and be integrated to academic, government, and industry workflows. It should be able to resolve highly unsteady detached flows and output airwake data with computationally efficient techniques.

2.4.2 Solver Formulation: HPCMP CREATE™™-AV Kestrel

The solver chosen to produce the ship airwake is Kestrel [130–132], a framework of CFD tools that already has seen use in DI applications [38]. It has been extensively improved and validated for the types of flows present in the DI [133, 134] and has been adopted for academic [135], government [134], and industry applications [136]. Kestrel itself is primarily an architecture to enhance CFD job setup and execution and serves as an interface between various component tools, many of which are interchangeable based on the user's needs.

2.4.3 Current Usage

In this research, only the job setup user interface, job execution utility, uRANS solver, and co-visualization output components of Kestrel were utilized. The CFD solver chosen was the default near-body unstructured solver Kestrel Computational Fluid Dynamics (KCFD). KCFD solves the uRANS equations as described in subsection 2.1.1, but uses an unstructured finite volume formulation. The unstructured format of the computational grid limits spatial accuracy to second order, but simplifies grid generation permitting automated techniques to be integrated into the workflow. For output of the airwake database, a co-visualization manager was utilized to interpolate flow conditions onto a user-specified Cartesian grid during the simulation. This database was supplied as an input to the OVERFLOW-CHARM solver which "flies" the helicopter within the influence of the airwake.

CHAPTER 3

EXTENSIONS AND IMPROVEMENTS TO A HYBRID CFD FRAMEWORK

3.1 Motivation for Extensions

Chapter 1 discussed some of the limitations of current hybrid Computational Fluid Dynamics (CFD) methodologies, while Chapter 2 described the implementation of OVERFLOW-CHARM prior to this work. Many of the drawbacks discussed in Chapter 1 were present in the implementation of OVERFLOW-CHARM prior to thie effort, and one of the goals of this research is to extend and improve OVERFLOW-CHARM so that it is accurate and flexible enough to be applied to the complex configurations required for Dynamic Interface (DI) investigations.

3.2 Capability Extensions

3.2.1 Advanced Rotor Configurations and Carefree Blade Deformation

The OVERFLOW-CHARM framework was originally unable to model more than one rotor or arbitrary rotor-hub positions relative to the inertial frame. With the push toward advanced future vertical lift designs, it is important for a DI analysis tool to resolve complex rotor-rotor and rotor-fuselage configurations. Both OVERFLOW and CHARM have native capability for modeling multiple rotors. OVERFLOW includes the number of rotors as a user input, as well as each rotor's reference conditions, number of blades, and unsteady Reynolds-Averaged Navier-Stokes (uRANS) grids associated with each blade. The blade geometry is derived from the surface grid topology, and blade deformations are driven either by coupling to a structural solver or with prescribed blade motion. CHARM requires all rotor and blade properties as inputs. The coupling routines between OVERFLOW and CHARM were refactored so that all the required information was passed from

OVERFLOW to CHARM, regardless of the complexity of the configuration.

The original OVERFLOW-CHARM framework required a blade deformation file, even when modeling rigid blades. This also limited coupling of OVERFLOW-CHARM to particular structural solvers that perform CFD-Computational Structural Dynamics (CSD) coupling through file I/O. To address this, the OVERFLOW-CHARM coupling routines were refactored to be agnostic to CFD-CSD coupling information and to compute blade geometry directly from the deformed uRANS grid. In particular, the reference frames of each rotor and its component blades are now derived from the user inputs and automatically convert blade quarter chord computed in the inertial reference from to the blade quarter chord in the CHARM blade reference frame with the following procedure:

for $ir = 1 : n\_rotors$ **do**

  for $ib = 1 : n\_blades(ir)$ **do**

    $[T](ir, ib) \leftarrow get\_blade\_transformation\_from\_inputs(psi)$

    $xqc \leftarrow compute\_quarter\_chord()$

    $xqc\_charm(ir, ib) \leftarrow transform\_quarter\_chord(xqc, [T](ir, ib))$

  end for

end for

This removes the requirement of a null blade motion file when rigid motion is desired. It also permits CFD-CSD coupling between OVERFLOW-CHARM and RCAS via the High-Performance Computing Modernization Program (HPCMP) Computational Research and Engineering Acquisition Tools and Environments (CREATE™)-Air Vehicles (AV) Helios framework, which deforms the uRANS grid through the Melodi mesh manager [137] rather than through a blade motion file.

3.2.2 Optimization of Simulation Initialization

Before the OVERFLOW-CHARM simulation begins, the CHARM free-vortex wake solution is initialized. An initial guess for the rotor sectional loads as a function of azimuth angle is supplied to initialize the CHARM wake. Revolutions of free-wake analysis are required to remove initial transients in the CHARM solution that can adversely influence the beginning of OVERFLOW-CHARM coupling.

Figure 3.2 gives a comparison of the original initialization procedure with the new optimized routine. As the induced velocity computation is the most expensive routine in the OVERFLOW-CHARM coupling, induced velocities are now only computed during initialization when they are required for boundary value interpolation (discussed later). uRANS grid motion is computed during this procedure so that the induced velocities can be applied immediately to boundary value interpolation. The optimized initialization procedure can be summarized as:

$boundary\_points \leftarrow get\_boundary\_points\_from\_grid()$

for $i\_rev = 1 : n\_init\_revs$ **do**

  for $i\_psi = 1 : n\_psi$ **do**

    $psi \leftarrow i\_psi/n\_psi * 360$

    for $ir = 1 : n\_rotor$ **do**

      for $ib = 1 : n\_blades(ir)$ **do**

        $lift(ir, ib) \leftarrow get\_lift\_from\_input\_file(psi)$

      end for

    end for

    $wake \leftarrow update\_charm\_wake(lift)$

    if $interpolation = true$ & $i\_rev = n\_init\_revs$ **then**

      $boundary\_pts \leftarrow rotate\_boundary\_pts(psi)$

      $boundary\_vels \leftarrow get\_boundary\_vels(wake, boundary\_pts)$

    end if

  end for

end for

These improvements allow multiple revolutions of CHARM-wake initialization to be performed at minimal computational expense, further improving the quality of the initialized CHARM solution.

uRANS analysis of low-advance-ratio rotorcraft cases is often plagued by strong initial transients that take a very long time to leave the flow domain, sometimes persisting for dozens of simulated revolutions. This problem can be effectively mitigated by providing an accurate initial guess of the uRANS flow field; however, this is not trivial for conventional uRANS methods and can still incur a significant computational cost penalty. Persisting initial transients are also observed in low-advance-ratio OVERFLOW-CHARM simulations, but, with recent developments to the coupling interface, there is now a cost effective method for initializing the flow field. After the CHARM vortex wake solution is initialized, velocities induced by the CHARM wake can be computed at every point in the uRANS flow field. Because the uRANS domain is already optimally decomposed at this stage and each processor owns the full CHARM solution, the cost required to do so is minimal and well worth the benefits to convergence. The uRANS flow field at the *beginning* of an OVERFLOW-CHARM simulation of an S76 rotor in hover is displayed in Figure 3.1, where such a highly-developed wake would have previously taken multiple revolutions of fully-coupled simulation to generate.

3.2.3 Single Gridded Blade (SGB) Simulation

Originally, OVERFLOW-CHARM required all blades to be resolved with uRANS grids. In flight conditions where rapid convergence to periodicity is expected, it may be desirable to resolve only a single blade with a uRANS grid. This capability was added to OVERFLOW-CHARM so that the loads and deformations of ungridded blades are duplicated from those computed on a single gridded blade based on assumed periodicity of the solution. CHARM still predicts the wake from the true number of blades in this scenario so that correct blade-wake interactions are predicted. In axisymmetric cases, the blade loads and properties of all blades can be set equal to those computed on the resolved blades. This procedure may

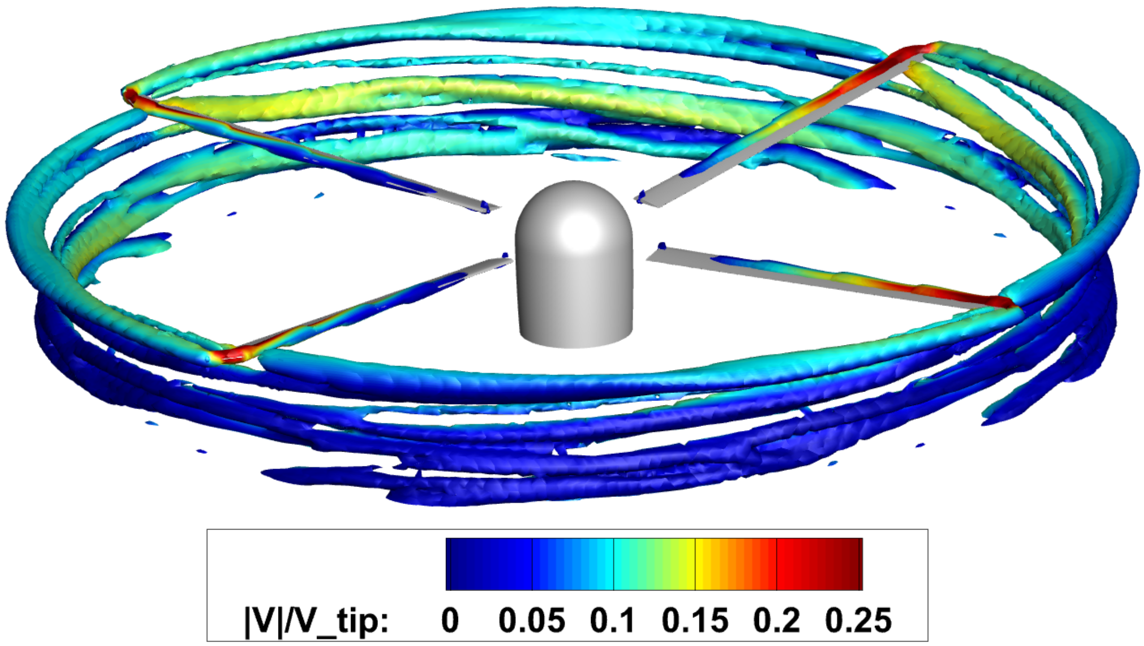

Figure 3.1: uRANS flow solution of an S76 rotor in hover initialized using CHARM.

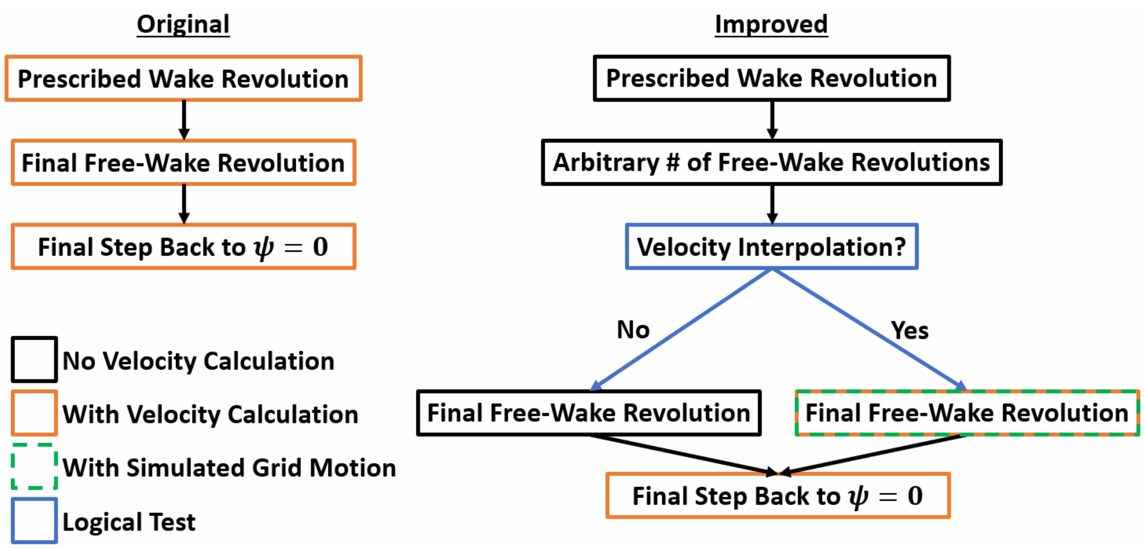

Figure 3.2: Flow charts comparing the original CHARM wake initialization procedure to the current routine.

be written as

$lift(1, psi) = compute\_lift\_from\_overflow()$

for $ib = 1 : n\_blades$ **do**

  if $Axisymmetric = true$ **then**

    $lift(ib, psi) = lift(1, psi)$

  else

    $lift(ib, psi) = lift(1, psi - 360/n\_blades * (ib - 1))$

  end if

end for

This approach reduces the size of the uRANS grid by a factor of the number of rotor blades, and thus significantly reduces the computational cost of the simulation. Because blade loads and geometries at each azimuth station in the CHARM simulation are updated only once every revolution instead of once every blade passage, the convergence rate of the OVERFLOW-CHARM solution may be somewhat slower, though this is offset by the reduction in the number of blade mesh points. Additionally, the convergence rate is not affected in axisymmetric cases, making single-blade simulations very cost-effective for hover, climb, and descent analysis of isolated rotors. In Figure 3.3, this conclusion is demonstrated for a two-bladed rotor in hover, where the thrust convergence behavior is not negatively impacted by the Single-Gridded-Blade (SGB) methodology and computational cost is reduced by approximately a factor of two compared to a fully gridded rotor.

3.2.4 Ship Airwake Coupling

The CHARM module allows the influence of aerodynamics external to the simulation to be modeled in a variety of ways. The most general of these is through a call to a custom subroutine that can modify the velocities at the CHARM wake control points. The modeling fidelity of this subroutine is unbounded, but the simplest implementation is to query a database for velocities and add them to the existing velocities of the CHARM control

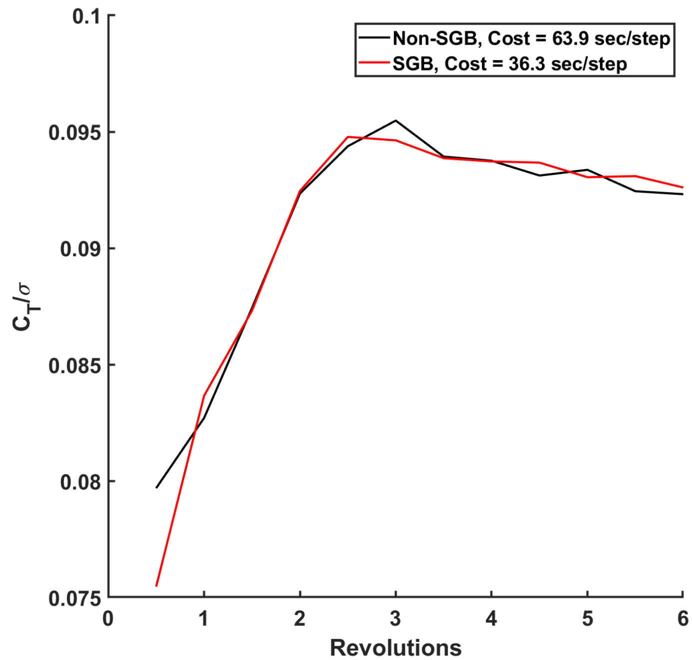

Figure 3.3: Thrust convergence behavior of a standard OVERFLOW-CHARM simulation compared with a single-gridded blade simulation for hover analysis of a two-bladed rotor.

points. This represents a linear superposition of the external aerodynamics with the aerodynamics predicted by OVERFLOW-CHARM. More sophisticated ship airwake modeling is available in CHARM, however, this implementation is deemed sufficient for the analysis in this research.

Ship airwake coupling is performed by first simulating the ship airwake without the rotor model present. This permits large time steps to be applied, and the database only has to be generated once for a given Wind-Over-Deck (WOD) condition, making this approach highly cost-effective. A uniform Cartesian sample of the airwake is taken in the spatial and temporal range of aircraft operation and saved for use by OVERFLOW-CHARM. During the OVERFLOW-CHARM simulation when the CHARM wake is updated, CHARM calls the custom ship airwake coupling routine, which loops over the CHARM wake control points and uRANS boundary points, interpolates the velocities from the ship airwake database onto the point, and adds the resulting velocity to the existing velocity at the point.

As long as the ship airwake database is stored on a uniformly spaced Cartesian grid, the cell that the CHARM point lies within can be calculated directly, such that the cost of the coupling only scales with the number of points in the CHARM simulation, and the airwake database can be arbitrarily large (within memory constraints) without impacting the speed of the algorithm. The database indices that the CHARM point (x,y,z) lies within are

$$i_0 = floor\left(\frac{(i_{max}-1)(x-x_{min})}{x_{max}-x_{min}}\right), \qquad i_1 = i_0 + 1, \tag{3.1}$$

$$j_0 = floor\left(\frac{(j_{max}-1)(y-y_{min})}{y_{max}-y_{min}}\right), \qquad j_1 = j_0 + 1, \tag{3.2}$$

$$k_0 = floor\left(\frac{(k_{max}-1)(z-z_{min})}{z_{max}-z_{min}}\right), \qquad k_1 = k_0 + 1, \tag{3.3}$$

Trilinear interpolation from these points onto the CHARM point is calculated as

$$\vec{u}_{new} = \vec{u}_{old} + \vec{c_0}\,(1-z_d) + \vec{c_1} z_d \tag{3.4}$$

where

$$\vec{c_0} = \vec{c_{00}}\,(1-y_d) + \vec{c_{10}} y_d, \qquad \vec{c_1} = \vec{c_{01}}\,(1-y_d) + \vec{c_{11}} y_d \tag{3.5}$$

$$\vec{c_{00}} = \vec{u}_{ship}\,(i_0, j_0, k_0)\,(1-x_d) + \vec{u}_{ship}\,(i_1, j_0, k_0)\,x_d \tag{3.6}$$

$$\vec{c_{01}} = \vec{u}_{ship}\,(i_0, j_0, k_1)\,(1-x_d) + \vec{u}_{ship}\,(i_1, j_0, k_1)\,x_d \tag{3.7}$$

$$\vec{c_{10}} = \vec{u}_{ship}\,(i_0, j_1, k_0)\,(1-x_d) + \vec{u}_{ship}\,(i_1, j_1, k_0)\,x_d \tag{3.8}$$

$$\vec{c_{11}} = \vec{u}_{ship}\left(i_0, j_1, k_1\right)\left(1 - x_d\right) + \vec{u}_{ship}\left(i_1, j_1, k_1\right) x_d \tag{3.9}$$

$$x_d = \frac{x - x_{ship}\left(i_0\right)}{x_{ship}\left(i_1\right) - x_{ship}\left(i_0\right)} \tag{3.10}$$

$$y_d = \frac{y - y_{ship}\left(j_0\right)}{y_{ship}\left(j_1\right) - y_{ship}\left(j_0\right)} \tag{3.11}$$

$$z_d = \frac{z - z_{ship}\left(k_0\right)}{z_{ship}\left(k_1\right) - z_{ship}\left(k_0\right)} \tag{3.12}$$

The capabilities of this ship airwake coupling approach are described in Chapter 6.

3.3 Boundary Condition Improvements

3.3.1 Implementation of Unsteady Pressure

To ensure the accuracy of such complex cases as shipboard landings, it was important to develop a robust and physically consistent uRANS boundary condition so that the CHARM solution accurately impacts the OVERFLOW solution. Originally, the far field boundary condition in OVERFLOW-CHARM applied the instantaneous induced velocities from the CHARM wake to update the boundary velocities and extrapolated the density and pressure from their steady free-stream values using isentropic relations. This fails to take into account unsteady information that is available in the free-wake solution. Pressure and density are now computed using the unsteady potential function predicted by CHARM:

$$p = \frac{1}{2}\rho_\infty \left(U_\infty^2 - U_{induced}^2 - 2\frac{\partial \phi}{\partial t}\right) + p_\infty \tag{3.13}$$

$$\rho = \rho_\infty + \frac{1}{a_\infty^2}\left(p - p_\infty\right), \tag{3.14}$$

Table 3.1: Propeller thrust coefficient as predicted by OVERFLOW, OVERFLOW-CHARM with isentropic boundary pressure, and OVERFLOW-CHARM with unsteady free-wake boundary pressure

	Thrust Coeff.
OVERFLOW	0.23048
OVERFLOW-CHARM (Isentropic Pressure)	0.22644 (-1.91%)
OVERFLOW-CHARM (Unsteady F-W Pressure)	0.23151 (+0.29%)

which improves the accuracy of the boundary condition when the boundary is immersed in a highly unsteady portion of the flow field and is critically important for computing wake-induced loads on a fuselage. When applied to OVERFLOW-CHARM analysis of an integrated propulsion system configuration, deriving pressure from $\frac{\partial \phi}{\partial t}$ results in a six-fold improvement in propeller thrust prediction accuracy over the isentropic method, as detailed in Table 3.1. Computing $\frac{\partial \phi}{\partial t}$ adds approximately 25% to the cost of computing induced conditions at the uRANS boundary points. However, the induced velocity calculation constitutes such a small percentage of the overall cost of an OVERFLOW-CHARM simulation that the effect on total computation time is negligible, especially considering the substantial increase in prediction accuracy.

3.3.2 Treatment of Characteristics

In previous implementations, a standard preconditioned Characteristic Boundary Condition (CBC) based on Riemann invariants (henceforth referred to as a standard CBC) was applied after setting the boundary values to the CHARM-induced conditions. This mimics the conventional far field boundary treatment in OVERFLOW. The algorithm for setting boundary values $\vec{Q}^{(r)}$ based on internal point values $\vec{Q}^{(i)}$ and external point values $\vec{Q}^{(o)}$ is

$$\vec{Q}^{(r)} = \vec{\overline{Q}} - \frac{1}{2}\boldsymbol{M}\boldsymbol{X}sign(\boldsymbol{\Lambda})\boldsymbol{X}^{-1}\boldsymbol{M}^{-1}\Delta\vec{Q}, \quad (3.15)$$

where

$$\vec{\bar{Q}} = \frac{\vec{Q}^{(o)} + \vec{Q}^{(i)}}{2}, \tag{3.16}$$

$$\Delta\vec{Q} = \frac{\vec{Q}^{(o)} - \vec{Q}^{(i)}}{2}, \tag{3.17}$$

and

$$\boldsymbol{M} = \begin{bmatrix} \frac{1}{T} & 0 & 0 & 0 & -\frac{\rho}{T} \\ \frac{u}{T} & \rho & 0 & 0 & -\frac{\rho u}{T} \\ \frac{v}{T} & 0 & \rho & 0 & -\frac{\rho v}{T} \\ \frac{w}{T} & 0 & 0 & \rho & -\frac{\rho w}{T} \\ \frac{U^2}{(\gamma-1)T} & \rho u & \rho v & \rho w & -\frac{\rho U^2}{T} \end{bmatrix}, \tag{3.18}$$

$$\boldsymbol{X} = \begin{bmatrix} 0 & 0 & 0 & -\frac{A_5}{2s_k} & \frac{A_4}{2s_k} \\ 0 & -\hat{n}_x & \hat{n}_y & \frac{\hat{n}_x}{2\rho s_k} & -\frac{\hat{n}_x}{2\rho s_k} \\ \hat{n}_z & 0 & -\hat{n}_x & \frac{\hat{n}_y}{2\rho s_k} & -\frac{\hat{n}_y}{2\rho s_k} \\ -\hat{n}_y & \hat{n}_x & 0 & \frac{\hat{n}_z}{2\rho s_k} & -\frac{\hat{n}_z}{2\rho s_k} \\ \hat{n}_x & \hat{n}_y & \hat{n}_z & -\frac{(\gamma-1)A_5}{2\gamma\rho s_k} & \frac{(\gamma-1)A_4}{2\gamma\rho s_k} \end{bmatrix}, \tag{3.19}$$

where $\hat{n} = \hat{n}_x\hat{i} + \hat{n}_y\hat{j} + \hat{n}_z\hat{k}$ is the Cartesian vector normal to the boundary face and

$$A_4 = \frac{1}{2}\left(\vec{u}\cdot\hat{n}\right)(1-\beta) + s_k, \tag{3.20}$$

$$A_5 = \frac{1}{2}\left(\vec{u}\cdot\hat{n}\right)(1-\beta) - s_k, \tag{3.21}$$

$$s_k = \sqrt{\frac{1}{2}\left(\vec{u}\cdot\hat{n}\right)^2(1-\beta)^2 + \beta c^2}, \tag{3.22}$$

and finally,

$$\mathbf{\Lambda} = \begin{bmatrix} \lambda_1 & 0 & 0 & 0 & 0 \\ 0 & \lambda_1 & 0 & 0 & 0 \\ 0 & 0 & \lambda_1 & 0 & 0 \\ 0 & 0 & 0 & \lambda_2 & 0 \\ 0 & 0 & 0 & 0 & \lambda_3 \end{bmatrix}, \tag{3.23}$$

where

$$\lambda_1 = \vec{u} \cdot \hat{n}, \tag{3.24}$$

$$\lambda_2 = \frac{1}{2} \left(\vec{u} \cdot \hat{n} \right) \left(1 + \beta \right) + s_k, \tag{3.25}$$

and

$$\lambda_3 = \frac{1}{2} \left(\vec{u} \cdot \hat{n} \right) \left(1 + \beta \right) - s_k. \tag{3.26}$$

The motivation for this boundary condition is to prevent reflections of out-going characteristics back into the uRANS domain. These characteristics can be split in to convective (λ_1) and pressure wave (λ_2, λ_3) characteristics. Taking the sign of $\mathbf{\Lambda}$ serves as a test for which characteristics are leaving the uRANS domain and to treat them appropriately to prevent their reflection.

This formulation of a far-field boundary condition is intended to be applied when $\vec{Q}^{(o)}$ represents freestream values of the flow variables. In most applications, either the far-field boundary will be far enough away that $\vec{Q}^{(i)} \simeq \vec{Q}^{(o)}$, or if not, $\vec{Q}^{(i)}$ will be a better approximation of the desired outflow boundary condition than $\vec{Q}^{(o)}$. For example, if the uRANS boundary is intended to represent the freestream, it is generally recommended that the boundary be far enough away that perturbations caused by the presence of the body of interest have dissipated sufficiently before reaching the boundary. Thus, there is very little discrepancy between the freestream values of $\vec{Q}^{(o)}$ and the interior cell values of $\vec{Q}^{(i)}$. In applications where it is not possible to have the the boundary out of the influence of the body wake, e.g. internal flow calculations, extrapolating values from $\vec{Q}^{(i)}$ onto the outflow boundary is acceptable because the alternative is applying the freestream values of $\vec{Q}^{(o)}$, which would be inaccurate when the boundary is immersed in the body wake.

However, in an OVERFLOW-CHARM simulation, $\vec{Q}^{(o)}$ *is* a good estimate for boundary values, even when the boundary is immersed in the rotor wake. Consider the outflow boundary just behind the rotor blade in an OVERFLOW-CHARM simulation. When the CBC is applied after the CHARM boundary condition, the tangential component of the CHARM-induced velocities will be overwritten by those extrapolated from the internal cell. However, the values of the internal cell depend on the boundary condition applied at the previous step, for which the tangential velocities have also been extrapolated. This results in an outflow boundary which has a very weak correlation to the flow conditions computed by CHARM, which accounts for the full wake. The velocities tangential to this boundary are significant for the prediction of the rotor wake flow physics, as the tip vortex- and vortex sheet-induced velocities will be predominantly tangential to this boundary.

To demonstrate the original characteristic boundary condition, a two-bladed rotor in hover was evaluated as shown in Figure 3.4. The uRANS domain is reduced to a rectangular region very close to the blades, and the flow variables on a particular boundary are investigated. As observed in Figure 3.4, CHARM predicts inflow on the majority of the boundary; however, there are some small regions where CHARM predicts outflow. The outflow region of particular interest is outlined in purple. Figure 3.5 shows contours of vorticity normal to the boundary as predicted by CHARM in Figure 3.5a, and then after the application of the standard CBC in Figure 3.5b. There is clearly a non-physical prediction of the vorticity field due to the difference in velocity characteristic treatment between inflow and outflow regions on this boundary.

It is not sufficient to remove the application of the CBC for OVERFLOW-CHARM simulations, because non-physical pressure wave reflections from the uRANS domain boundary can have a non-negligible influence on the rotor loads. While the original CBC has a

Table 3.2: Quality of characteristic treatments for various implementations of the CHARM boundary condition.

	Correlation between Boundary Velocities and Induced Velocities	**Ability of BC to Prevent Wave Reflection**
No CBC	Good	Poor
CBC	Poor	Good
Free-Wake CBC	Good	Good

negative impact on the boundary velocities, it does mitigate these pressure wave reflections, as evidenced by the reduction in magnitude of integrated loads oscillations in Figure 3.6.

To address these two issues, a new free-wake CBC was written that both preserves the CHARM-induced velocities on the uRANS boundary and treats pressure wave characteristics appropriately to mitigate their reflection back into the uRANS domain. This is achieved by setting

$$sign(\mathbf{\Lambda}) = \begin{bmatrix} -1 & 0 & 0 & 0 & 0 \\ 0 & -1 & 0 & 0 & 0 \\ 0 & 0 & -1 & 0 & 0 \\ 0 & 0 & 0 & 1 & 0 \\ 0 & 0 & 0 & 0 & -1 \end{bmatrix}. \tag{3.27}$$

in Equation 3.15, assuming subsonic flow. This ensures that all characteristics are treated identically at the OVERFLOW-CHARM boundary and achieves the desired effect on the vorticity contours and pressure waves, per Figure 3.5c and Figure 3.6, respectively. Table 3.2 breaks the motivation for this new CBC down into its simplest terms.

3.3.3 Boundary Value Interpolation

Because in most applications the CHARM solution is updated much less frequently than the OVERFLOW solution (5-15 degrees per time step compared to 0.25-1 degree per time step, respectively), uRANS boundary values may change significantly when the CHARM wake is updated. This has been observed to cause large, non-physical oscillations in the blade loads at the CHARM update frequency. The oscillations become more pronounced

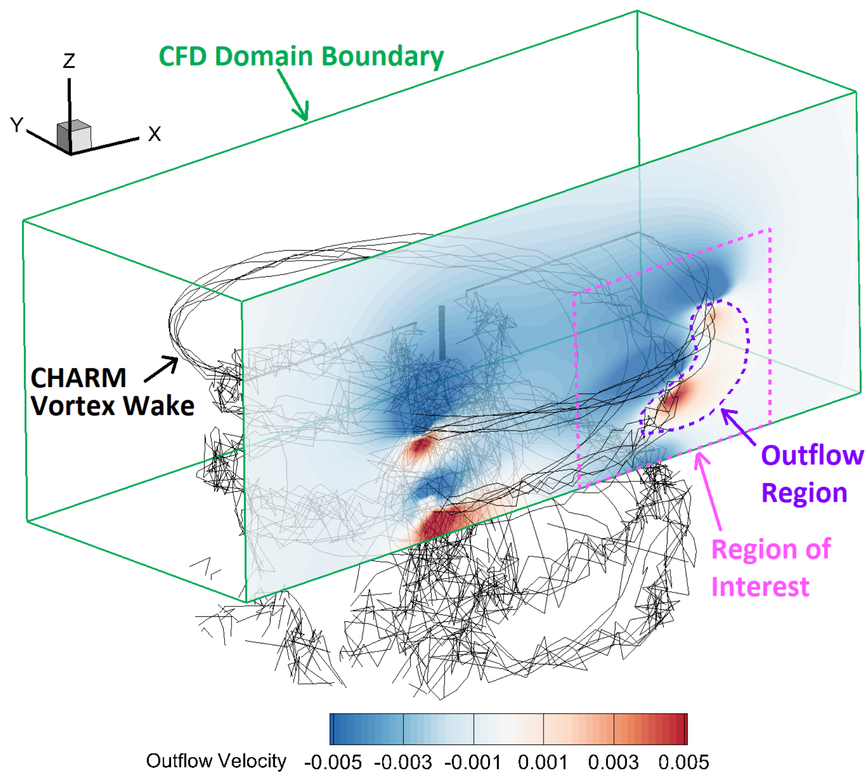

Figure 3.4: Simulation setup for CBC demonstration with contours of CHARM-induced outflow velocity on the boundary of interest.

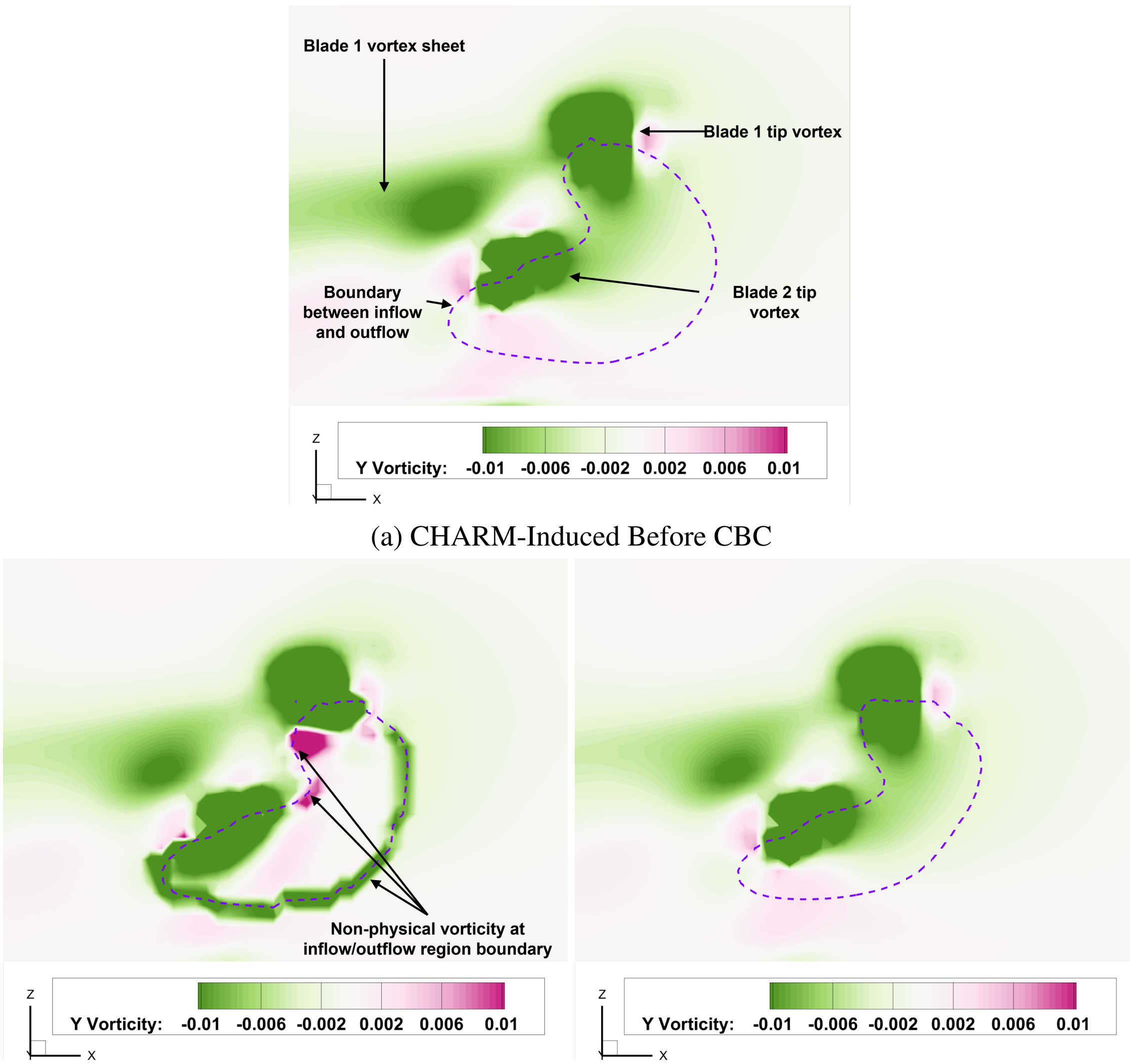

(a) CHARM-Induced Before CBC

(b) Final After Original CBC

(c) Final After Improved CBC

Figure 3.5: Comparison of boundary-normal vorticity contours on the uRANS boundary in an OVERFLOW-CHARM simulation before the application of any CBC and after the application of the original and improved Riemann boundary conditions. See Figure 3.4 for context.

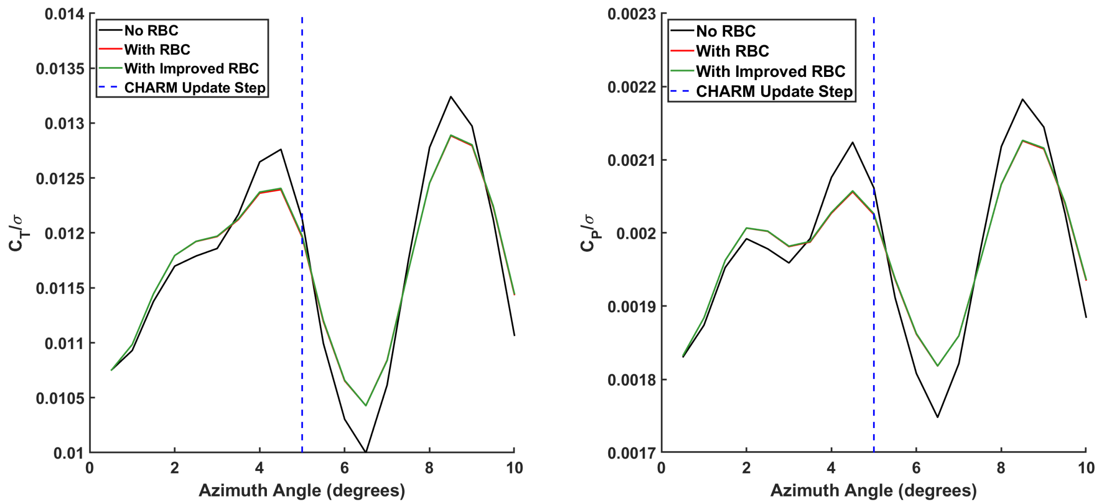

(a) Thrust Coefficient (b) Power Coefficient

Figure 3.6: Comparison of boundary-normal vorticity contours on the uRANS boundary in an OVERFLOW-CHARM simulation before and after the application of the free-wake CBC. Lines for standard and improved CBC are approximately coincident. See Figure 3.4 for context.

as the uRANS boundaries approach the blade. To mitigate these oscillations, CHARM-induced velocities and pressures can be interpolated between CHARM update steps. For example, if the CHARM solution updates every five degrees, at $\psi = 7.5$ degrees, the boundary values will be the average of the values computed at $\psi = 5$ degrees and those computed at $\psi = 10$ degrees. Since the CHARM model will not have reached ten degrees yet, the values at ten degrees need to be predicted. There are two methods that have been investigated to predict these values.

Velocity-Predictive Interpolation (VPI)

The CHARM-induced boundary values that need to be predicted can be set to those computed during the previous revolution, assuming periodicity of the rotor aerodynamics. This reduces the discontinuity in boundary values before and after CHARM update steps and thus improves the quality of OVERFLOW-CHARM results. While pressure is derived from the $\frac{\partial \phi}{\partial t}$ term, because $\frac{\partial \phi}{\partial t}$ can vary significantly during the simulation, interpolating it directly can cause non-physical pressures at the boundary, so pressure is interpolated instead. Referring to Figure 3.7, the velocity at an arbitrary azimuth angle $\vec{u}\,(\psi)$ is computed as:

$$\vec{u}\,(\psi) = a\vec{u}\,(\psi_1) + (1-a)\vec{u}\,(\psi_2), \tag{3.28}$$

where a is the interpolation weight. The red text indicates that $\vec{u}\,(\psi_2)$ is being predicted, and the blue text indicates that $\vec{u}\,(\psi_1)$ is computed during the CHARM update step. The prediction for $\vec{u}\,(\psi_2)$ is

$$\vec{u}\,(\psi_2) = \vec{u}\,(\psi_2 - 360), \tag{3.29}$$

where the green text indicates that $\vec{u}\,(\psi_2 - 360)$ comes from saved data, in this case, from the prior revolution. Pressure is interpolated with the same procedure. Velocity-Predictive Interpolation (VPI) generally reduces oscillations at the CHARM-update frequency, but can require several rotor revolutions before boundary velocities become periodic enough for the effect to be significant.

Force-Predictive Interpolation (FPI)

When the CHARM-predicted rotor wake is insufficiently periodic due to unconverged blade loads or its inherently unsteady nature such as a maneuvering wake, the VPI method still results in discontinuities in boundary values at the CHARM update step. The magnitude of the discontinuity is proportional to the aperiodicity of the CHARM wake. This discontinuity indicates that there are still oscillations in the predicted blade loads and uRANS flow field at the CHARM update frequency, though the oscillations are weaker than with no interpolation at all. Therefore, a new method for predicting velocities was devised. Instead of applying boundary values computed during the previous revolution, the CHARM model leads the OVERFLOW solution by one update step. Because the CHARM model is ahead of the OVERFLOW solution, the blade lift distribution required to generate the wake must be predicted. The current implementation predicts the loads to be those computed when the previous blade passed through that azimuth angle. Boundary values can then be interpolated exactly, since the induced conditions at CHARM update angles before and after the current angle are both known. This results in an interpolation between computed and predicted boundary values that is always smooth. The trade-off is that the OVERFLOW solution "lags" the CHARM solution by one blade passage, which is acceptable for periodic cases. Referring to Figure 3.7b, the flow conditions at an arbitrary azimuth angle $\vec{u}\,(\psi)$ are computed as:

$$\vec{u}\,(\psi) = a\vec{u}\,(\psi_1) + (1-a)\vec{u}\,(\psi_2). \tag{3.30}$$

No terms are being predicted in this equation, ensuring that there are no discontinuities at the update steps. Instead, the blade lift distribution at the next update step $F_{blade1}\,(\psi_2)$ is predicted as:

$$F_{blade1}\,(\psi_2) = F_{blade2}\,(\psi_2). \tag{3.31}$$

The advantages of Velocity-Predictive Interpolation and Force-Predictive Interpolation are illustrated in Figure 3.8, where it can be seen that both methods reduce the discontinuity in the boundary velocities compared to no interpolation. However, if there is any difference in the computed velocity and the predicted velocity (black and red dots, respectively), VPI can still result in some temporal discontinuities at the boundary proportional to that difference. Force-Predictive Interpolation (FPI), in contrast, always creates temporally continuous boundary velocities.

Validation of FPI

The benefits of FPI were demonstrated using a vortex advection case where two-rev periodicity is present due to pairing of the tip vortices shed from a single sub-scale S76 rotor blade as observed in Figure 3.9. In this simulation, the OVERFLOW domain is a single 100×100×101 box grid which is static in space below the initial rotor blade position. It extends from 0.54 rotor radii (R) to 1.43R in the blade spanwise direction, -0.41R to 0.30R

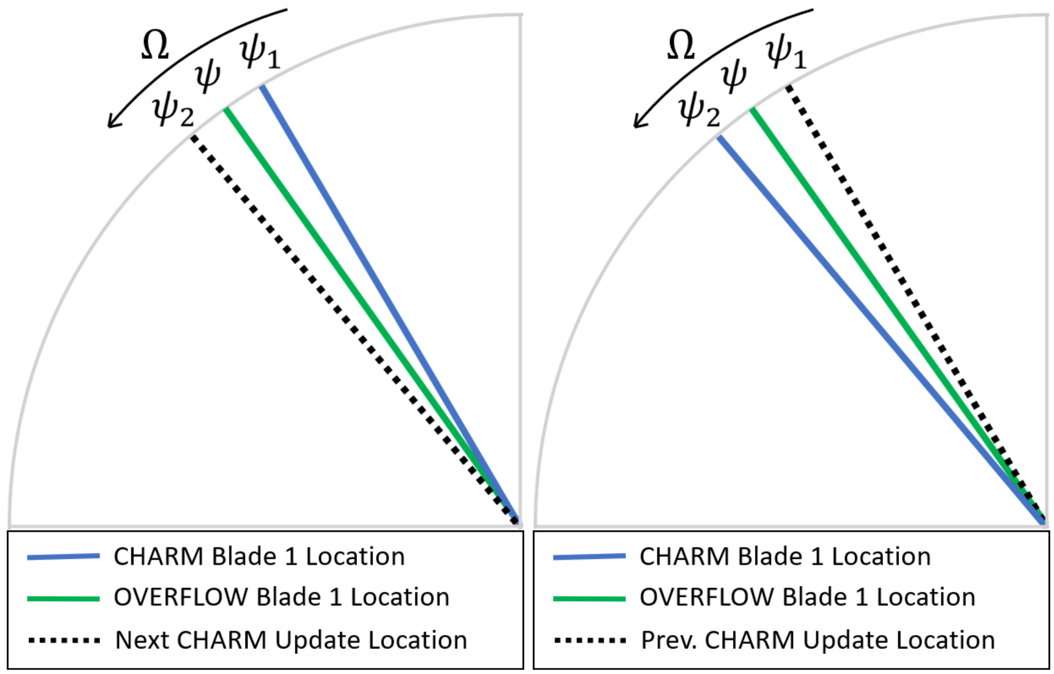

(a) VPI (b) FPI

Figure 3.7: Illustration of definitions for ψ, ψ_1, and ψ_2 in Equation 3.28-Equation 3.31.

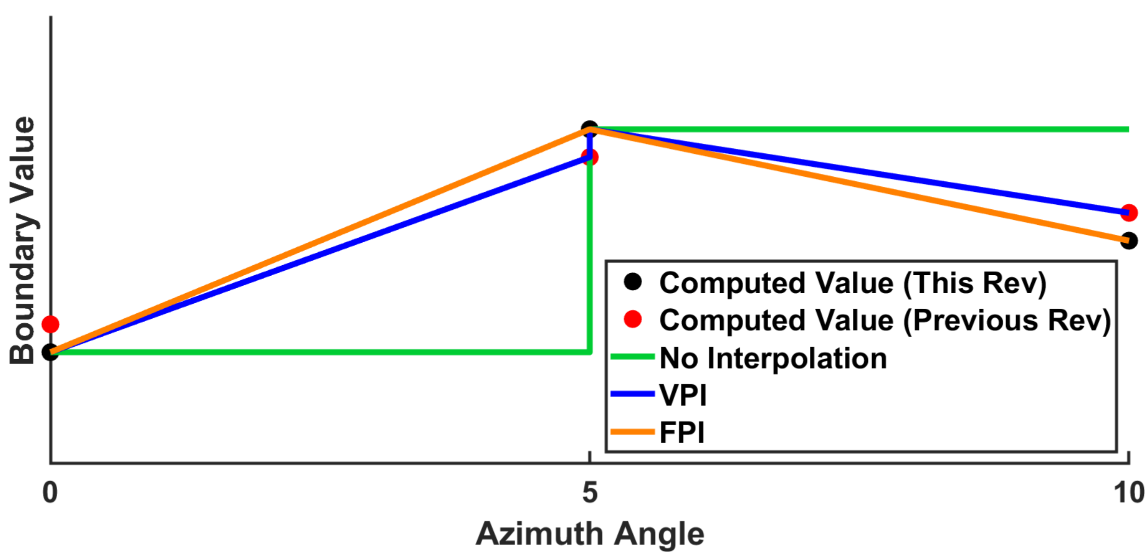

Figure 3.8: Interpolation quality without interpolation, with VPI, and with FPI.

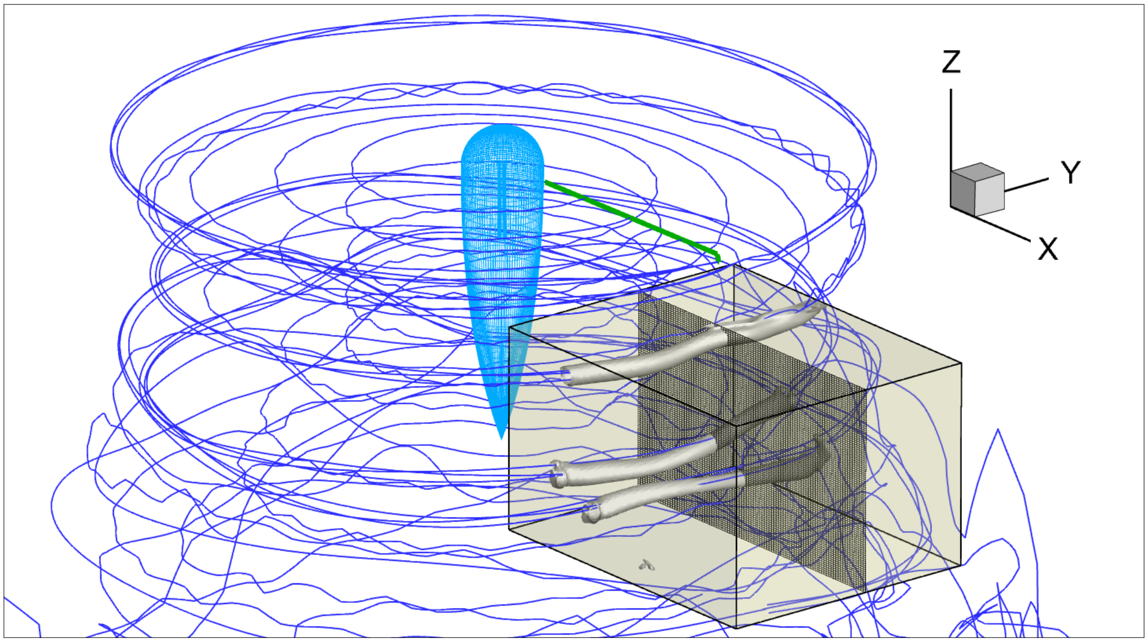

Figure 3.9: Setup of vortex advection scenario. OVERFLOW region boundaries are colored by Q-criterion, CHARM vortex wake is in blue, and the rotor blade is in green. The shown slice is used for visualization.

in the blade chordwise direction, and -0.71R to -0.18R in the vertical direction. Grid points are clustered around the path of the blade tip vortices. Blade forces are pre-computed and do not change as the simulation progresses to focus analysis on the induced flow field within the region of interest. The flow field is initialized as the conditions induced by the CHARM rotor wake to accelerate convergence and minimize initial transients in the uRANS solution.

Time advancement is performed using Euler implicit dual time stepping with 39 subiterations and a constant CFL number of 10. The time step corresponds to 0.25 degrees of rotation of the rotor blade, which translates to approximately 3000 steps for a vortex to advect through the computational domain. The right-hand-side terms were discretized using the fourth-order Roe upwind spatial differencing with 4/2 TLNS3D dissipation where the fourth- and second-order dissipation constants were 0.04 and 2.0, respectively. The left-hand-side terms were discretized using an ARC3D diagonalized Beam-Warming scalar pentadiagonal scheme with fourth-order TLNS3D dissipation. The one-equation Spalart-

Allmaras turbulence model was used with a rotational correction. The reference condition was the rotor tip, with a Mach number of 0.65 and a Reynolds number per inch of 120,000. The CHARM vortex wake is resolved with 360 vortex elements per filament and is updated every five degrees. This corresponds to removal of vortex elements when they reach a wake-age of five revolutions. Root and tip filaments are preserved for an additional five revolutions.

Applying VPI to this case results in very strong oscillations in the solution at the CHARM update frequency, and are sufficiently large enough to impact the advection rate of the vortices. When FPI is applied, however, these oscillations nearly disappear (Figure 3.10). With VPI, the pressure field is dominated by the oscillations resulting from the discontinuity in boundary values at the update frequency. With FPI, pressure field accurately resolves the low pressure inside the vortices with no significant artifacts from the coupling procedure.

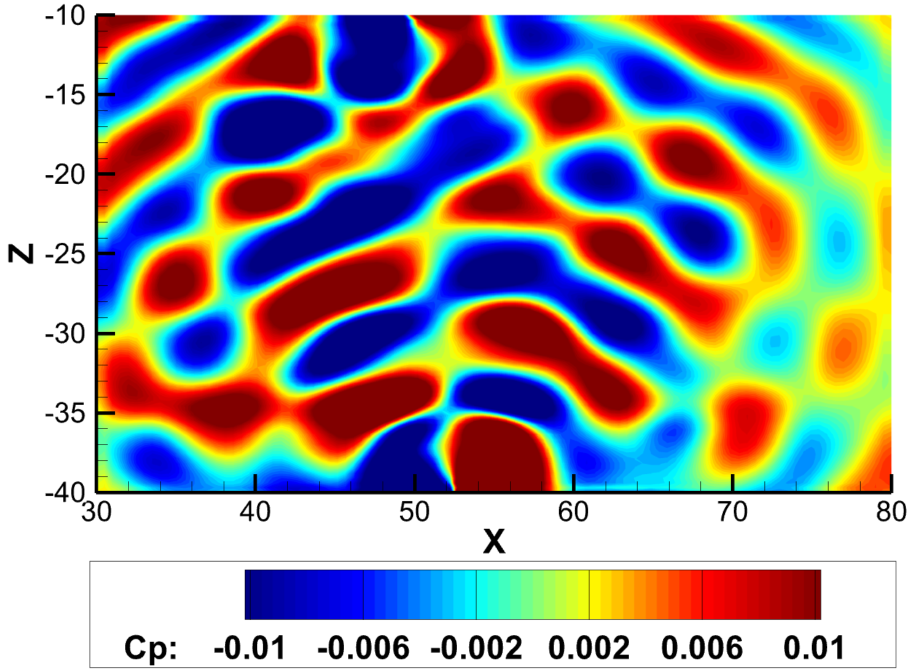

(a) With VPI

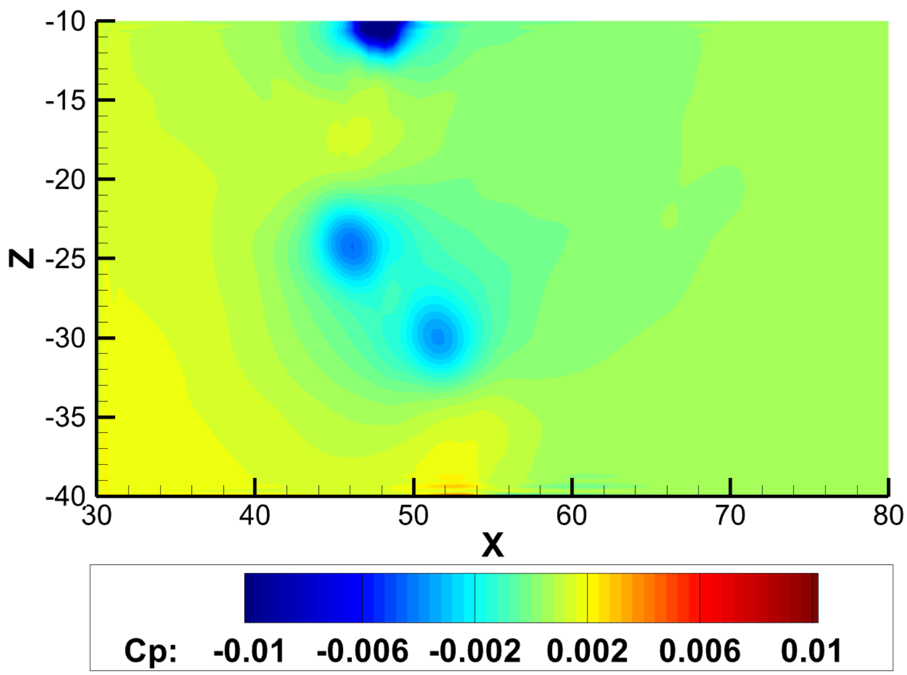

(b) With FPI

Figure 3.10: Comparison of pressure fields on a hub plane slice for the vortex advection case at $\psi = 270°$, where the blade is at z = 0 just above the slice (see Figure 3.9).

CHAPTER 4
WING-WAKE AERODYNAMIC INTERACTIONS

4.1 Introduction

One of the major challenges in the ship-helicopter dynamic interface is the complexity of the interactional aerodynamics between the rotor and other aerodynamic components of the rotorcraft such as a wing, tail, or secondary rotor. While many of these interactions involve complex viscous phenomena, CHARM has been shown to predict rotor wake impingement effects on the fuselage and empennage of rotorcraft with acceptable fidelity for flying quality assessment [121]. OVERFLOW-CHARM also provides the ability to resolve particular components with Computational Fluid Dynamics (CFD) if viscous effects are expected to have a strong influence on quantities of interest along with its conventional advantage of highly accurate computed rotor blade loads. A wing-integrated propeller configuration is used as a basic example of the combination of rotating and static aerodynamic systems which are present on modern rotorcraft designs. Wind-tunnel predictions of the aerodynamics of this model are available to be used for validating computational results.

4.2 Experimental Configuration

To encourage expansion of computational tools and to determine their capabilities in performing integrated propulsion analysis, the American Institute of Aeronautics and Astronautics (AIAA) Workshop for Integrated Propeller Prediction (WIPP) was organized. A team effort between Helden Aerospace, Empirical Systems Aerospace, and the National Aeronautics and Space Administration (NASA) performed wind tunnel tests on a wing-integrated propeller configuration with a 10% scale C-130 four-bladed propeller mounted on the tip of a 40.5% scale semi-span wing model measured relative to the X-57 demon-

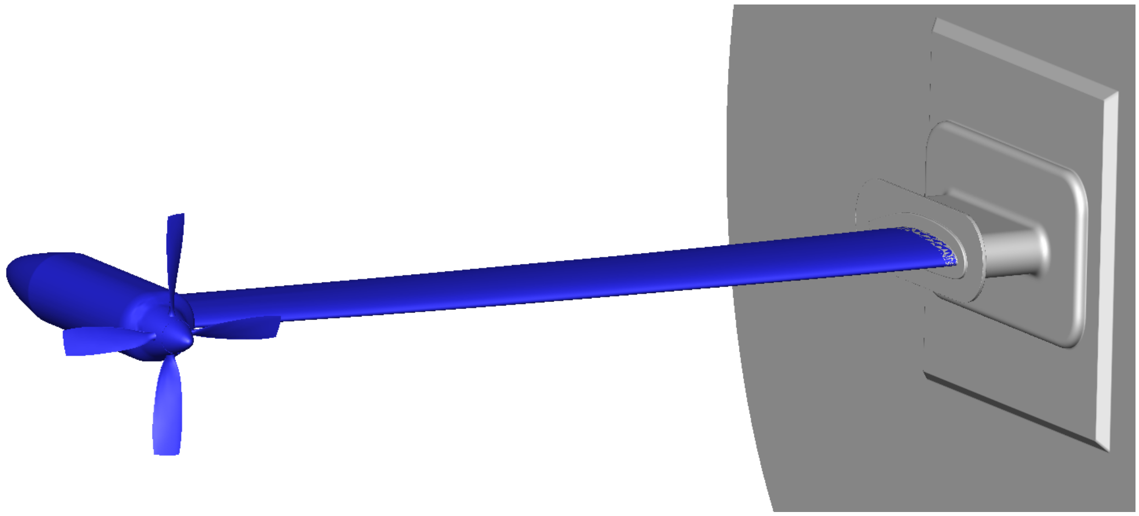

Figure 4.1: WIPP configuration geometry. Integrated forces are reported on surfaces highlighted in blue (via Moushegian et al. [138]).

strator. The experimental configuration is shown in Figure 4.1. The wing was swept and tapered with a root chord of 11.6 inches, a tip chord of 8.6 inches, and a leading-edge sweep angle of 1.9 degrees.

Tests were performed in the Lockheed Martin Low-Speed Wind Tunnel (LSWT) at a range of propeller thrust, component, and freestream conditions totaling 197 runs. Of these, a small subset was chosen for focused computational analysis. This analysis focuses on run number 180, which had at a free-stream Mach number of 0.08 and a nominal propeller thrust coefficient of 0.4 for angles of attack ranging between -10 to 17 degrees in one degree increments. The nominal propeller thrust coefficient is based on uninstalled calibration data from Lockheed Martin and is not necessarily consistent with the measured thrust value. Computational predictions are therefore compared to the experimentally measured thrust. Propeller thrust in the experiment was calculated using wake momentum measurement, and is the value compared with present computational results. Data gathered during run 180 also included thrust-corrected wing lift and drag, wing airfoil pressure coefficient data at various spanwise locations (see Figure 4.10), and measured freestream and propeller RPM conditions at each angle of attack (Table 4.1) [139].

Table 4.1: Table of conditions for experimental run number 180.

α (°)	M_∞	M_{tip}	ρ_∞ (kg/m^3)	p$_\infty$ (Pa)
0.0721	0.08266	0.3749	1.1778	96849.8
3.0958	0.08258	0.3746	1.1780	96849.8
5.1089	0.08268	0.3734	1.1781	96851.1
7.1167	0.08271	0.3727	1.1784	96851.1
11.133	0.08267	0.3716	1.1781	96855.1

4.3 Simulations

The application of OVERFLOW-CHARM to an integrated propulsion configuration involved a study of optimal grid reduction strategies, selection of turbulence modeling, and boundary value interpolation schemes through parametric studies at the zero angle of attack condition. Once these parameters were determined, an angle of attack sweep was performed, comparing the propeller and wing aerodynamic predictions to those of a conventional OVERFLOW simulation and experimental data. Results were also compared to data from Aref et al. [140] and Baruzzi et al. [141] where available. The convergence criterion for all simulations performed here was met when the mean difference in propeller thrust over one blade passage varied by less than 0.05% with respect to the previous blade passage, or

$$cc = \overline{\left| \frac{C_T(\psi)}{C_T(\psi - 90°) - 1} \right|} < 0.0005. \tag{4.1}$$

OVERFLOW simulations were initialized with a non-rotating 3240-step steady-state simulation at the end of which the wing lift had converged to a constant value. Restarting from this solution helped to accelerate convergence of the wing aerodynamics in the unsteady simulations. The flow field in OVERFLOW-CHARM simulations was initialized with the freestream conditions. All simulations were performed on the Department of Defense (DoD) High-Performance Computing Modernization Program (HPCMP) cluster Centennial on 240 Intel Xeon E5-2698v4 Broadwell Cores running at 2.2GHz.

4.3.1 Computational Meshes

Workshop participants were provided a structured overset computational grid system on which to perform CFD simulations. This mesh contained 35.1 million grid points (after parallel decomposition) and resolved the propeller blades, nacelle, wing, and splitter plate geometries present in the experiment. These computational geometries were generated from laser scans of the experimental apparatus. Due to an error in the generation of the provided blade grids, highly-skewed cells were present at the trailing edges of the propeller blades, so the main blade grids were re-generated for this study using the same surface mesh and a marching front technique that ensures high-quality cells in the boundary layer. This was the only modification made to the provided grid system, details of which are given in Table 4.2. The meshes were generated using established best practices with a y^+ value of less than one for the first cell in the boundary layer and points clustered around areas of high geometric curvature and aerodynamic gradients. The blade grids consisted of a main blade grid, a tip grid, and two small grids that resolved the leading and trailing edges of the blade tip which totaled 1.7 million points for each blade. The main blade grids were O-type meshes with 201 points around the airfoil, 101 points along the span, and 57 points in the wall normal direction.

A unique advantage of OVERFLOW-CHARM is the user's ability to choose which components which are resolved by the CFD domain, from a single blade to the full configuration. For the simulations performed, three different CFD domain reductions were applied. All three made use of identical blade grids; the only variation was in the off-blade grid configuration.

For the first configuration, OVERFLOW resolved a small region close to the propeller. The reduced domain resolved an approximately hemispherical region around the propeller, extending 0.22 propeller diameters downstream. This is referred to as the ”near-field” approach and is displayed in Figure 4.2a. The off-body domain consisted of four grids. Two of these grids, one O-H and one H-H topology, resolved the tip of the nacelle with a

Table 4.2: Details of baseline grid system provided to workshop participants

Grid Name	Dimensions	Topology	Total Points
Main Wing	305x58x65	C-H	1.1M
Wing Trailing Edge	45x61x53	H-H	0.1M
Wing-Splitter Cuff	241x77x61	O-H	1.1M
Wing-Nacelle Cuff	301x49x61	O-H	0.9M
Main Splitter	161x149x57	O-H	1.4M
Main Nacelle	201x181x81	O-H	2.9M
Nacelle Nose	41x41x61	H-H	0.1M
Nacelle Tail	25x25x61	H-H	0.04M
Wing Refinement	97x61x65	H-H	0.4M
Nacelle Refinement	161x65x77	H-H	0.8M
Tunnel Volume	121x97x125	H-H	1.5M
Blade Vortex Refinement	241x361x101	O-H	8.8M
Main Blade (x4)	201x101x57	O-H	1.2M
Blade Tip (x4)	57x97x66	H-H	0.4M
Blade Tip LE (x4)	25x37x81	H-H	0.07M
Blade Tip TE (x4)	39x37x79	H-H	0.1M

total of 1.6 million points. Another O-H grid resolved the helical propeller wake and served as the outer boundary of the CFD domain with an additional 3.3 million points. Finally, a small H-H prism grid closed the CFD domain upstream of the propeller. This approach sought to accurately capture the aerodynamics of the propeller blades, particularly where they meet the nose of the nacelle.

In the second configuration, the OVERFLOW domain was further reduced to a disk encompassing only the propeller blade grids. This is called the ”disk” approach and is displayed in Figure 4.2b. The off-body domain consisted of a single, O-H topology grid consisting of 2.2 million points that extended from the nacelle surface to an outer radius of 1.3 propeller radii. The disk approach excluded the area in front of the propeller where there are no complex aerodynamic phenomena to further reduce the point count.

In the final domain, referred to as the ”noncontiguous” approach, the CFD domain consisted solely of the blade grids (Figure 4.2c). Two variants were tested, one with the original blade grids extended to encompass a region 1 chord length away from the blade (“A” variant), and one employing the original blade grids (“B” variant). The noncontiguous

Table 4.3: Comparison of component and total sizes of grid systems for each OVERFLOW-CHARM grid reduction approach to the baseline OVERFLOW grid.

	Blade	Other Body	Off-Body	Total Pts	Boundary Pts
OVERFLOW	6.7M	6.4M	12.8M	26.0M	-
Near-Field	6.7M	1.6M	3.4M	11.8M (-55%)	114k
Disk	6.7M	2.2M	-	9.0M (-65%)	63k
Noncontiguous A	8.1M	-	-	8.1M (-69%)	206k
Noncontiguous B	6.7M	-	-	6.8M (-75%)	206k

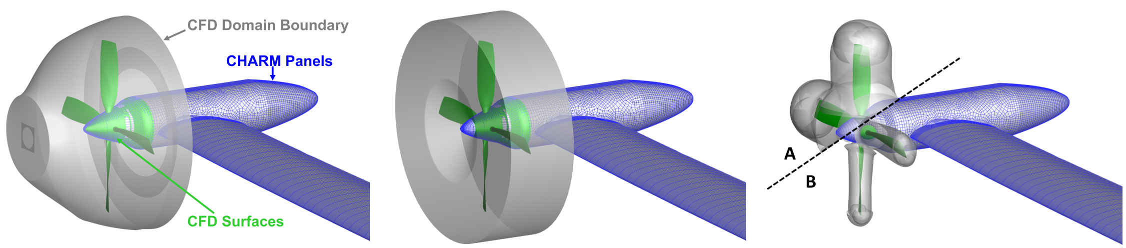

(a) **Near-Field** (b) **Disk** (c) **Noncontiguous**

Figure 4.2: Diagrams of OVERFLOW-CHARM domain setups for the WIPP configuration.

approach represents a configuration where very high cost savings are desired. The details of each grid reduction approach are tabulated in Table 4.3.

The wing and nacelle were resolved in the CHARM model as 15,001 triangular and quadrilateral panels, generated by Continuum Dynamics, Inc. The wing surface was resolved with rectangular panels with clustering at the leading edge, and the nacelle surface panels were approximately uniformly distributed with an average panel size of 0.2 inches.

4.3.2 Numerical Options

In the baseline OVERFLOW simulations and in the OVERFLOW portion of OVERFLOW-CHARM simulations, time-advancement was performed with dual time stepping employing up to forty second-order subiterations, a local time step factor of 1.0, and a Courant–Friedrichs–Lewy (CFL) number of five. The physical time step advances the propeller 0.25 degrees per time step. Subiterations were stopped when the residual reduced by two orders of magnitude, as convergence beyond this level did not sufficiently improve results to justify the additional cost. The right-hand-side terms were discretized with second-order central spatial differencing using fourth- and second-order constants of 0.04 and 10.0, respectively. The left-hand-side terms were discretized with a diagonalized Beam-Warming scalar pentadiagonal scheme.

In the hybrid simulations, the CHARM vortex wake was updated every five degrees of propeller rotation, during which new vortex elements were generated and those older than three revolutions were removed. More frequent wake updates are not recommended due to potential instabilities in the CHARM solution. Less frequent updates (every 15 degrees) were observed to degrade the accuracy of dynamic propeller loads. The blade loads that were sent to CHARM by OVERFLOW were initialized from a one-revolution OVERFLOW calculation, and the CHARM vortex wake was initialized without coupling for two revolutions. Once coupling begins, it is important to delay sending CFD loads to CHARM as initial transients can result in large spikes in blade loads. These rapidly changing blade loads would then cause strong disturbances in the CHARM wake. Thus, the initial loads were applied until the initial transients in the OVERFLOW solution had dispersed after one blade passage of coupled simulation. Over the next blade passage, blade loads were smoothly blended between the initial guess and the CFD solution until, by the beginning of the third blade passage, the blade loads were solely from the CFD solution.

Selection of the turbulence model followed a series of parametric studies concurrent with the evaluation of grid extents and boundary value interpolation. Turbulence models evaluated were the Spalart-Allmaras (SA) [142] and Menter Shear-Stress Transport (SST) [143] turbulence models . Rotational corrections and Delayed Detached Eddy Simulation (DDES) formulations of these turbulence models altered integrated loads predictions by less than 0.1% and were thus not applied.

4.3.3 Parametric Study Methodology

The parametric study of turbulence model, grid reduction, and boundary value interpolation was performed in two stages. In stage one, an initial guess for each parameter was employed (k-ω turbulence model, near-field grid reduction, and velocity-predictive interpolation) and each parameter was varied independently as described in Table 4.4. Then, to verify that the results of each study were independent from the others, stage two applies the results of stage one in a second variation per Table 4.5.

4.4 Results

4.4.1 Baseline OVERFLOW results

Comparing the results of the baseline OVERFLOW simulations, which employed the WIPP workshop meshes, with the experimental results, propeller thrust was generally underpredicted by approximately 5% of the experimentally predicted value, as observed in Figure 4.3b. It is unclear whether this was an effect of the computational grid/method or experimental measurement technique, though the choice of turbulence model was a contributing factor (see Figure 4.6) and other workshop participants reported difficulty in matching the experimental propeller thrust with conventional CFD methods. In the experiments, thrust was varied through propeller speed rather than blade trimming, so no trimming procedure was applied in the computational simulations to ensure one-to-one comparison with the experimental data and between computational methods.

The wing lift and drag coefficient predictions were generally within 5 percent of the experiment and compared favorably to predictions from Aref et. al [140] (Figure 4.3a).

Table 4.4: Stage one parametric study simulations

	Turbulence Model	**Grid Reduction**	**Interpolation**
Test 1	SA, k-ω SST	Near-Field	VPI
Test 2	k-ω SST	Near-Field, Disk, Noncontig. A/B	VPI
Test 3	k-ω SST	Near-Field	None, VPI, FPI

Table 4.5: Stage two parametric study simulations

	Turbulence Model	Grid Reduction	Interpolation
Test 1	SA, k-ω SST	Disk	FPI
Test 2	SA	Near-Field, Disk, Noncontig. A/B	FPI
Test 3	SA	Disk	None, VPI, FPI

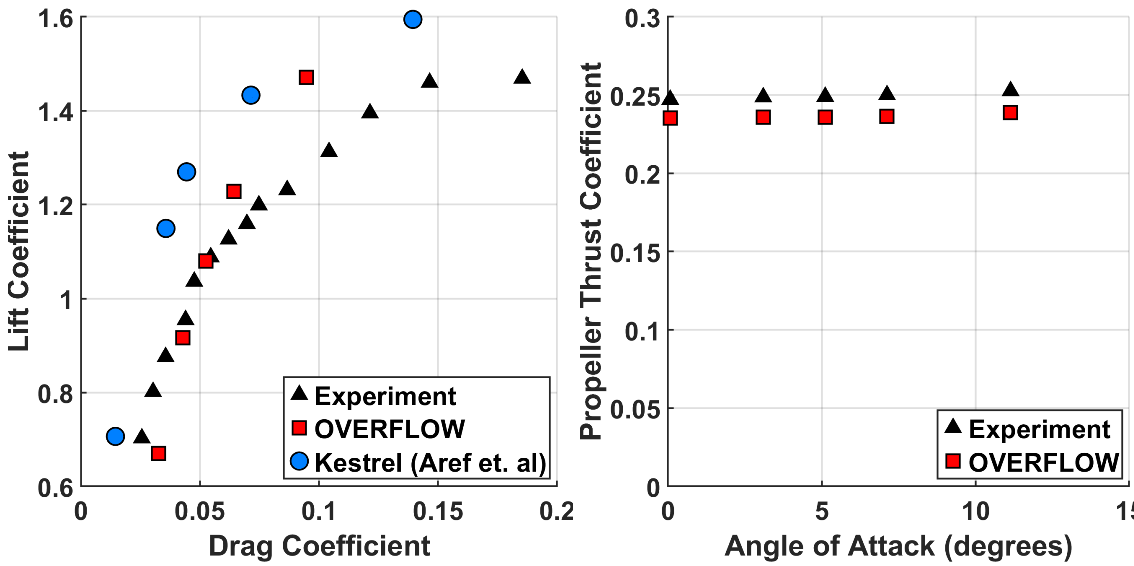

(a) **Drag Polar** (b) **Propeller Thrust**

Figure 4.3: OVERFLOW predictions of wing drag polar and propeller thrust compared to experimental data. Drag polar also compared to simulations using Kestrel with SAMAir off-body grids performed by Aref et al. [140].

Pressure coefficient data varied between $C_p = 0.01$ and 0.3 of Kestrel [144] and Fluent [141] predictions and between 0.05 and 0.65 of experimental data, with the best agreement at BL 57. (Figure 4.4). The deviations from the experimental data in both the drag polar and pressure coefficient predictions were consistent with those observed when applying other CFD methods [140, 141]. Further details of the baseline OVERFLOW results will be discussed in the context of the OVERFLOW-CHARM predictions.

4.4.2 Grid Extents

Examining the propeller performance predictions of each grid reduction strategy, the near-field and disk grid reduction strategies both predicted propeller performance within 0.5% of the baseline OVERFLOW simulation (Table 4.6). The noncontiguous approach overpre-

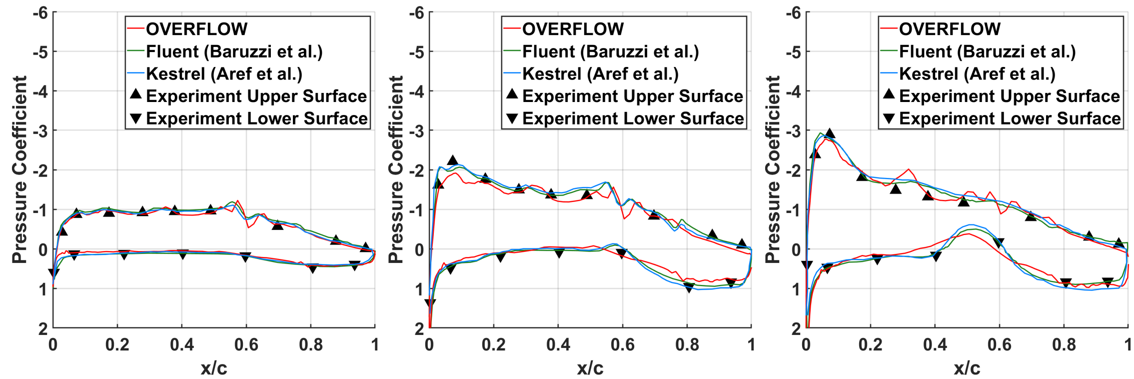

(a) **BL 57** (b) **BL 60.75** (c) **BL 63**

Figure 4.4: Comparison of wing pressure coefficients at $\alpha = 0.07°$ between OVERFLOW, experiment, and computational results of Fluent [141] and Kestrel [140].

dicted the propeller thrust and power, with the smaller B variant introducing significantly more error than the A variant. This is consistent with previously published results where reduction of the CFD grid below a distance of 1 chord from the blade was demonstrated to have a strong impact on integrated force predictions [127]. The flow physics are shown in Figure 4.5, where artifacts appear at the boundary of the B variant noncontiguous domain, and to a lesser extent with the A variant domain, which prevent the propeller wake from developing properly.

These grid configurations make minimal modifications to the point density of the baseline OVERFLOW grid, only cutting or extending existing grids where necessary. When the number of points along the span of the propeller blades and in the disk off-body grid are reduced, an additional 15% reduction in the number of grid points can be achieved with a less than 1% impact on the predicted propeller loads. To simplify comparison to the baseline OVERFLOW simulations, however, the unreduced grids are employed for detailed analysis.

This study demonstrated that including an off-body grid can provide benefits to hybrid simulation fidelity, and that, while incurring some additional computational cost, using the disk approach resulted in performance prediction accuracy within 0.4% of conventional CFD methods while providing 70% cost savings. Cost savings using the disk were the

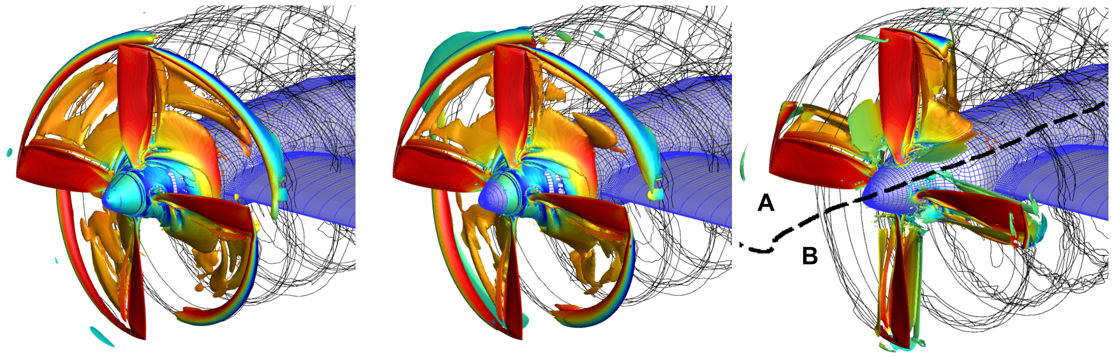

(a) **Near-Field** (b) **Disk** (c) **Noncontiguous**

Figure 4.5: Propeller wake geometry, visualized with CHARM vortex filaments (black) and isosurfaces of q-criterion within the OVERFLOW domain (colored), predicted by OVERFLOW-CHARM with various grid reduction techniques at $\alpha = 0.07°$

result of mesh reduction and faster convergence compared to the baseline OVERFLOW simulations. For these reasons along with the simplicity of the domain, OVERFLOW-CHARM results are presented from simulations employing the disk approach to off-body grid reduction.

4.4.3 Turbulence Model

Because it was observed that applying a rotational correction or DDES formulation to the chosen turbulence model resulted in very little difference in the integrated loads, comparison is made between the SA and k-ω-SST turbulence models. As observed in Figure 4.6, the choice between the one-equation SA model and the two-equation k-ω-SST model had a moderate impact on the propeller performance predicted by OVERFLOW and

Table 4.6: OVERFLOW-CHARM predictions of thrust and power at $\alpha = 0.07°$ with various grid reduction strategies compared to the baseline OVERFLOW predictions.

	Thrust Coefficient	**Power Coefficient**	**Appx. CPU-Hour Cost**
OVERFLOW	0.23523	0.26165	4800
Near-Field	0.23558 (+0.15%)	0.26230 (+0.25%)	2000 (-58%)
Disk	0.23444 (-0.34%)	0.26118 (-0.18%)	1500 (-69%)
Noncontiguous A	0.24504 (+4.17%)	0.27240 (+4.11%)	1350 (-72%)
Noncontiguous B	0.29034 (+23.4%)	0.32467 (+24.1%)	1125 (-77%)

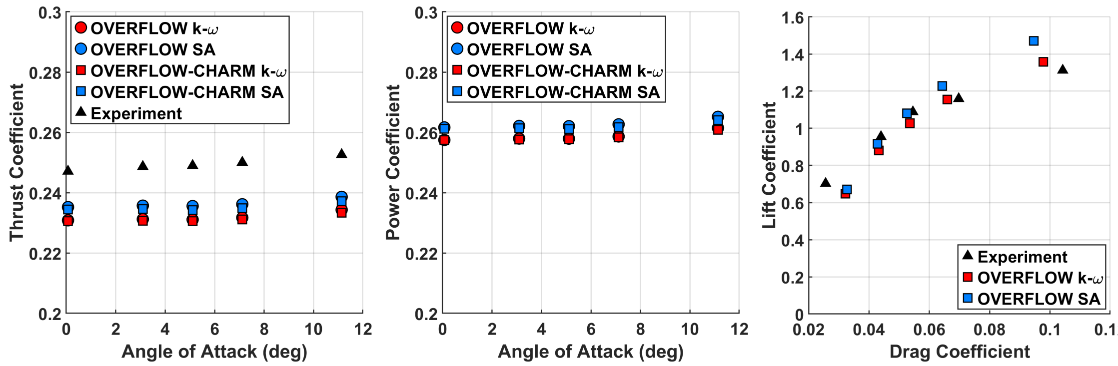

(a) **Propeller Thrust** (b) **Propeller Power** (c) **Wing Drag Polar**

Figure 4.6: Comparison of propeller and wing performance predictions by OVERFLOW and OVERFLOW-CHARM with the k-ω-SST and SA turbulence models.

OVERFLOW-CHARM, and the wing drag polar predicted by OVERFLOW. While higher consistency was observed between OVERFLOW-CHARM and OVERFLOW when applying the k-ω-SST model, the SA model generally provided higher accuracy with respect to the experimental predictions, so the SA model was applied to further simulations in this work.

4.4.4 Boundary Value Interpolation

In the baseline OVERFLOW simulation, the amplitude of propeller thrust oscillations with a frequency of 72/rev is negligible because there are no underlying physics occurring at this frequency. Running OVERFLOW-CHARM without boundary value interpolation results in propeller thrust oscillations at the CHARM update frequency (72/rev), as observed in Figure 4.7. Table 4.7 tabulates how each interpolation scheme impacts the amplitude of the non-physical 72/rev oscillations associated with CHARM updates and whether they impact the major 1/rev and 4/rev amplitudes as predicted by OVERFLOW. Velocity-Predictive Interpolation (VPI) only begins to mitigate the 72/rev oscillations at the last blade passage of the simulation and only reduces the amplitude by about half. With Force-Predictive Interpolation (FPI), the amplitude of oscillations drops by an order of magnitude, but an additional 1/rev oscillation is created. This is caused by initial transients in the CFD so-

Table 4.7: Means values and non-physical frequency amplitudes in propeller thrust predictions by OVERFLOW and OVERFLOW-CHARM with various interpolation schemes applied. Error in mean thrust is relative to the OVERFLOW prediction.

	Mean Thrust	**1/rev Amp.**	**72/rev Amp.**
OVERFLOW	0.2354	1.69e-4	4.73e-7
No Interpolation	0.23438 (-0.4%)	2.74e-5	2.84e-4
VPI	0.23453 (-0.4%)	9.28e-5	1.08e-4
FPI	0.23458 (-0.3%)	1.00e-4	4.64e-5
FPI with delay	0.23442 (-0.4%)	2.19e-5	4.98e-5

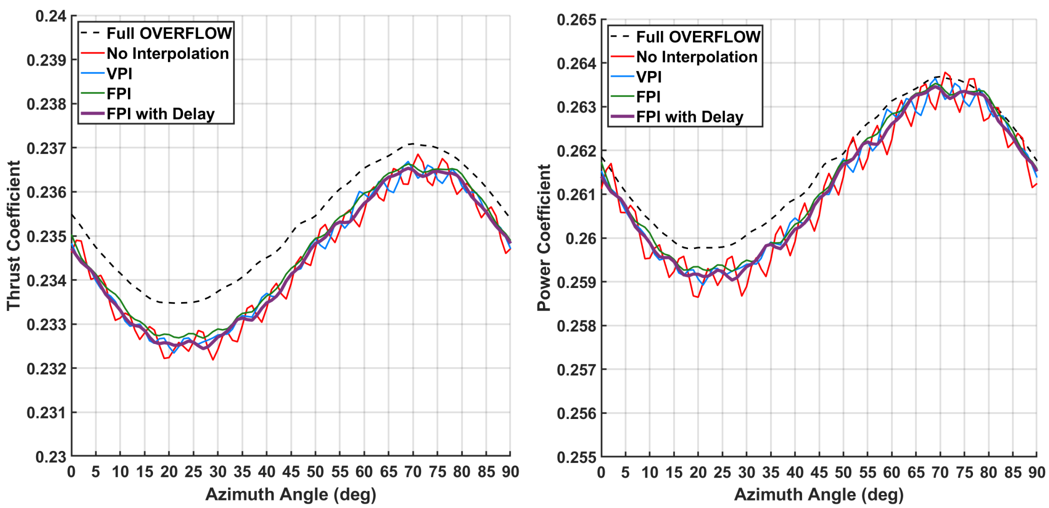

(a) **Propeller Thrust** (b) **Propeller Power**

Figure 4.7: Propeller thrust and power variation over one blade passage predicted by OVERFLOW and OVERFLOW-CHARM with various boundary value interpolation schemes applied. Thrust axis enlarged to highlight oscillations. Error between mean OVERFLOW and OVERFLOW-CHARM predictions is less than 0.4%.

lution being propagated throughout the simulation because of the ninety-degree lag between when blade forces are computed by OVERFLOW and when they are applied to the CHARM model. This lag is inherent to the FPI formulation, but should be acceptable if the solution is periodic. The 1/rev oscillation can be prevented by starting FPI after one revolution with no interpolation to allow initial transients to be eliminated before introducing the aforementioned lag in the CHARM blade loads. Because this approach eliminates the 1/rev oscillation without sacrificing the mitigation of oscillations at the CHARM update frequency, further simulations apply FPI after one revolution of no interpolation.

4.4.5 Propeller Performance

Table 4.8 compares the thrust and power coefficients predicted by OVERFLOW and OVERFLOW-CHARM for various angles of attack. Agreement between these predictions was very strong, within 1%. Inspection of the variation of thrust produced by a single blade with azimuth angle demonstrates how the presence of the wing in the CHARM model impacted the propeller performance. If nonlinear effects of the wing on the propeller are being captured by OVERFLOW-CHARM, it will present as a deviation in the "Nonlinear Thrust Delta" ($NLT\Delta$), defined as

$$NLT\Delta\left(\psi\right) = C_{T,\alpha}\left(\psi\right) - C_{T,alpha_0}\left(\psi\right) - A_1 sin(\psi + \theta_1). \tag{4.2}$$

Here, $C_{T,\alpha}\left(\psi\right)$ and $C_{T,\alpha_0}\left(\psi\right)$ are the blade thrust variation at angles of attack α and $\alpha = 0$, respectively. Linear aerodynamic effects of angle of attack on $C_{T,\alpha}\left(\psi\right) - C_{T,alpha_0}\left(\psi\right)$ should be a sine wave based on blade-element momentum theory. To isolate purely nonlinear effects, the linear effect of angle of attack is estimated as the first term in the Fourier series

$$C_{T,\alpha}\left(\psi\right) - C_{T,alpha_0}\left(\psi\right) = \frac{A_0}{2} + \sum_{n=1}^{\infty} A_n sin(n\psi + \theta_n). \tag{4.3}$$

After subtracting the first term, what is left is the $NLT\Delta$, which can alternatively be defined as

$$NLT\Delta\left(\psi\right) = \frac{A_0}{2} + \sum_{n=2}^{\infty} A_n sin(n\psi + \theta_n). \tag{4.4}$$

Figure 4.8a demonstrates that, without the presence of the wing, OVERFLOW-CHARM does not capture the deviation in $NLT\Delta$ as the blade passes over the wing. When the wing is included in the OVERFLOW-CHARM configuration, however, OVERFLOW-CHARM predicts $NLT\Delta$ consistently with OVERFLOW. With regard to the dynamics of the total propeller thrust, the amplitude and phase of the 4/rev oscillation resulting from blade passage over the wing are compared between OVERFLOW and OVERFLOW-CHARM in

Table 4.8: Comparison of predicted thrust and power coefficients between OVERFLOW and OVERFLOW-CHARM with percent error calculated relative to the OVERFLOW value.

α (°)	OF Alone C_T	OF-CHARM C_T	OF Alone C_P	OF-CHARM C_P
0.0721	0.23586	0.23444 (-0.60%)	0.26219	0.26118 (-0.39%)
3.0958	0.23627	0.23461 (-0.70%)	0.26263	0.26140 (-0.47%)
5.1089	0.23610	0.23428 (-0.77%)	0.26253	0.26114 (-0.53%)
7.1167	0.23667	0.23485 (-0.77%)	0.26311	0.26171 (-0.47%)
11.133	0.23906	0.23716 (-0.79%)	0.26555	0.26405 (-0.57%)

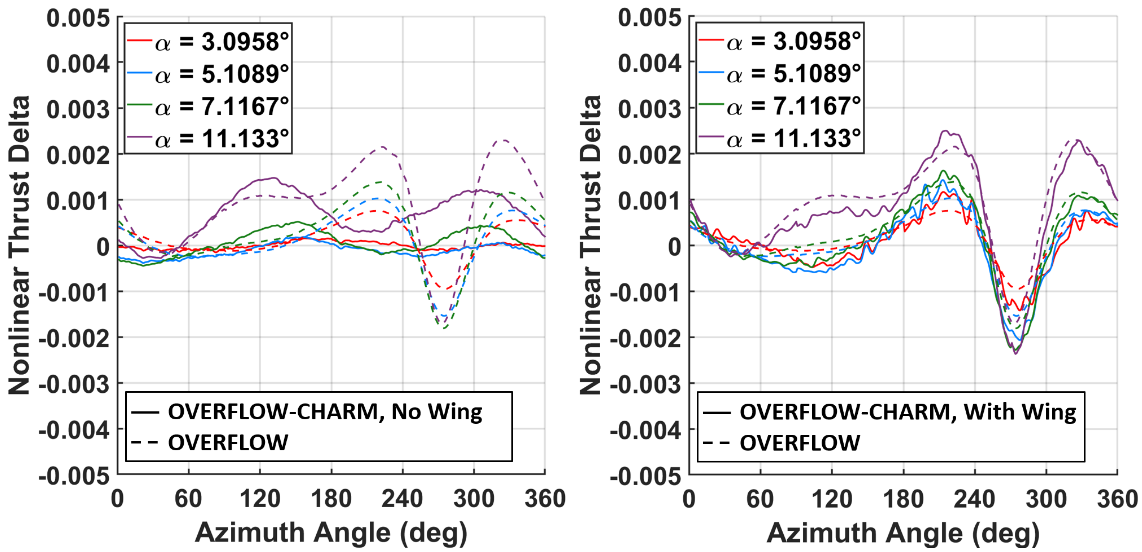

(a) **No Wing**

(b) **With Wing**

Figure 4.8: OVERFLOW-CHARM prediction of nonlinear thrust delta ($NLT\Delta$) in blade thrust coefficient (Equation 4.2) variation over azimuth angle at various angles of attack compared to first term in Fourier series.

Figure 4.9. The mean propeller thrust predictions are within 0.5% between OVERFLOW and OVERFLOW-CHARM. The amplitude was overpredicted by OVERFLOW-CHARM, approximately 15-20% higher than that predicted by OVERFLOW (See Figure 4.9b), however the variation of the phase with angle of attack was in very good agreement, within one to two degrees of the OVERFLOW predictions. The overprediction of thrust amplitude is caused by higher back pressure predicted at the OVERFLOW-CHARM boundary in front of the wing leading edge relative to the OVERFLOW simulation.

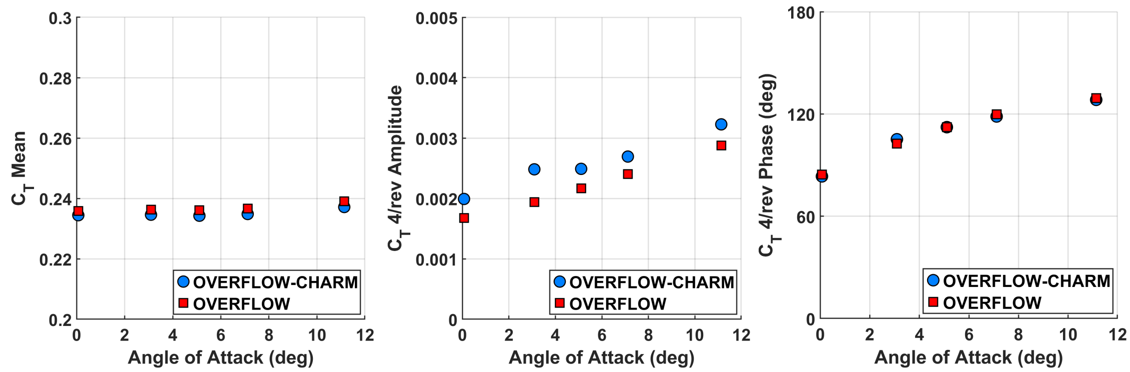

(a) **Mean** (b) **Amplitude** (c) **Phase**

Figure 4.9: OVERFLOW and OVERFLOW-CHARM predictions of mean, 4/rev amplitude and 4/rev phase of propeller thrust coefficient at various angles of attack.

4.4.6 Wing Performance

Wing performance was predicted by CHARM using a panel method. As mentioned previously, wake panels were shed from the sharp trailing edge of the wing to predict the effect of wing lift on the flow field. The pressure coefficient was computed at the center of each surface panel using the combined influence of the freestream conditions, propeller vortex wake, and shed wake panels using:

$$C_p = 1 - \frac{U_t^2}{U_\infty^2} - \frac{2}{U_\infty^2}\frac{\partial \phi}{\partial t}. \tag{4.5}$$

The total lift coefficient was computed by integration of this pressure coefficient over all of the panels, including the nacelle, which matched the metric bodies in the experimental data.

The lift variation with angle of attack is given in Table 4.9, and the pressure coefficient at four spanwise stations and each angle of attack are given in Figure 4.11-Figure 4.15. The zero angle of attack wing lift was under-predicted by approximately 13% compared to the OVERFLOW prediction, however the lift slope was matched within 3%. The mean absolute percentage error (MAPE) was 8%. The small lift deficit is at least partially the result of tip losses at the root of the CHARM wing model, where there is no splitter plate

Table 4.9: Comparison of predicted lift coefficients between OVERFLOW and OVERFLOW-CHARM with percent error calculated relative to the OVERFLOW value.

α (°)	**OVERFLOW** C_L	**OVERFLOW-CHARM** C_L
0.0721	0.67049	0.58434 (-12.9%)
3.0958	0.91657	0.82990 (-9.5%)
5.1089	1.0803	0.97556 (-9.7%)
7.1167	1.2277	1.1483 (-6.5%)
11.133	1.4708	1.4896 (+1.3%)

geometry resolved. This could be remedied by including the splitter plate in the CHARM model, or by applying an image plane at the wing root to prevent tip losses.

The prediction of sectional pressure coefficients was accurate to the experimental and CFD data, especially out of the effect of the propeller wake. The impact of the rotor wake was captured particularly well on the lower surface of the wing, varying with an average RMS error of 0.23 compared to the OVERFLOW predictions. On the upper surface, within the influence of the propeller wake, the trend of an increase in the suction peak and an overall decrease in the pressure coefficient was captured. However, the magnitude of the suction peak was under-predicted, and between x/c = 0.4 and 0.8 at BL 63 (closest to the propeller), pressure coefficient was generally over-predicted. Strong correlation was observed between the pressure coefficient predictions of OVERFLOW-CHARM and OVERFLOW, indicating that the detailed interactional aerodynamics of the wing and propeller can be well-captured at significantly reduced computational cost by employing hybrid methodologies.

At zero angle of attack (Figure 4.11), at BL 57, the only major difference between OVERFLOW and OVERFLOW-CHARM is the capture of the pressure fluctuation caused by a small deviation in the wing geometry by OVERFLOW. At BL 60.75, which is approximately aligned with the propeller tip vortex, the average suction peak is slightly underpredicted by OVERFLOW-CHARM, and the upper surface pressure is slightly underpredicted downstream of the mid-chord. At BL 63, the suction peak is again underpredicted by OVERFLOW-CHARM, with general differences in the prediction of the pressure deviation on the upper surface as a result of the interactions between the propeller wake, wing, and nacelle. On the lower surface, OVERFLOW-CHARM misses the pressure minimum at the mid chord.

At moderate angles of attack (Figure 4.12-Figure 4.13), similar observations to those at zero angle of attack are present for BL 57 and BL 60.75. However, at BL 63, both OVERFLOW and OVERFLOW-CHARM underpredict the pressure on the upper surface. At the highest angle of attack (Figure 4.15), more significant differences start to emerge between OVERFLOW and OVERFLOW-CHARM, even at BL 57. At both BL 57 and BL 60.75, OVERFLOW-CHARM is unable to predict the trailing edge separation on the upper surface due to the potential formulation of CHARM. However, at BL 63, both OVERFLOW and OVERFLOW-CHARM predict that the propeller wake prevents trailing edge separation from occurring and better agreement is observed between the two solvers.

4.4.7 Computational Cost Savings

On average, OVERFLOW required 10-11 blade passages before the wing lift and propeller loads converged to a periodic solution, meeting the convergence criterion of Equation 4.1. OVERFLOW-CHARM required an average of 8 blade passages to reach the same convergence. Additionally, the disk approach to off-body grid reduction provided a 65% decrease in the number of points compared to the baseline OVERFLOW grid. The combination

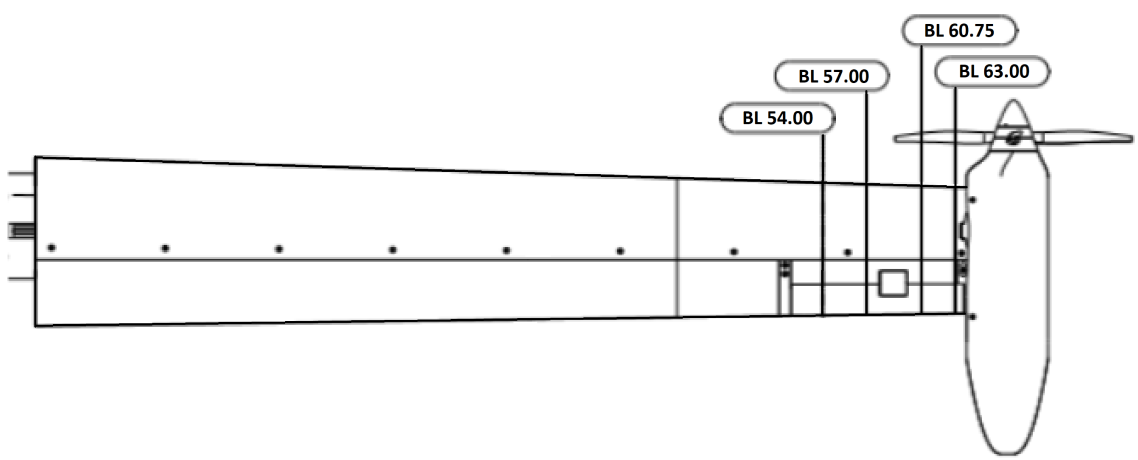

Figure 4.10: Experimental wing pressure tap locations

of grid reduction and convergence speed benefits of OVERFLOW-CHARM resulted in computational cost savings of 70% when simulations were parallelized so that the number of points per processor was kept the same between OVERFLOW and OVERFLOW-CHARM. The OVERFLOW simulations required approximately 5000 Central Processing Unit (CPU)-hours to evaluate, whereas the OVERFLOW-CHARM simulations required approximately 1500 CPU-hours.

4.5 Concluding Remarks

This chapter demonstrates the ability of a sufficiently accurate and flexible hybrid methodology to be applied to analysis of an integrated propulsion system configuration at reduced computational cost when compared to conventional CFD methods. The following is a summary of the conclusions can be made from the results presented here:

- The Spalart-Allmaras turbulence model with no rotational correction or Delayed Detached Eddy Simulation formulation is sufficient to capture integrated propeller performance with either conventional CFD methods or hybrid methods.
- The off-body grids can be reduced to a disk encompassing the propeller blades with OVERFLOW-CHARM.
- OVERFLOW-CHARM can predict nonlinear aerodynamic effects of the wing on

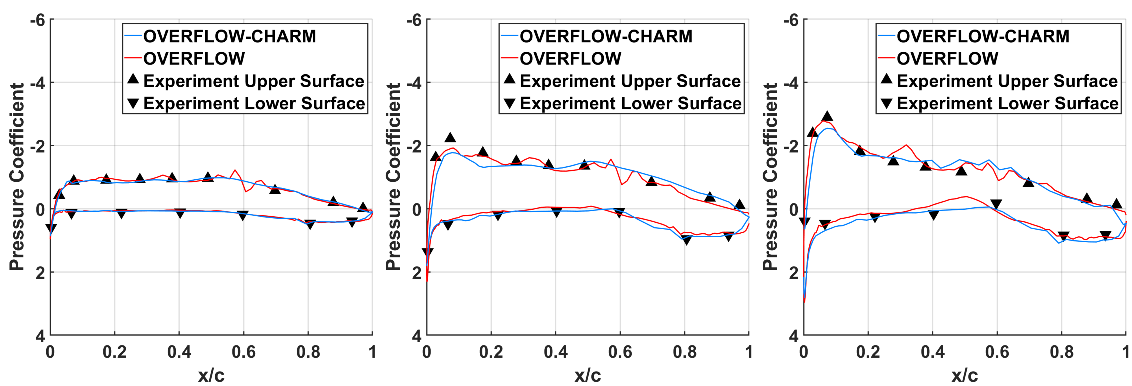

(a) **BL 57** (b) **BL 60.75** (c) **BL 63**

Figure 4.11: Pressure coefficient predicted using CHARM panels in the OVERFLOW-CHARM simulation at $\alpha = 0.07°$

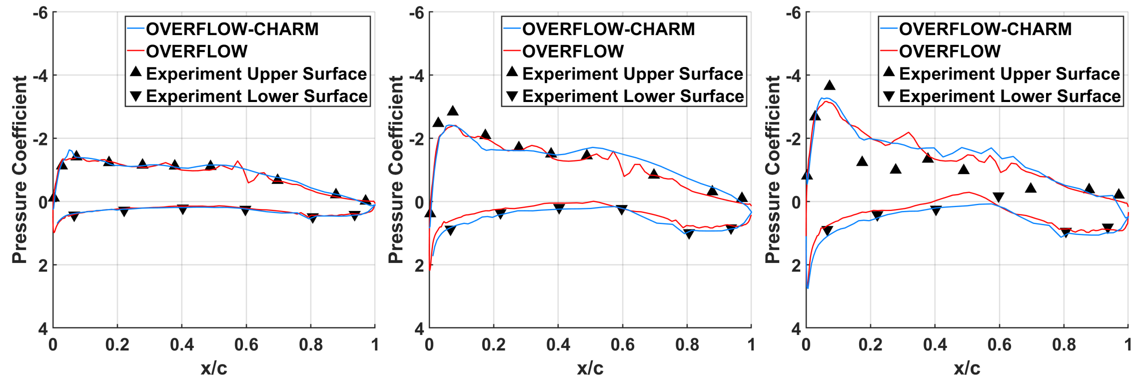

(a) **BL 57** (b) **BL 60.75** (c) **BL 63**

Figure 4.12: Pressure coefficient predicted using CHARM panels in the OVERFLOW-CHARM simulation at $\alpha = 3.10°$

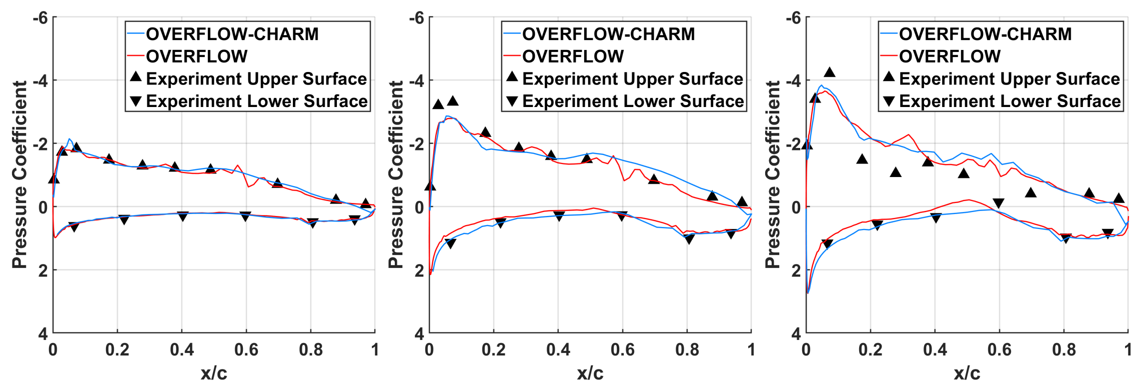

(a) **BL 57** (b) **BL 60.75** (c) **BL 63**

Figure 4.13: Pressure coefficient predicted using CHARM panels in the OVERFLOW-CHARM simulation at $\alpha = 5.11°$

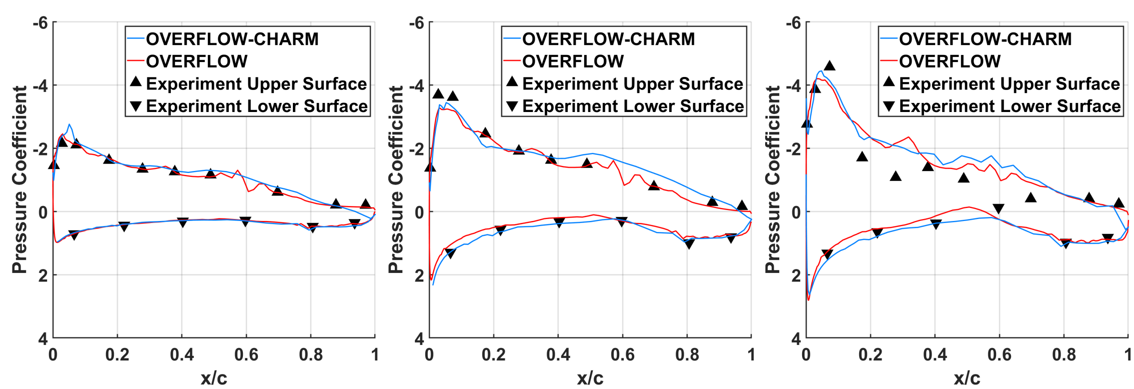

(a) **BL 57** (b) **BL 60.75** (c) **BL 63**

Figure 4.14: Pressure coefficient predicted using CHARM panels in the OVERFLOW-CHARM simulation at $\alpha = 7.12°$

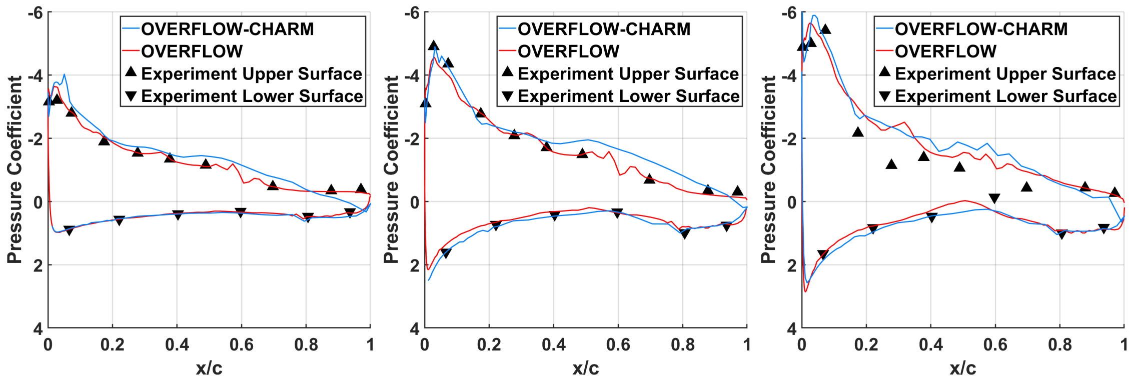

(a) **BL 57** (b) **BL 60.75** (c) **BL 63**

Figure 4.15: Pressure coefficient predicted using CHARM panels in the OVERFLOW-CHARM simulation at $\alpha = 11.13°$

integrated propeller performance.

- OVERFLOW-CHARM can be applied to inspect detailed interactional aerodynamic effects of the integrated propeller on the wing pressure distribution.
- OVERFLOW-CHARM can provide cost savings in excess of 70% when applied to integrated propulsion system analysis.

CHAPTER 5
ROTORS IN HOVER IN GROUND EFFECT

5.1 Introduction

A computational tool for Dynamic Interface (DI) analysis must be capable of capturing the influence of rotor-wake/ship-deck interactions on rotor performance and flight dynamics during shipboard landing. The flow physics in this scenario are comparable to those during hover in ground effect. While reduced-order models exist to estimate ground effect's impact on rotor hover performance, they do not resolve the relevant physics, which is required if they are to be extended to DI analysis so that the motion of the ship, the irregular ship geometry, partial ground effect, and the presence of the ship airwake are included. To address this, OVERFLOW-CHARM capability of modeling the ground effect is validated with experimental data. Special focus is placed on the code's ability to capture flow physics for application to DI analysis. While the most detailed experimental data are only available for very small scale rotors, findings were also compared to a larger scale rotor experiment to verify that they are valid at full scale simulations.

5.2 Micro-Scale Rotor in Ground Effect

Prediction capabilities of ground effect using OVERFLOW-CHARM were first validated with the experiment performed by Lee et al. [145]. Simulations matching the experimental conditions generated predictions of the hover performance and flow field of a micro-scale rotor in and out of ground effect. The rectangular rotor blades were untwisted and untapered with a radius of 91.6 millimeters and a chord of 21 millimeters. The root cutout was estimated from images in Lee et al. to be approximately 16 millimeters (0.175 R). The blade airfoil was a circular section with 3.3% camber and 3.7% thickness. The collective was fixed at 12 degrees. The rotation speed of the rotor was 50 Hz, corresponding to a tip Mach number of 0.08 and a tip Reynolds number of 36,000 based on the blade chord. The experiment was performed in a flow-conditioned test cell with honeycomb walls.

Parametric studies of low-Mach preconditioning strength, time step, grid density, and domain configuration were performed with OVERFLOW-CHARM at the Out of Ground Effect (OGE) condition, and then a sweep of heights above the ground plane was performed employing the optimal numerical parameters. To establish a computational baseline, OVERFLOW simulations were performed in and out of ground effect employing best practices for detailed hover performance analysis [146, 147].

5.2.1 Computational Meshes

While exact digital geometry of the experimental rotor was not available, details of the rotor blades described in Lee et al. [145] and in Kalra [148] informed the generation of the geometry for discretization. To best preserve the sharpness at the trailing edge, the blades were resolved with C-H topology grids. To ensure high-quality cells in the mesh, the blade leading edges were rounded with a radius of 0.016 millimeters (0.15% of the chord).

The baseline primary blade grid included 101 points in the radial direction spaced with a hyperbolic tangent distribution with root and tip spacings equal to 0.1% of the rotor radius. There were 81 points in the wall normal direction spaced with a geometric distribution and a growth rate of 1.05 in the boundary layer (22 points) up to a maximum growth rate of 1.1. In the chordwise direction, the airfoil shape was resolved with 386 points having leading edge and trailing edge spacing of 0.1% of the blade chord and all points followed a hyperbolic tangent distribution. This near-body grid resolved a region 1.2 chord lengths around the blade.

The baseline meshes were based on best practices identified in prior analyses with VOERFLOW-CHARM [128, 149]. Because the shape of the blade root and tip was not described in Lee et al. [145], a circular revolution of the airfoil about the camber line com-

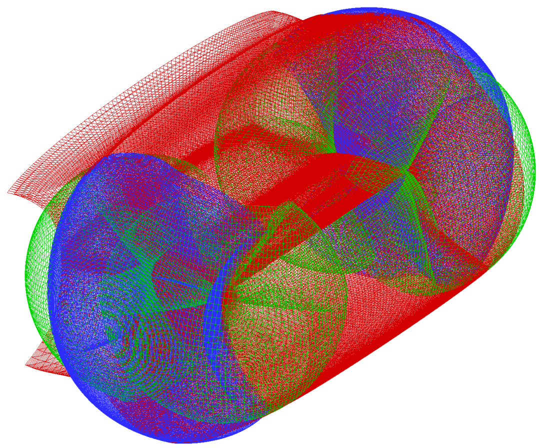

(a) Volume Grids

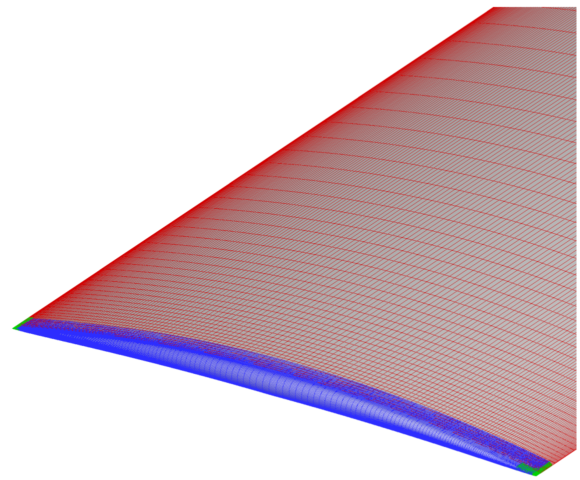

(b) Surface Grids

Figure 5.1: Baseline blade mesh system composed of seven grids. The main blade grid is depicted in red, root and tip grids in blue, and blade corner grids in green.

prised the computational root and tip geometry. To avoid singularities in the grid topology, three sub-grids resolved each blade root and tip. The surface grids at the leading and trailing edges had dimensions of 49×78 points and 51×74 points, respectively, and conformed to the distribution of points in the wall normal direction of the main blade sub-grid. Between these corner grids, a surface grid with dimensions of 196×108 points resolved the remainder of the root/tip geometry, with the main blade sub-grid wall-normal point distribution. The outer limits of each grid formed a continuous surface so that the CHARM boundary condition could be easily applied to these boundaries, as illustrated in Figure 5.1.

To determine whether point reduction of the near-body mesh was possible without impacting the solution, the number of grid points in the primary, root, and tip blade grids was approximately halved in each direction to determine the effect on the simulation fidelity. The simulations performed are described in Table 5.1. These simulations employed the Single-Gridded-Blade (SGB) OVERFLOW-CHARM domain configuration.

In the baseline OVERFLOW simulations, off-body Cartesian grids were generated at run-time. The off-body domain consisted of a refinement region and far-field region. The refinement region extended 1.5 rotor radii in the plane of the rotor and up to two rotor

Table 5.1: Table describing coarsening of main and root/tip grids for each case in the grid study. Dimensions correspond to chord x radial x normal point counts.

Coarsening Direction	Primary Dimensions	Root/Tip Dimensions	Total Size
None (Baseline)	546×101×81	196×108×81	9.13 M
Chord (½)	274×101×81	99×108×81	5.20 M
Radial (½)	546×51×81	196×108×81	6.92 M
Normal ($\approx$ ⅔)	546×101×51	196×108×51	6.20 M
All	274×51×51	99×108×51	3.03 M

radii below the rotor. The mesh cells were constrained to side lengths no greater than five percent of the chord. The far-field region extended up to 17 rotor radii out from the rotor and was resolved with cells that doubled in size every four cells as the distance from the rotor increases (see Figure 5.2). These off-body settings are consistent with best practices for Automatic Mesh Refinement (AMR) established in the literature [147, 150])

5.2.2 Numerical Options

Time-advancement employed dual-time stepping with thirty second-order subiterations, a local time step factor of 0.1, and a minimum Courant–Friedrichs–Lewy (CFL) number of five. Subiterations were stopped after the L2 norm of the residual dropped by two orders of magnitude. In prior studies, the time step in OVERFLOW-CHARM simulations has corresponded to 0.25 degrees of azimuthal rotation of the rotor in keeping with the convention for detailed rotorcraft unsteady Reynolds-Averaged Navier-Stokes (uRANS) simulations [128, 138, 149]. To determine whether such a small time step was necessary, diagnostic simulations were evaluated at 0.25 and 0.5 degrees per time step. The right-hand-side terms were discretized using fourth-order Roe upwind spatial differencing with 4/2 dissipation where the fourth- and second-order dissipation constants were 0.04 and 10.0, respectively. The left-hand-side terms were discretized using a diagonalized Beam-Warming scalar pentadiagonal scheme with fourth-order dissipation. The one-equation thin-layer Spalart-Allmaras turbulence model was used, as Wilbur et al. [128] determined that this provided the best compromise of computational cost to fidelity when flow separation was not anticipated.

This assumption was validated by testing Spalart-Allmaras (SA)-Delayed Detached Eddy Simulation (DDES), k-ω-Shear-Stress Transport (SST), and k-ω-SST DDES turbulence models, which showed minimal improvement in predicted results so that the additional computational cost required to apply these models was not warranted.

5.2.3 Low Mach Preconditioning

Because of the low tip Mach number of 0.08, the solution of the compressible Navier-Stokes equations can result in a numerical scheme that is overly stiff and exhibits slow solution convergence. OVERFLOW employs Weiss-Smith Low Mach Preconditioning (LMP) [151], which requires a user-specified β_{min} parameter that determines the strength of the preconditioning scheme. The default value of $\beta_{min} = 3M_\infty^2$ is recommended, but to verify this recommendation, a single static rotor blade at freestream conditions representative of the tip conditions in the experiment were evaluated at $\beta_{min} = 1.5M_\infty^2, 8M_\infty^2, 3M_\infty^2$, and with no preconditioning. The default value of $\beta_{min} = 3M_\infty^2$ provided the optimal convergence of the blade sectional lift and drag. To ensure that LMP did not impact the accuracy of the simulation, the pressure coefficient distribution at the mid-span of the blade and integrated forces were compared with and without LMP. This comparison verified that both the RMS deviation of the pressure and the total lift and drag forces on the blade differed by less than 1%, while more than doubling the rate of solution convergence. These findings are consistent with previously published studies of the β_{min} parameter for OVERFLOW applications [152–154]. When applied to the Cartesian off-body grids generated by OVERFLOW at runtime, the near-body value of β_{min} resulted in odd-even decoupling instability, which was resolved by increasing β_{min} to 0.1 for the off-body grids.

5.2.4 Baseline OVERFLOW Simulation Setup

The OGE simulation utilized OVERFLOW's vorticity-based automatic mesh refinement capabilities in the refinement region. The In Ground Effect (IGE) simulations were similar, but with an inviscid boundary to mimic the ground plane at the appropriate height below the rotor and an extended refinement region over the ground plane to capture the spreading of the rotor wake. Viscous boundary conditions for run-time-generated off-body grids are not supported within OVERFLOW. Due to the expense of the full uRANS simulations, one OGE (no ground plane present) and two IGE cases at heights of one and two rotor radii was performed to establish the variation of rotor performance due to ground effect. The full range of experimental heights was performed with OVERFLOW-CHARM.

Some convergence issues were observed in the rotating simulations that did not occur in the static LMP parametric study. Large oscillations in the blade forces appeared over multiple revolutions that did not dissipate as the simulation progressed. The source of these oscillations was determined to be the abrupt start of the blade motion at the beginning of the simulation, which creates a large initial transient. To mitigate this, the OVERFLOW simulations were initialized by linearly ramping the rotor speed from zero to the desired speed over one rotor revolution. After ramping up the rotor speed, simulations were performed for 4.5 revolutions without AMR to initialize the rotor wake, then for 4.5 revolutions with AMR to converge to the final solution.

The AMR procedure evaluated the sensor function $\|\nabla \times \vec{u}\| = 0.025\frac{s^{-1}}{a_\infty l_g}$ to decide whether a grid block was to be refined or coarsened. If a grid block contains a nondimensional vorticity magnitude value greater than the threshold value it is flagged for refinement, otherwise it is flagged for coarsening. The solution from the previous step is then interpolated onto the refined grid. This procedure is applied only on the Cartesian background grids in the refinement region, and the AMR algorithm was limited to two levels of refinement where the smallest cells have side lengths of 1.25% of the blade chord. The resulting mesh after an AMR simulation can be observed in Figure 5.2. The red box encloses the region in which the AMR sensor function is evaluated and mesh refinement is performed. The blue box delineates a refinement region which is manually specified to ensure that the spreading of the rotor wake is resolved before AMR begins. The evolution of each grid

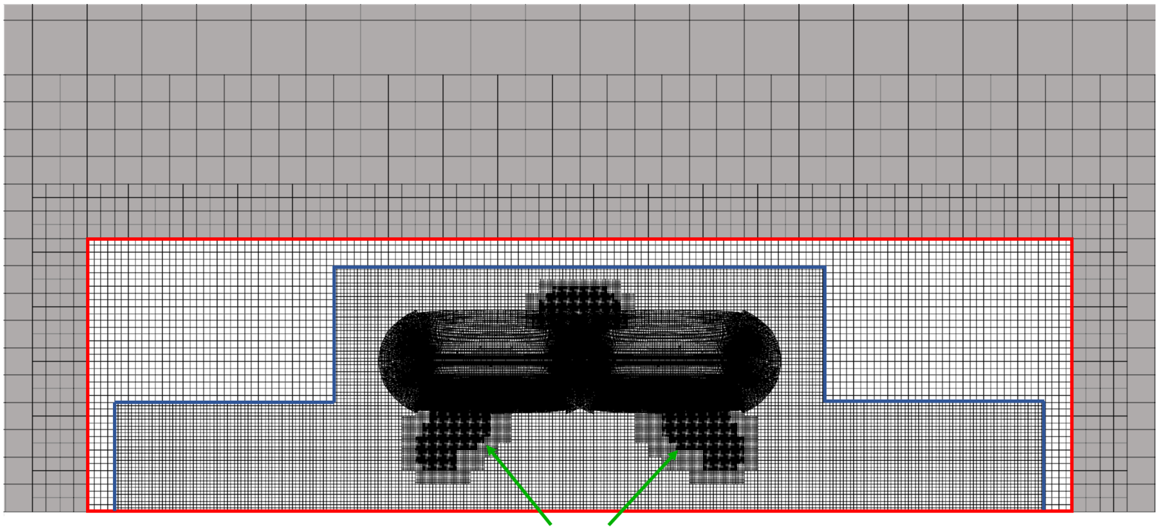

Figure 5.2: Slice of a grid produced by the AMR procedure.

at the three ground heights as the simulations progressed is given in Figure 5.3. The flat trends observed after 300-400 AMR iterations indicates that additional revolutions would not further resolve vorticity in the flow field.

5.2.5 OVERFLOW-CHARM Simulation Setup

OVERFLOW-CHARM domain configurations of five types were evaluated: a static contiguous simulation, a rotating contiguous simulation, a noncontiguous simulation, and an SGB simulation. The domain configurations are described visually in Figure 5.4. Each OVERFLOW-CHARM case was evaluated over six revolutions, at which point the average integrated loads had converged according to the criteria:

$$\left| \frac{\overline{C_T\left(\psi - 360 : \psi\right)}}{\overline{C_T\left(\psi - 720 : \psi - 360\right)}} - 1 \right| < 0.025, \tag{5.1}$$

indicating that the mean thrust coefficient has changed by less than 2.5% in the last computed revolution. This definition is necessary due to the chaotic nature of long-age CHARM vortex elements, which are usually convected away from the rotor in forward flight conditions. Boundary velocities were interpolated with the Force-Predictive Interpolation (FPI)

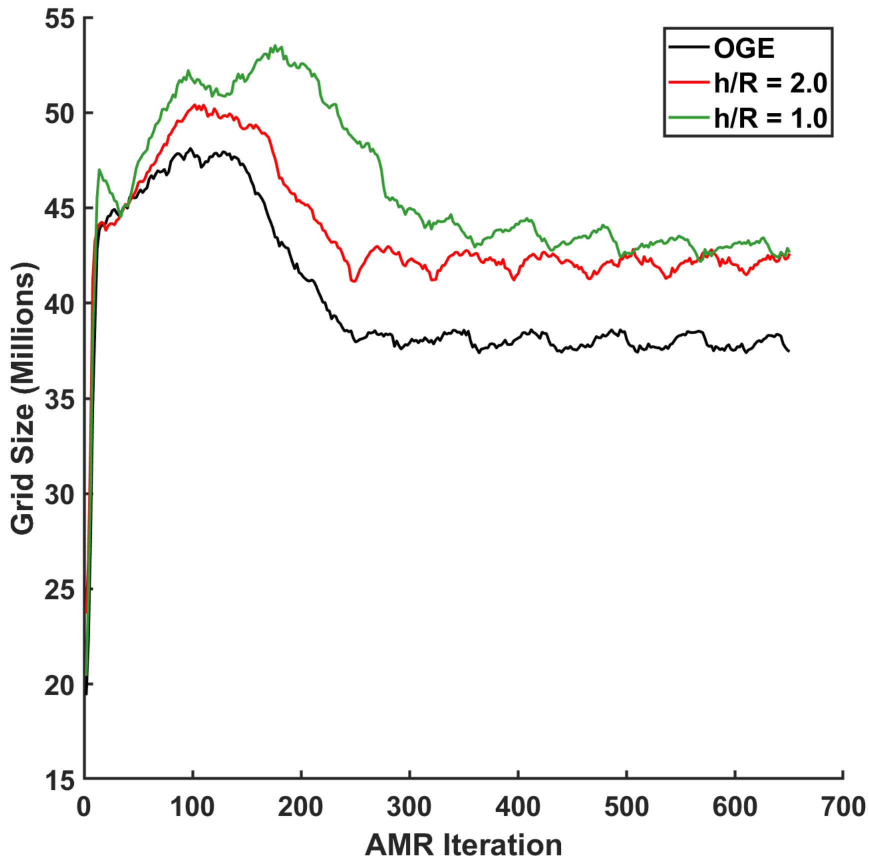

Figure 5.3: Evolution of the AMR grid size for the three heights studied.

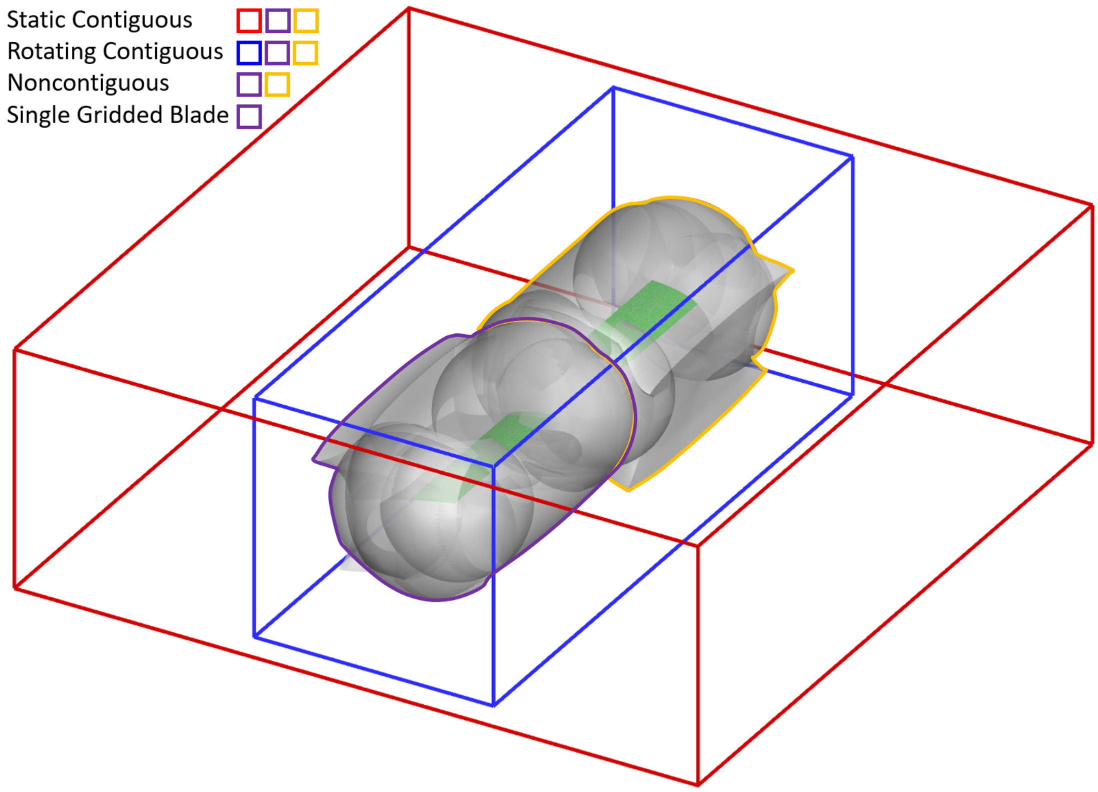

Figure 5.4: Visual description of OVERFLOW-CHARM domain configurations. Box colors in the legend correspond to components outlined in the diagram which constitute each case.

method to mitigate oscillations resulting from aperiodicity of the strong root vortex in the CHARM solution.

The ground plane in the CHARM simulation is modelled as an image plane, across which vortex elements are reflected. The CHARM wake model is updated 72 times per revolution, i.e. every five degrees. Root and tip vortex elements older than six revolutions are assumed to be far enough away that they do not impact the flow within the OVERFLOW domain and are removed from the simulation. Full-span vortex elements are retained for three revolutions. The settings for CHARM update frequency and number of vortex elements retained were selected to provide maximum fidelity while maintaining a stable wake solution, since long-wake-age elements become increasingly unstable. Blade loads from the initialization file are applied during the first blade passage of the simulation so that the initial transients in the uRANS solution do not effect the CHARM solution. During the second blade passage, a smoothly interpolated transition between the initialized loads and the OVERFLOW-predicted loads is performed, after which the blade loads come solely from the uRANS flow prediction.

5.3 Micro-Scale Results

5.3.1 Time Step Study

Comparing simulations at the larger time step (0.5 degrees) with those at the smaller time step (0.25 degrees), the integrated performance coefficients required more rotor revolutions to converge; however, convergence was achieved in fewer iterations and fewer subiterations. Approximately ten fewer subiterations were required to achieve consistent two order s of mangnitude reduction in the subiteration L2 norm residuals with the larger time step. These factors resulted in wall-time savings of approximately 38% with the larger time step. The final converged value for the integrated quantities differed by less than 0.3%, and differences in the blade surface aerodynamic stresses were negligible between the two time step values. Thus, a time step of 0.5 degrees per step was applied in the final simulations.

5.3.2 Grid Density Study

As described in Table 5.2, the predicted total thrust and power coefficients have similar values for the baseline and all coarsened grids. However, significant differences were observed in the mid-span pressure coefficient prediction for all but the grid coarsened in the wall-normal direction. From inspection of the surface pressure predictions in Figure 5.5, the effect of coarsening in each direction can be determined. Reduction of the mesh size along the chord altered the stress predictions primarily at the leading edge of the blade. Radial coarsening generally redistributed the stresses along the span of the blade, with shear stress differences observed at the blade tip. Coarsening in all directions produced predictions which were, predictably, a combination of the differences seen in each individual case. As a result of this study, the normally-coarsened grid is chosen for further use in this

Table 5.2: Table describing OGE hover results with coarsening of main and root/tip grids in various directions. Percent error differences in parentheses relate to the OVERFLOW baseline computation. The chosen grid is highlighted in green.

Coarsening Direction	**Final C_T (% Err)**	**Final C_P (% Err)**	**C_p Difference**		**C_f Difference**	
			Max	**RMS**	**Max**	**RMS**
N/A (Baseline)	0.093928	0.0145	-	-	-	-
Chord	0.0922 (-1.8%)	0.0143 (-1.4%)	0.809	0.0327	8.0e-5	2.6e-6
Radial	0.0931 (-0.9%)	0.0144 (-0.8%)	0.252	0.0078	3.7e-3	3.5e-5
Normal	0.0932 (-0.8%)	0.0145 (-0.2%)	0.122	0.0098	1.4e-5	8.6e-7
All	0.0922 (-1.8%)	0.0144 (-0.8%)	0.782	0.0327	7.8e-5	2.9e-6

Table 5.3: Comparison of integrated quantities predicted when employing various grid reduction strategies for the micro-scale rotor in hover out of ground effect.

	Thrust Coefficient	**Power Coefficient**	**Grid Size**
Baseline OVERFLOW	0.094	0.0144	37.5M
Static Contiguous	0.097	0.0146	17.1M
Rotating Contiguous	0.086	0.0138	15.9M
Noncontiguous	0.089	0.0141	15.6M
Single-Gridded-Blade	0.09	0.0142	8.2M

work, reducing the number of points in the blade grid system by approximately one third without significantly impacting the simulation accuracy.

5.3.3 Domain Configuration Study

Table 5.3 provides a comparison of integrated quantities predicted when evaluating the various grid reduction strategies to this case. The noncontiguous SGB simulation was able to predict the rotor performance with the with the same level of accuracy (within 4% of OVERFLOW) and rate of convergence (6 revolutions to meet the convergence criteria) as the other strategies at half the cost, so this was the configuration chosen for use in the study of ground effect. Results obtained with this setup are shown in Figure 5.7, demonstrating how it is effective for cost-effective prediction of the rotor flow physics of this case. Because the CHARM solution still contains wake filaments shed from both blades, the SGB method does not affect OVERFLOW-CHARM's modeling of wake-ground interactions.

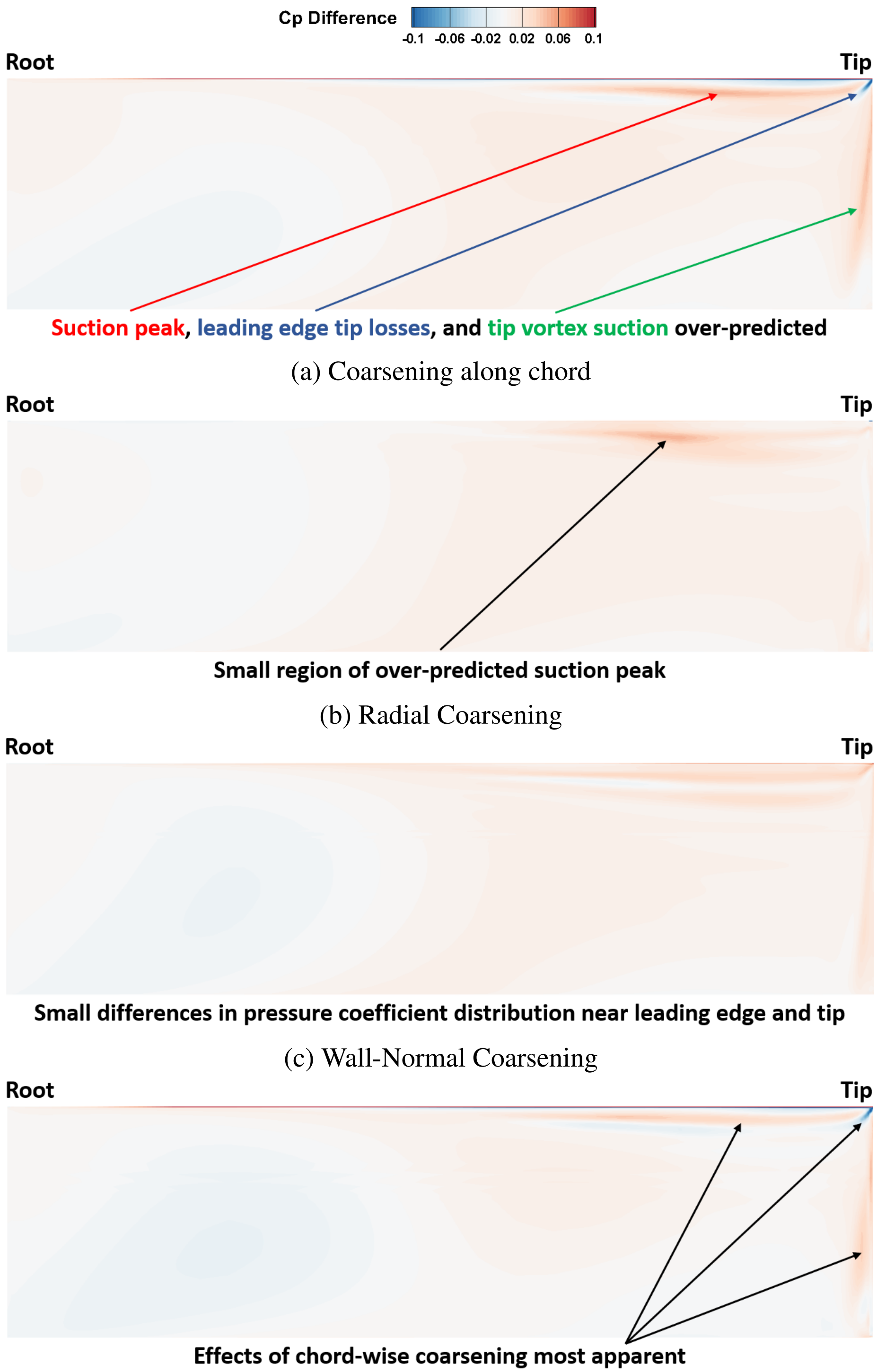

(a) Coarsening along chord

(b) Radial Coarsening

(c) Wall-Normal Coarsening

(d) Coarsening in All Directions

Figure 5.5: Difference in rotor blade upper surface pressure coefficient distribution with coarsening in the indicated direction compared to the baseline grid

5.3.4 Integrated Quantities and Computational Cost

Figure 5.6 compares the variation of thrust coefficient, power coefficient, and figure of merit with rotor height above the ground between experiment [145], OVERTURNS [148], OVERFLOW, and OVERFLOW-CHARM. The OVERTURNS simulation in Kalra's dissertation provides an external reference for conventional uRANS methods' ability to make predictions for this particular case. The variation of thrust coefficient is predicted within 5% of the experimental data by OVERFLOW and OVERFLOW-CHARM while power coefficient is underpredicted by approximately 10%. However, results are consistent within 0.5% between between OVERFLOW and OVERFLOW-CHARM, demonstrating the efficacy of the OVERFLOW-CHARM methodology. Figure of merit predictions differ by less than 4 counts between OVERFLOW and OVERFLOW-CHARM, which is an improvement over previous hybrid predictions [149]. The underprediction of power coefficient by both OVERFLOW and OVERFLOW-CHARM may be due to low-Reynolds number effects based on the turbulence models available in OVERFLOW. The numerical studies discussed earlier rule out low-Mach preconditioning, grid density, or time step as the cause. The presence of the hub in the experiment would also have contributed some small additional drag which is not modeled in the computational results. Finally, root and tip geometry differences between the experiment and computations may also have contributed to the underprediction of power coefficient, as exact geometries were not available.

OVERFLOW-CHARM predicts the rotor performance coefficients within three percent of full uRANS at approximately 80% savings in computational cost (time and memory). The OVERFLOW simulations required approximately 10,000 CPU-hours, while the OVERFLOW-CHARM simulations required only 2,000 CPU-hours. The computational cost savings were due to an approximately 72% reduction in the number of grid points (adjusted for the AMR procedure), and a reduction of the number of revolutions required for convergence by one third. All simulations were performed using 48 MPI processes on the US DOD High Performance Computing (HPC) machine "Gaffney" with

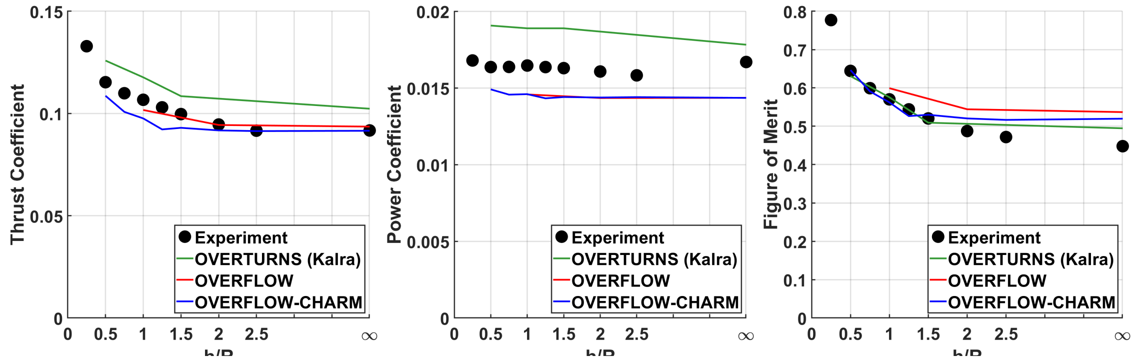

(a) Thrust Coefficient (b) Power Coefficient (c) Figure of Merit

Figure 5.6: Variation of rotor performance coefficients with ground plane height as predicted by OVERFLOW-CHARM, OVERFLOW, OVERTURNS, and experiment.

Intel®Xeon®Platinum 8168 CPUs at 2.7 GHz. Savings of this magnitude can increase the bandwidth of ground effect analysis workflows five-fold, making once intractable computations realizable.

5.3.5 Flow Field Analysis

Figure 5.7 displays the features of an OVERFLOW-CHARM simulation in ground effect. The global nature of the flow field is captured with CHARM vortex filaments and is accurately transferred into the OVERFLOW domain via the boundary condition coupling method. This is verified by the observation of isosurfaces of Q-criterion within the uRANS domain, where the tip vortex from the ungridded blade and older wake-age tip vortices are present within the uRANS solution. Non-dimensional Q-criterion is defined as

$$Q_c = \frac{1}{2}\left(\|\Omega\|^2 - \|S\|^2\right), \tag{5.2}$$

where Ω and S are the vorticity and rate of strain tensors of the non-dimensional velocity vector $\vec{u}/a_\infty$. This criterion serves to identify vorticity in the flow which is not associated with shear strain and thus identify vortices while masking shear-related vorticity in the boundary layer or shear layers.

The tip vortex trajectories in ground effect predicted by OVERFLOW and

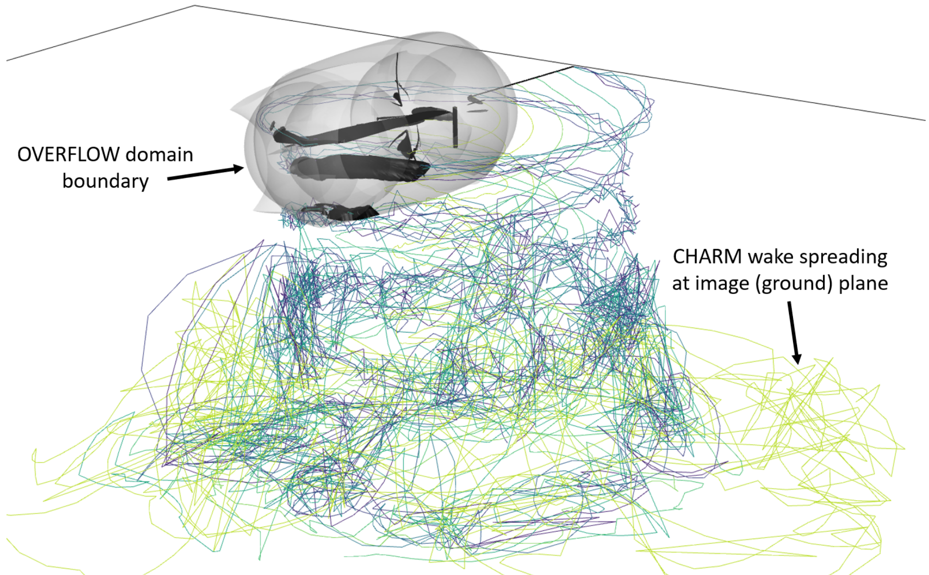

Figure 5.7: Wake geometry computed using the single-bladed OVERFLOW-CHARM simulation setup visualized using an isosurface of non-dimensional Q-criterion = 0.0001 within the uRANS domain and with CHARM vortex filaments in the CHARM domain. Filaments are colored according to their release order along the span of the blade.

OVERFLOW-CHARM are compared in Figure 5.8, which shows the OVERFLOW-computed tip vortex as a transparent isosurface of nondimensional Q-criterion = 0.00005 and the OVERFLOW-CHARM-computed tip vortex as the CHARM vortex filaments in black. For the OVERFLOW-CHARM wake, a higher concentration of CHARM filaments indicates a stronger vortex. In general, the tip vortex trajectory is predicted consistently between the two methods for wake ages less than approximately 0.75 revolutions, after which OVERFLOW predicts more downward convection of the vortex than does OVERFLOW-CHARM. At wake ages older than approximately 1.25 revolutions, the OVERFLOW-predicted wake has dissipated below the Q-criterion isosurface threshold and the CHARM wake becomes more unsteady and increasingly diffuse. It can be concluded from these observations and inspection of the integrated rotor loads that accurate prediction of the tip vortex is most important for wake ages less than one when analyzing rotor hover performance.

Lee et al. [145] provides smoke flow visualization for the experimental study of this ro-

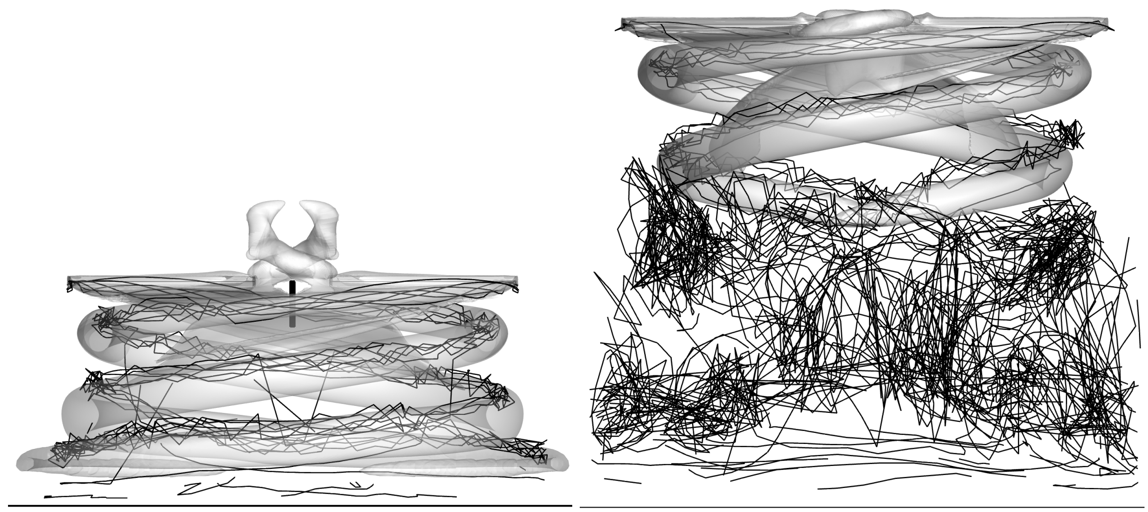

(a) h/R = 1.0 (b) h/R = 2.0

Figure 5.8: Comparison between tip vortex predicted by OVERFLOW (q-criterion = 0.00005 isosurface, grey) and OVERFLOW-CHARM (CHARM vortex filaments, black).

tor in ground effect. Comparisons between this type of flow visualization and instantaneous computational flow fields are necessarily qualitative in nature; however, data are presented so that similar features are highlighted by the two different visualization techniques. The trajectory of the high-speed rotor downwash is shown using velocity magnitude, and individual vorticies are highlighted using non-dimensional Q-criterion overlaid in black. For the OVERFLOW-CHARM visualizations, the OVERFLOW-predicted flow field is shown within the OVERFLOW domain. Outside the OVERFLOW domain, since CHARM does not solve for the traditional flow field quantities, an induced flow field is computed as a co-processing step during the simulation. While the slipstream boundary presented in the experimental data is approximate, a quantitative equivalent of this feature has been devised according to the following criterion:

$$\overline{\|\vec{u}\|} = 10\% \|\vec{u}_{tip}\| \tag{5.3}$$

where the mean of the velocity magnitude is taken over the last predicted revolution of the rotor. This criterion serves to separate high speed mean flow from low speed mean flow, which is a quantitative interpretation of the slipstream boundary presented in Lee et al. This method would require multiple revolutions of converged solution to eliminate bias from the average and produce a smooth slipstream boundary, but a smoothed result from a single revolution is sufficient for comparison to the uRANS and experimental data.

Qualitative aspects of both the OVERFLOW and OVERFLOW-CHARM flow fields agree with the experimental flow visualization, with clear similarities in the locations, trajectories, and relative spacings of the successive tip vortices. Out of ground effect (Fig. Figure 5.9), the OVERFLOW-CHARM slipstream boundary follows the experimental closely, particularly within the OVERFLOW domain. The most apparent differences between OVERFLOW and OVERFLOW-CHARM are the better resolution of the vortex sheet and higher dissipation of the tip vortices in the OVERFLOW solution. Far from the rotor, the influence of the starting vortex remains a factor in the deviation of the computational predictions compared to the experimental slipstream. At h/R = 2.0 (Fig. Figure 5.10), again, the slipstream boundaries of OVERFLOW and OVERFLOW-CHARM follow the same trajectory near the rotor, then begin to deviate as the unsteadiness in the CHARM wake begins to amplify at long wake ages. The spreading of the slipstream boundary is particularly affected by the difference in physical modeling at the wall, where OVERFLOW applies an inviscid boundary and CHARM employs an image plane method. Considering the low Reynolds number, it is also likely that the inviscid wall boundary condition in the OVERFLOW simulation is responsible for the deviations from the experimental slipstream boundary. The closest agreement between the slipstream boundaries of the three methods is observed at h/R = 1.0 (Fig. Figure 5.11). Here, the vortex sheet in the OVERFLOW solution is less apparent, and dissipation of the tip vortices is stronger than in the OVERFLOW-CHARM solution.

The influence of the starting vortex is visible in the OGE OVERFLOW results (Figure 5.9a), as the simulation had not progressed for sufficient time for it to dissipate or convect far away from the rotor. This is a known phenomenon in uRANS predictions of rotors in hover. In the IGE cases, the starting vortex is convected away by the wall jet produced by the ground effect and does not significantly influence the flow field in the region observed. This observation has since inspired an alternative application of the OVERFLOW-CHARM methodology as a way to initialize a conventional uRANS simulation. Setting the initial flow field to a CHARM-induced flow field instead of quiescent flow has the potential to reduce the strength of the starting vortex and thus reduce the amount of simulation time needed eliminate it from the flow field. Further study into this possibility is recommended.

5.4 Sub-Scale Simulations

To verify that the capabilities of OVERFLOW-CHARM extend to larger-scale rotors in ground effect, analysis was performed on a 1:4.71 scale S76 rotor matching the experiments of Balch and Lombardi [155, 156]. The primary objective of these experiments was to quantify differences in rotor blade tip geometry on hover performance. Four different blade tip geometries were evaluated in a collective sweep at various ground heights and tip Mach numbers. Test points employing the rectangular tip geometry at a tip Mach number of 0.6 have been compared to computational results in this research, namely run numbers 54, 57, and 58. The rotor blades were untapered, utilize the SC1095 and SC1094 R8 airfoils, and had a -10° equivalent linear twist, 3.5° coning angle, 56.224 inch radius, and 3.566 inch chord. Collective sweeps from 2 to 9 degrees in steps of approximately one degree were performed at ground heights of 0.75R, 1.2R, and 3R (corresponding to runs 54, 57, and 58, respectively), with the latter serving as the OGE test point.

Collective sweeps at various ground heights were performed by applying lessons learned from the micro-scale simulations and from simulations performed by Jacobson et al. [149]. These simulations seek to test the best practices established in the previous section at higher Reynolds numbers, verify improvements to OVERFLOW-CHARM since the study of Jacobson et al., and acquire more detailed hover performance results in and out of ground effect.

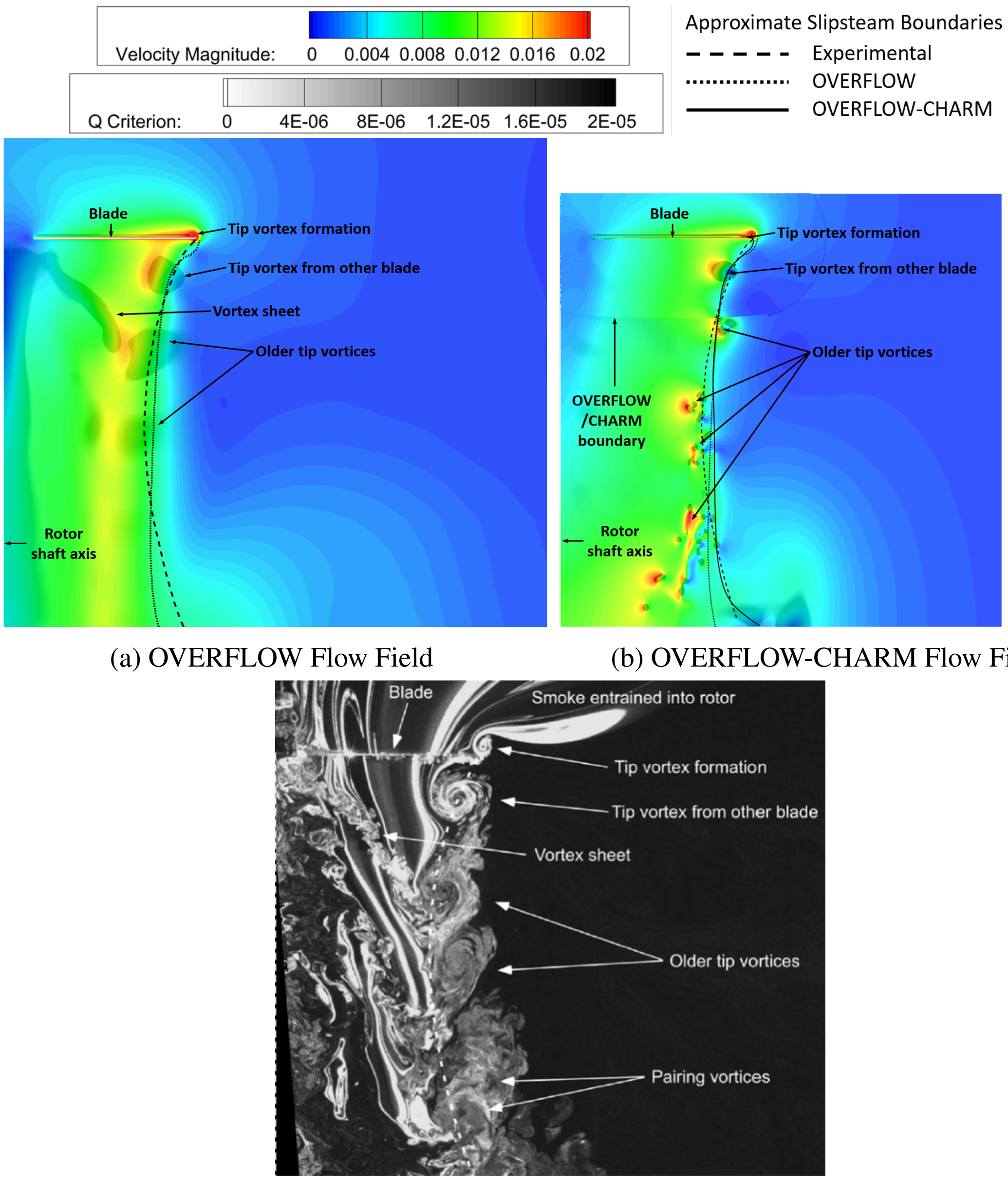

(a) OVERFLOW Flow Field

(b) OVERFLOW-CHARM Flow Field

(c) Experimental Flow Vis (Lee et al. [145])

Figure 5.9: Comparison between computational and experimental flow fields out of ground effect. Figures are to scale.

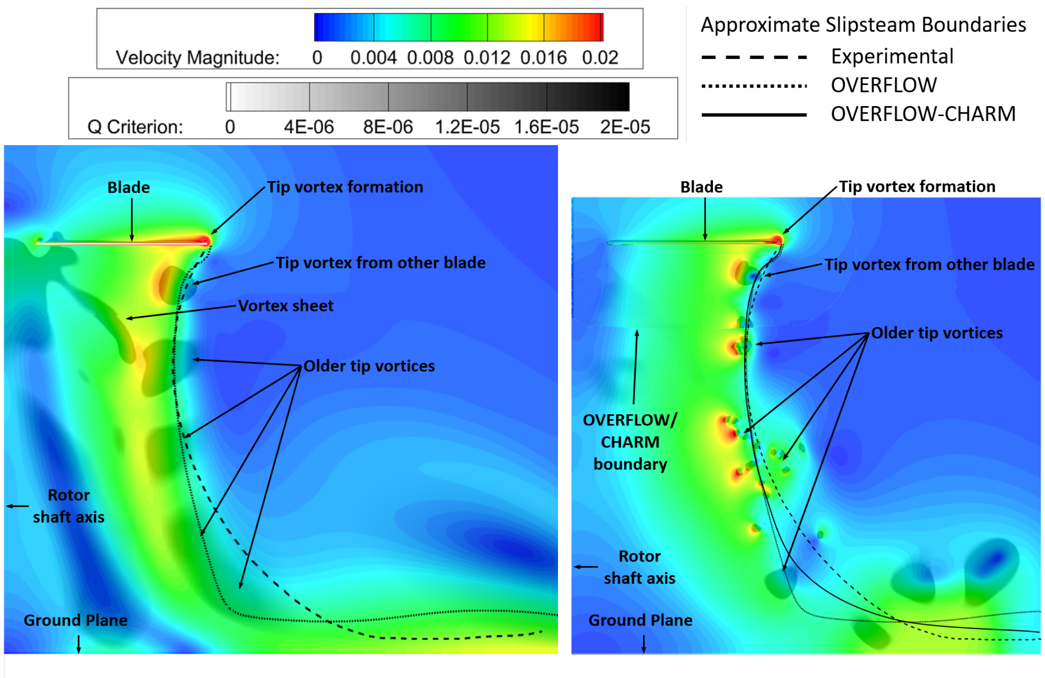

(a) OVERFLOW Flow Field (b) OVERFLOW-CHARM Flow Field

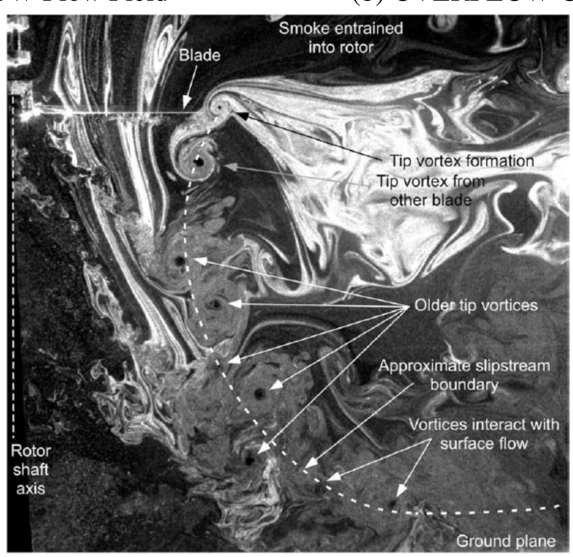

(c) Experimental Flow Vis (Lee et al. [145])

Figure 5.10: Comparison between computational and experimental flow fields at h/R = 2.0. Figures are to scale.

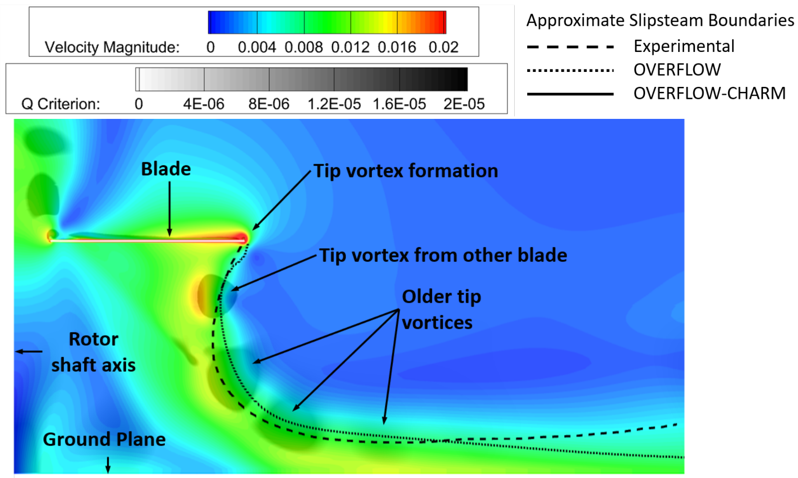

(a) OVERFLOW Flow Field

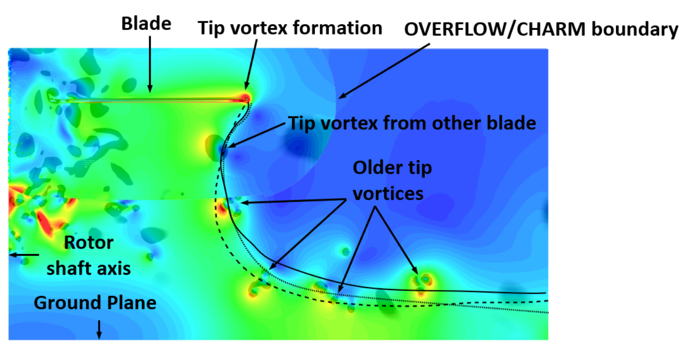

(b) OVERFLOW-CHARM Flow Field

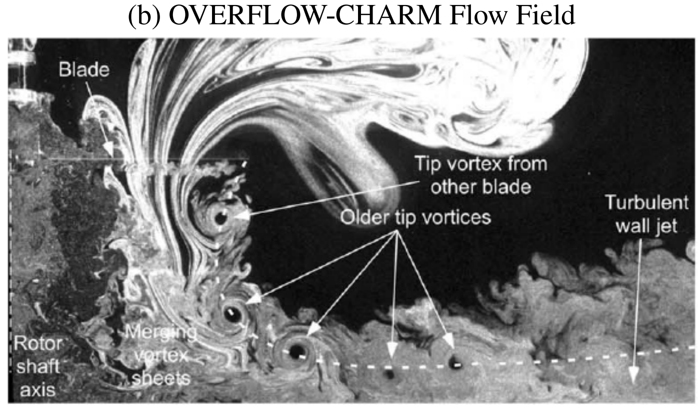

(c) Experimental Flow Vis (Lee et al. [145])

Figure 5.11: Comparison between computational and experimental flow fields at h/R = 1.0. Figures are to scale.

Table 5.4: Table of S76 grid properties colored according to Figure 5.12.

	Topology	Dimensions	Total Points
Main Blade	O-H	377x133x60	2.9M
Blade Root	H-H	49x145x60	0.4M
Blade Tip	H-H	49x145x60	0.4M
Hub	O-H	44x361x78	1.2M
Box	H-H	118x125x125	1.8M

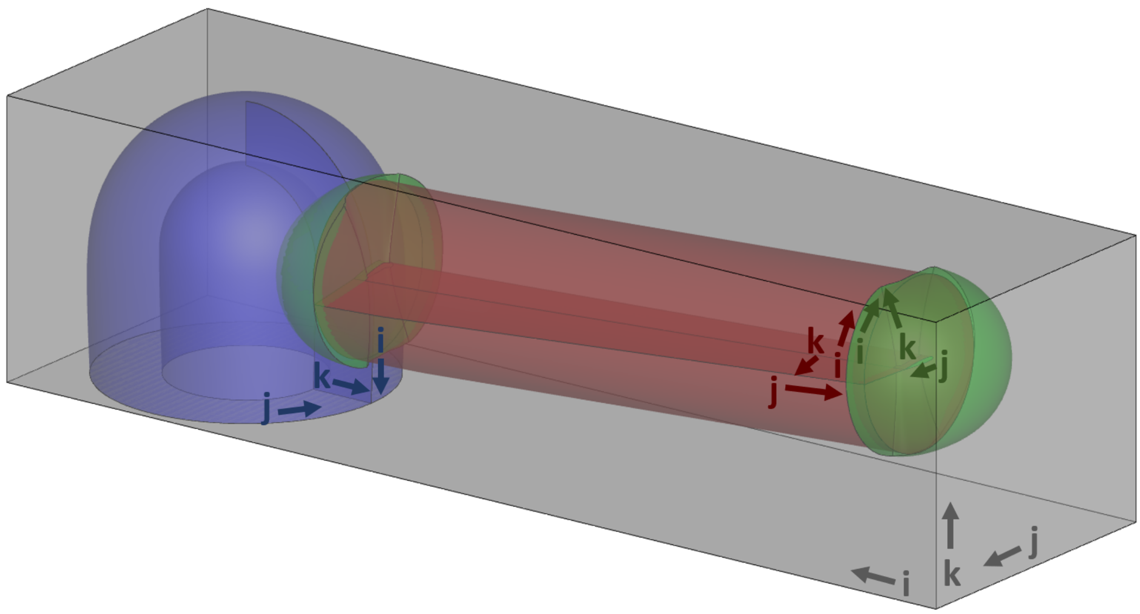

Figure 5.12: Diagram of S76 main blade (red), root/tip (green), hub (blue), and box (grey) grids.

The computational meshes for the S76 rotor blades were developed by Jacobson et al. and are described in reference [149]. A summary of the blade grids and hub grid is provided in Table 5.4 and Figure 5.12.

Numerical options are consistent with those of Jacobson et al. with some exceptions derived from the findings of the micro-scale study, described in Table 5.5. Time-advancement was performed with dual time stepping and a minimum CFL number of five. The physical time step was chosen so that the rotor advances 0.5 degrees per time step. The right-hand-side terms were discretized using fourth-order Roe upwind spatial differencing with 4/2 dissipation where the fourth- and second-order dissipation constants were 0.04 and 10.0, respectively. The left-hand-side terms were discretized using a diagonalized Beam-Warming

Table 5.5: Comparison of numerical options and OVERFLOW-CHARM code improvements between the present study and that of Jacobson et al. [149]

	Jacobson et al.	**Present Study**
Numerical Options		
Time Step	0.25 deg/step	0.5 deg/step
CFL Number	10	5
Spatial Scheme	Central	Roe
2nd-Order Diss. Constant	2	10
Revolutions	5	15
Subiterations	20	40
Code Improvements		
Domain Configuration	Noncontiguous	Noncontiguous SGB
Boundary Pressure	Isentropic	Unsteady Free-Wake Pressure
Boundary Interpolation	None	FPI
Boundary Characteristics	Unmodified	Modified

scalar pentadiagonal scheme with fourth-order dissipation. The one-equation thin-layer SA turbulence model was applied with a rotational correction. The CHARM wake model was updated every fifteen degrees with three revolutions of full-span vortex elements and six revolutions of root and tip vortex elements.

SGB OVERFLOW-CHARM simulations were computed in two stages, as illustrated in Figure 5.13. For the first stage, the CHARM solution was initialized from blade loads predicted by a two-revolution OVERFLOW simulation. The CHARM wake was initialized for two revolutions, and the OVERFLOW solution was initialized to CHARM-induced values. In both OVERFLOW-CHARM stages, blade loads were blended from the input loads beginning after one blade passage and proceeding over the second blade passage, after which loads are extracted entirely from the OVERFLOW solution. Stage one OVERFLOW-CHARM cases were computed for two revolutions with six subiterations and stage two cases for fifteen revolutions with forty subiterations. Boundary velocities were interpolated with the FPI method beginning after five revolutions.

The results of the sub-scale S76 OVERFLOW-CHARM simulations confirm that the findings of the micro-scale simulations translate well to larger rotors. Correlation of power coefficient vs. thrust coefficient is within 6% RMS error of the experimental data (see

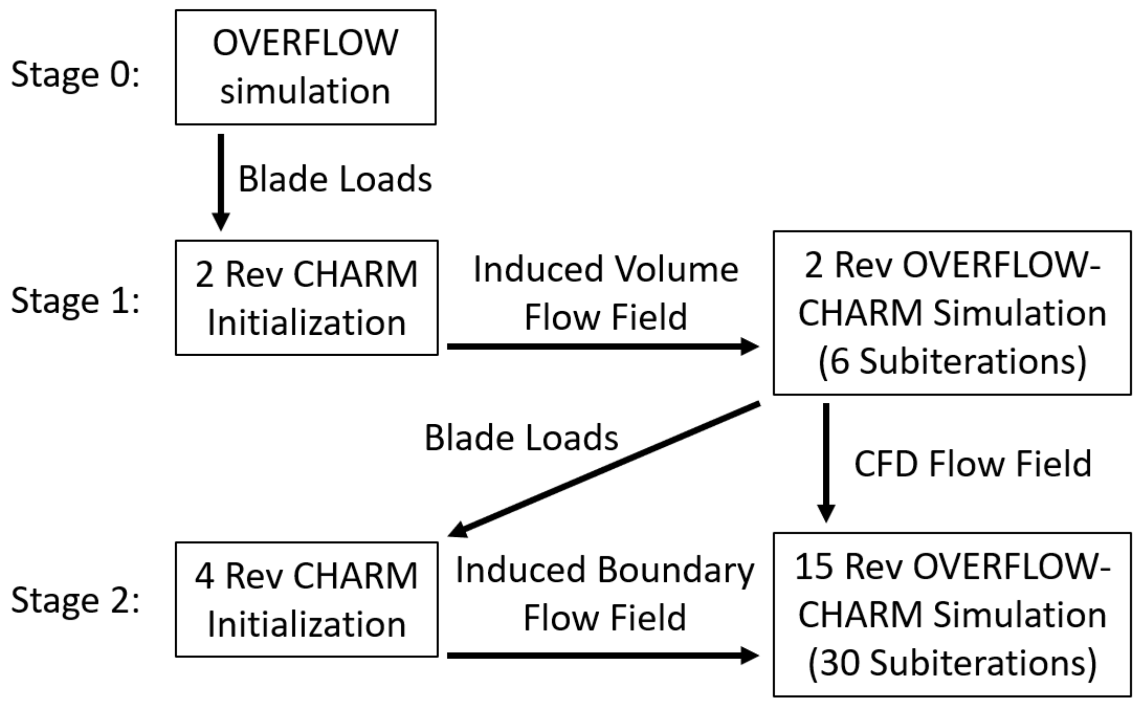

Figure 5.13: Flow chart describing OVERFLOW-CHARM simulations of the sub-scale S76 rotor.

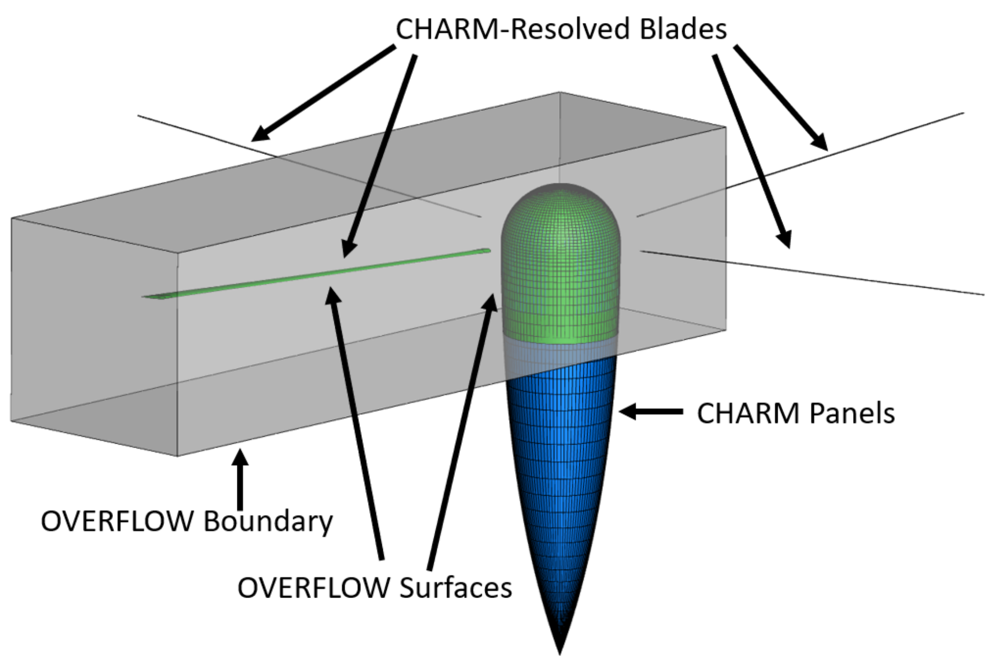

Figure 5.14: OVERFLOW-CHARM Simulation setup for S76 rotor in hover.

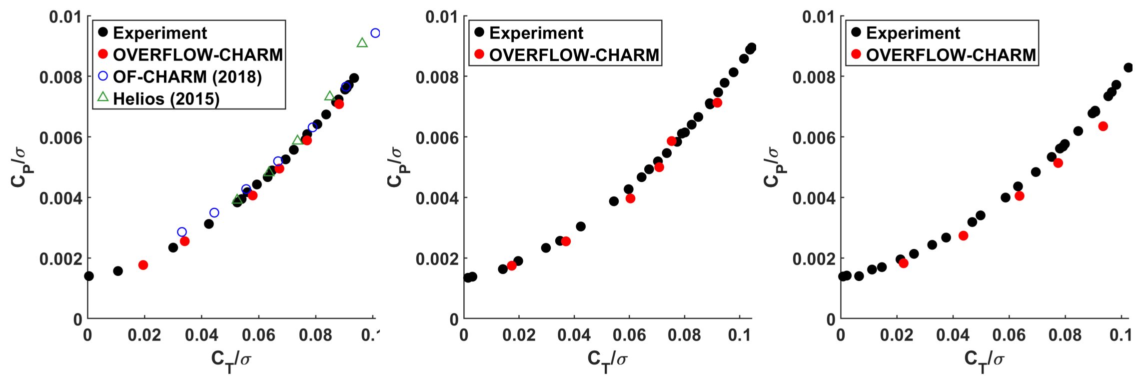

(a) h/R = ∞ (b) h/R = 1.2 (c) h/R = 0.75

Figure 5.15: Sub-scale S76 thrust vs. power plots at various ground heights as predicted by OVERFLOW-CHARM and experiment.

Figure 5.15). OGE performance plots for the Helios simulations of Jain [157] and the previous implementation OVERFLOW-CHARM utilized by Jacobson et al. [149] are also provided. The present results are as accurate as the uRANS simulations (RMS differences of 3.36% for OVERFLOW-CHARM and 3.38% for Helios with respect to the experiment) and are improved over the previous OVERFLOW-CHARM predictions (6.37%). Jacobson et al. presented cost savings of 94.3% compared to full uRANS with convergence reported after five revolutions, though no criterion is given. The present results were evaluated for more revolutions and used more subiterations, yet the grid reduction offered by the SGB methodology makes the overall computational cost comparable between the two studies (2610 core-hours for the present results and 2140 core-hours reported by Jacobson et al.).

5.5 Concluding Remarks

Results presented here demonstrate that OVERFLOW-CHARM can be accurately applied to rotor hover performance analysis at a range of scales where wake impingement on an external surface is present. Best practices are generally consistent with those established for conventional uRANS simulations, and advanced hybrid coupling approaches can be effectively employed for maximum cost savings, as much as 80%. The level of accuracy of OVERFLOW-CHARM predictions is the same as that of conventional uRANS predictions, generally within 10% for integrated loads, when compared to experimental data. These results establish confidence in OVERFLOW-CHARM's ability to be applied to shipboard landing scenarios where wake impingement on the ship deck is expected to impact rotor performance.

CHAPTER 6

LOW-SPEED OBJECT-INDUCED DOWNWASH RECIRCULATION

6.1 Introduction

The final step to develop OVERFLOW-CHARM as a viable tool for analysis of the Dynamic Interface (DI) is investigation of its capability to predict helicopter aerodynamics in the presence of an external airwake and ground obstacle. To achieve this, OVERFLOW-CHARM predictions of fuselage and rotor loads of an UH-60L helicopter in the presence of an Elevated Fixed Platform (EFP) are evaluated to those of a full-scale flight test performed at Naval Air Warfare Command Aircraft Division - Patuxent River (NAWCAD-PR). The UH-60L is aerodynamically identical to the UH-60A.

6.2 Experimental Configuration

Flight tests of the V-22, UH-72, OH-58C, and UH-60L were performed on the airfield at NAWCAD-PR with the objective of providing validation data for the Dynamic Interface Virtual Environment (DIVE) program, which is focused on improving DI simulation tools. The ground obstacle, called the EFP, was a $96 \times 100 \times 38$ foot construction of standard CONEX boxes. During these tests, velocity data was obtained from anemometers arranged along the wall of the EFP, as well as aircraft performance data and ambient wind conditions from a reference anemometer. Rotor speed was varied to achieve different values of thrust coefficient, since aircraft weight was allowed to vary with fuel burned. The data gathered during the flight test includes time-resolved velocity measurements near the EFP, aircraft position and attitude, pilot and Stability Augmentation System (SAS) control inputs, and engine power and fuel consumption. Testing was performed on days where winds were not expected to exceed ten knots. Before each test, a hover ladder, during which the aircraft

Table 6.1: Table of freestream values for the Low-Speed Object-Induced Downwash Recirculation (LOIDR) downwind and sideslip conditions. Standard sea level atmospheric conditions are assumed.

	Downwind	**Sideslip**
β (°)	0	75
M_∞	0.0075	0.0083

hovered at skid heights of 1, 6, 15, 24, 39, and 44 feet, was performed out of the influence of the EFP. Then, hover ladders were performed at predetermined locations approaching the EFP along a line extending from the centerline of the EFP. Finally, a similar procedure was performed with the rotor aligned with the port face of the EFP.

The test points at skid-heights of fifteen feet (a rotor height of approximately one rotor radius), 98% rotor speed, and two different hover locations were replicated in OVERFLOW-CHARM simulations. At the first location, the UH-60L hovers 34 feet from the nearest face of the EFP, measured to the pilot's "bumline". At the second location, the UH-60L hovers over open tarmac. These points provide a comparison of the aerodynamics when the rotor wake is and is not interacting with the EFP. The wind conditions during these tests were approximately 5.5 knots at 217° from north, corresponding to 80 degree sideslip. This condition will be referred to as the "sideslip condition". To examine the capabilities of OVERFLOW-CHARM when the helicopter is fully immersed in the wake, simulations with winds directly aligned with the EFP center line (zero degree helicopter sideslip) at five knots were also performed. This condition will be referred to as the "downwind condition". Table 6.1 defines the freestream values for the sideslip and downwind conditions.

6.3 Simulation Methodology

A one-way coupled approach to DI modeling was utilized to replicate the experimental conditions due to the cost-savings it provides over a unified approach, and to take full advantage of the cost-saving and modeling capabilities of OVERFLOW-CHARM. Thus,

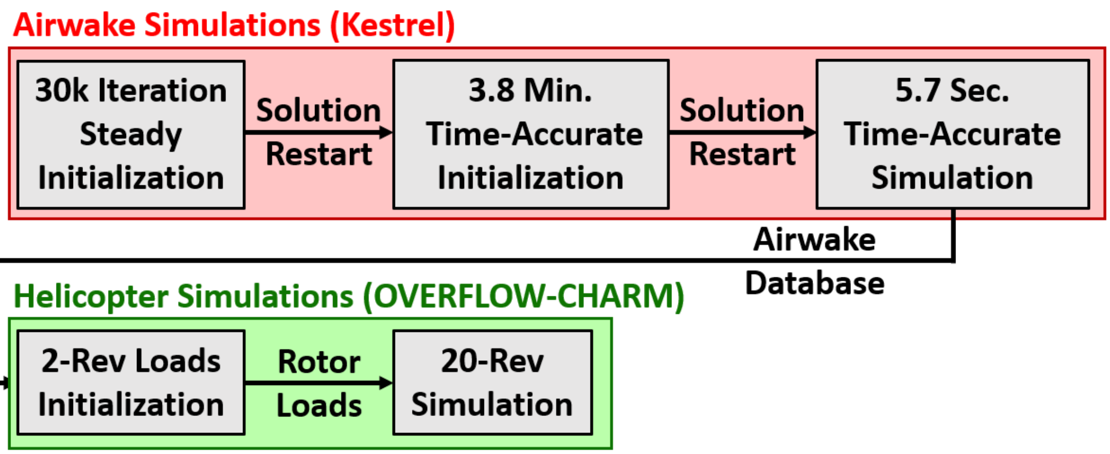

Figure 6.1: Flow chart of procedure for performing LOIDR simulations.

two separate classes of simulations were performed. First, simulations of the EFP at the recorded ambient wind conditions were performed in High-Performance Computing Modernization Program (HPCMP) Computational Research and Engineering Acquisition Tools and Environments (CREATE™)-Air Vehicles (AV) Kestrel. From these simulations, airwake data were extracted for a large control volume around the helicopter position. Then, the airwake database was coupled to an OVERFLOW-CHARM simulation of the UH-60L helicopter at identical experimental conditions. This process is illustrated in Figure 6.1. Simulations were run at standard sea level conditions with a rotor tip Mach number of 0.63. This approach to airwake coupling does not account for the influence of the helicopter aerodynamics on the EFP airwake. It is not, however, a superposition of flow fields, because the EFP airwake alters the CHARM rotor wake solution, which impacts the self-induced wake-element Biot-Savart calculations when the CHARM solution is advanced. This approach permits some prediction of nonlinear aerodynamic coupling between the airwake and the rotor wake while also allowing the re-use of the airwake database for multiple test points or different helicopters.

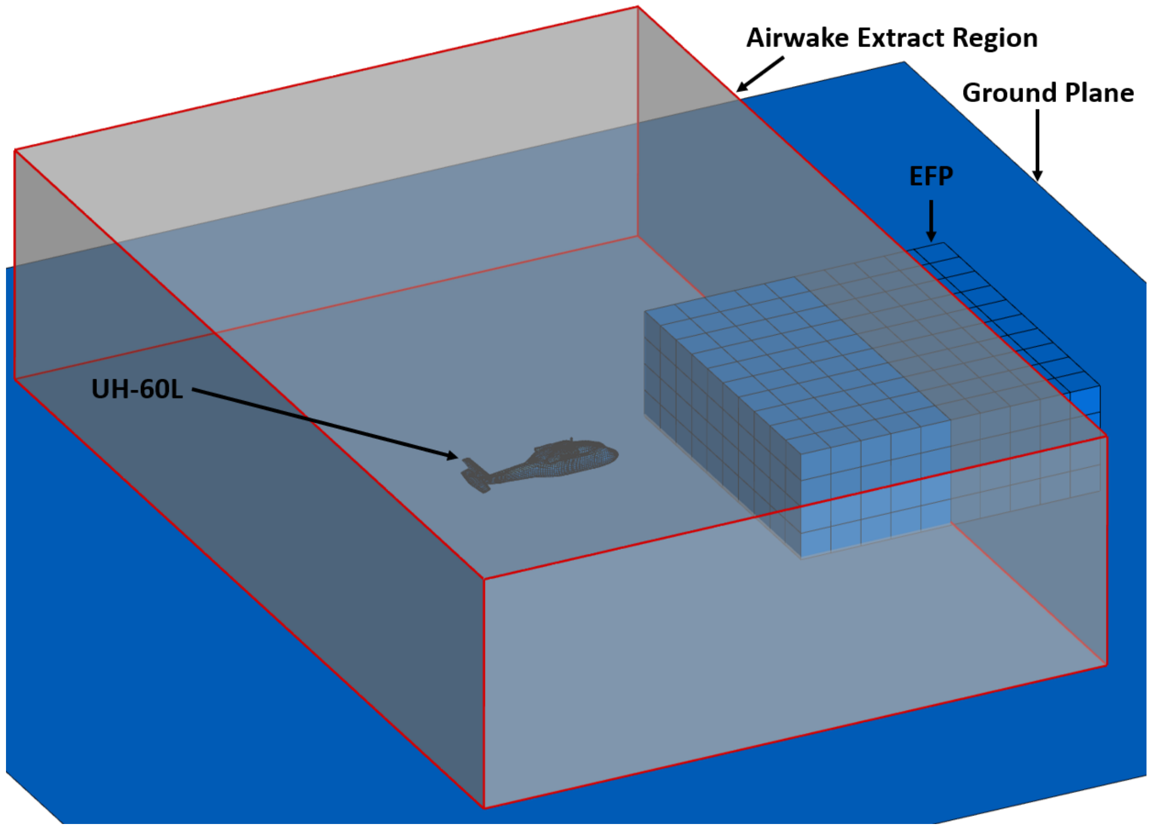

Figure 6.2: Airwake database region with respect to the EFP and UH-60L

6.4 Airwake Simulations

The airwake simulations were required to produce a time history of airwake data that exceeded the length of time over which OVERFLOW-CHARM would predict the rotorcraft response. To allow sufficient time for the simulation to converge and investigate unsteady fuselage and rotor loads, an airwake record length of 20 rotor revolutions was chosen. At the experimental rotor speed, this corresponds to 4.7 seconds of simulation, with an extra second required to initialize the CHARM wake. The extract volume, shown in Figure 6.2, encompasses the region of space in which the CHARM wake is modeled in the helicopter simulations and is made up of Cartesian cells at a resolution of one-foot (0.6 blade chords).

The simulations were performed in three stages. First, a steady simulation was performed to develop the EFP wake. Then, an unsteady simulation was performed with no data extracted to develop accurate unsteadiness in the wake. Finally, an unsteady simulation generated the final airwake data, extracted onto the three-dimensional Cartesian grid described previously. The extracted data were converted to a simplified format containing only velocity deviations from the nominal freestream velocity and normalized by the freestream speed:

$$\vec{u}_{airwake} = \frac{\vec{u}_{extract} - \vec{u}_{\infty}}{\|\vec{u}_{\infty}\|}. \tag{6.1}$$

This circumvents the need for unit conversions between the airwake and helicopter simulations.

6.4.1 Computational Meshes

The computational mesh for the airwake simulations was an unstructured mesh composed of tetrahedral, prism, and pyramid cells generated by the program Heldenmesh [158–160] (see Figure 6.3). Heldenmesh merges a list of patches in the form of a GridTool restart file and an input file describing sources for grid refinement to create the unstructured surface and volume meshes. The EFP has a primary cell spacing one-foot, with half-foot cells along the edges. A refinement region was introduced in the operational area of the helicopter containing one-foot cells. The cell sizes gradually grow from the refinement region to a maximum size of fifty feet. The far field boundaries are approximately 5000 feet from the EFP and the top of the bounding box is 1000 feet high. Boundary layer T-Rex cells are grown from the ground plane and EFP surfaces with a first cell spacing of 0.0000132, which corresponds to a $y^+ \leq 1$. The grid contained a total of 81 million cells.

6.4.2 Numerical Options

The airwake simulations employed the compressible formulation of KCFD, Harten-Lax-van Leer-Einfeldt (HLLE)++ scheme for inviscid flux computation, Limited Directed Difference (LDD)+ scheme for viscous flux computation, second-order spatial accuracy, and the Menter Shear-Stress Transport (SST) Delayed Detached Eddy Simulation (DDES) turbulence model with wall function. The steady state simulations were evaluated for 30000

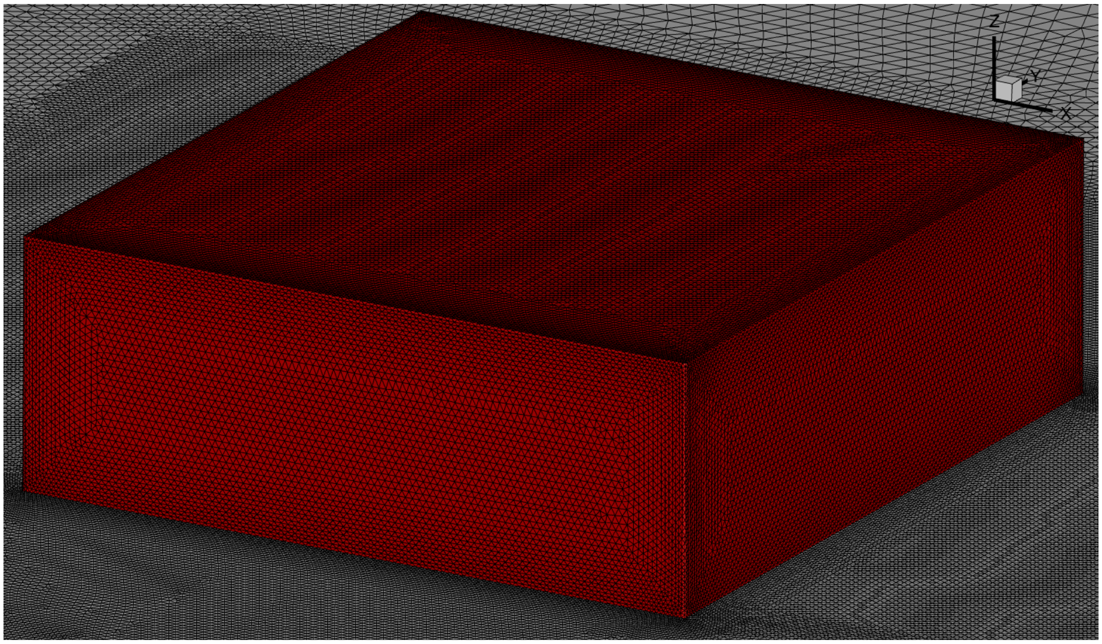

(a) EFP Surface Grid

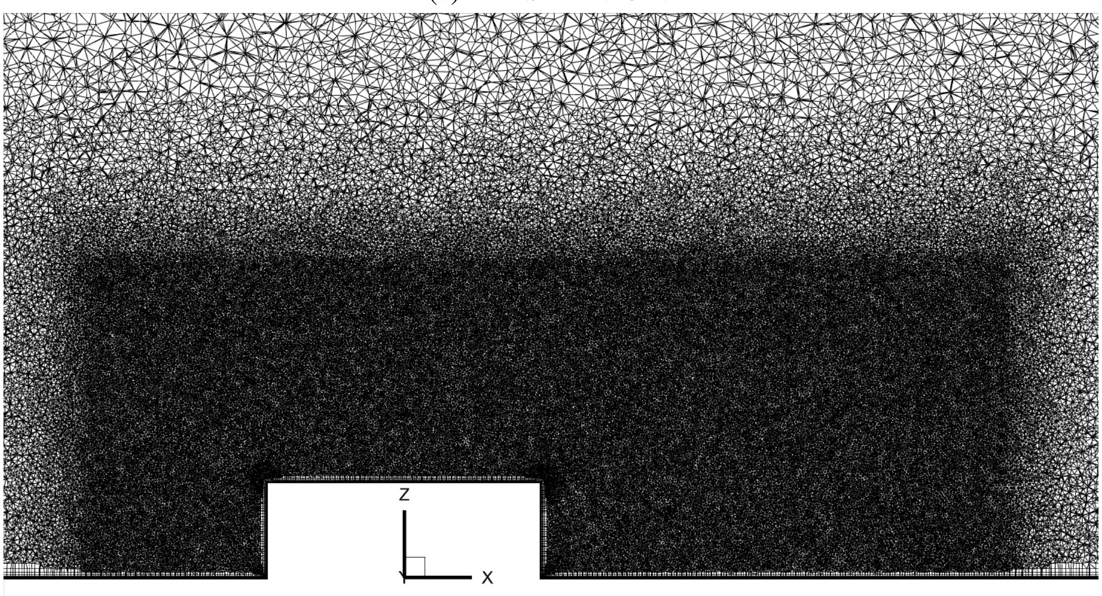

(b) Volume Mesh Slice

Figure 6.3: Illustrations of the unstructured EFP grid employed in the Kestrel airwake simulations.

iterations at a Courant–Friedrichs–Lewy (CFL) number of 1000 to develop the airwake. The unsteady simulations employed second-order Newton time stepping with a time step corresponding to 1000 steps (about 0.01 seconds) for a fluid particle to traverse the length of the EFP at the freestream velocity. Four subiterations were utilized, which was sufficient to provide a residual drop of at least three orders of magnitude. The unsteady flow field was initialized for 20000 iterations, and then another 2160 iterations were performed to generate the airwake extracts.

6.5 Helicopter Simulations

The UH-60L simulations employed lessons learned from the previous studies of the relevant aerodynamics in DI analysis. The rotor blades were resolved with non-contiguous OVERFLOW grids (see Figure 6.4). The fuselage and EFP were resolved with CHARM doublet panels. The ground was modeled as an image plane. Because transformations of the pilot controls to swashplate angles was not provided, cyclic angles were held at zero and the collective was trimmed by first computing a target rotor thrust based on gross weight and fuselage download. The fuselage download was calculated directly from pressures computed by the OVERFLOW-CHARM fuselage panel method. The gross weight was calculated from flight test data, where the empty weight of the helicopter and pilot weights were given. Fuel weight was calculated by subtracting the total fuel burned from the reported starting fuel. The total fuel burned was calculated by integrated the measured fuel burn rate from the start of the data collection period to the appropriate time of the selected test point, accounting for incremental burn during the simulated period. The algorithm for computing the target thrust is given below.

$Burned\_Fuel \leftarrow \int_{t_0}^{t_1} Fuel\_Burn\_Rate(t) * dt$

$Download \leftarrow \sum_{panels}(-Pressure * Z\_Unit\_Normal * Area)$

$Target\_Thrust \leftarrow (Download + Empty\_Weight + Pilot\_Weight + Start\_Fuel - Burned\_Fuel)$

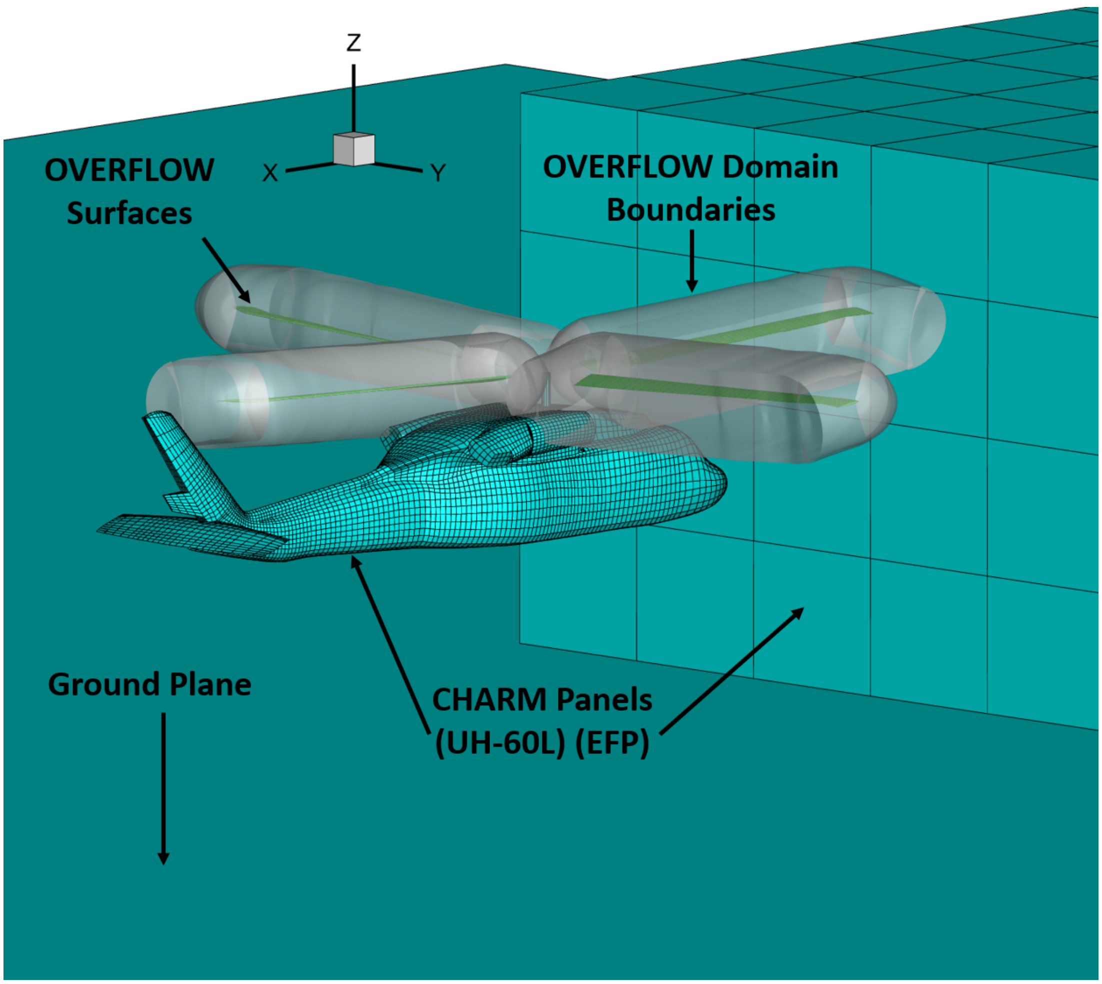

Figure 6.4: Diagram of the OVERFLOW-CHARM domain configuration.

Then, a blade motion file was generated with an updated collective to either increase or decrease the predicted thrust to approach the target thrust. The rotor coning angle was approximated from previous aeroelastic predictions of the UH-60 rotor assuming linearity with thrust. No elastic deflections of the blades were applied. This manual trimming procedure is in lieu of coupling to a flight dynamics or comprehensive code that is recommended for future expansion of this analysis.

6.5.1 Computational Meshes

The OVERFLOW blade grids were identical to the baseline blade grids employed in the study of Wilbur et al. [128, 129], which studied the ability of OVERFLOW-CHARM to make aeroelastic predictions of the UH-60A rotor. The grids were originally generated at Boeing and are typical for engineering applications. Each near-body blade grid consists of three million points, and is composed of a main blade C-mesh bounded by root and tip cap meshes. The surface of the blade was resolved by 302 points around the chord and 100 radial points, with 77 points extending in the wall-normal direction. The leading and trailing edge spacing corresponded to 0.3% and 0.05% of the reference chord, respectively. The first cell in the boundary layer had a thickness such that $y^+ = 1$, and there were approximately 46 points in the boundary layer.

The EFP and UH-60L fuselage were resolved with CHARM doublet panels. UH-60L was made up of 8,374 triangular and quadrilateral panels, as illustrated in Figure 6.5. This resolution is sufficient to resolve the geometry of the UH-60L and is much more detailed than is usually employed for stand-alone CHARM computations [161]. The EFP was made up of 220 rectangular panels, with ten panels along the length and width and four panels in the vertical direction.

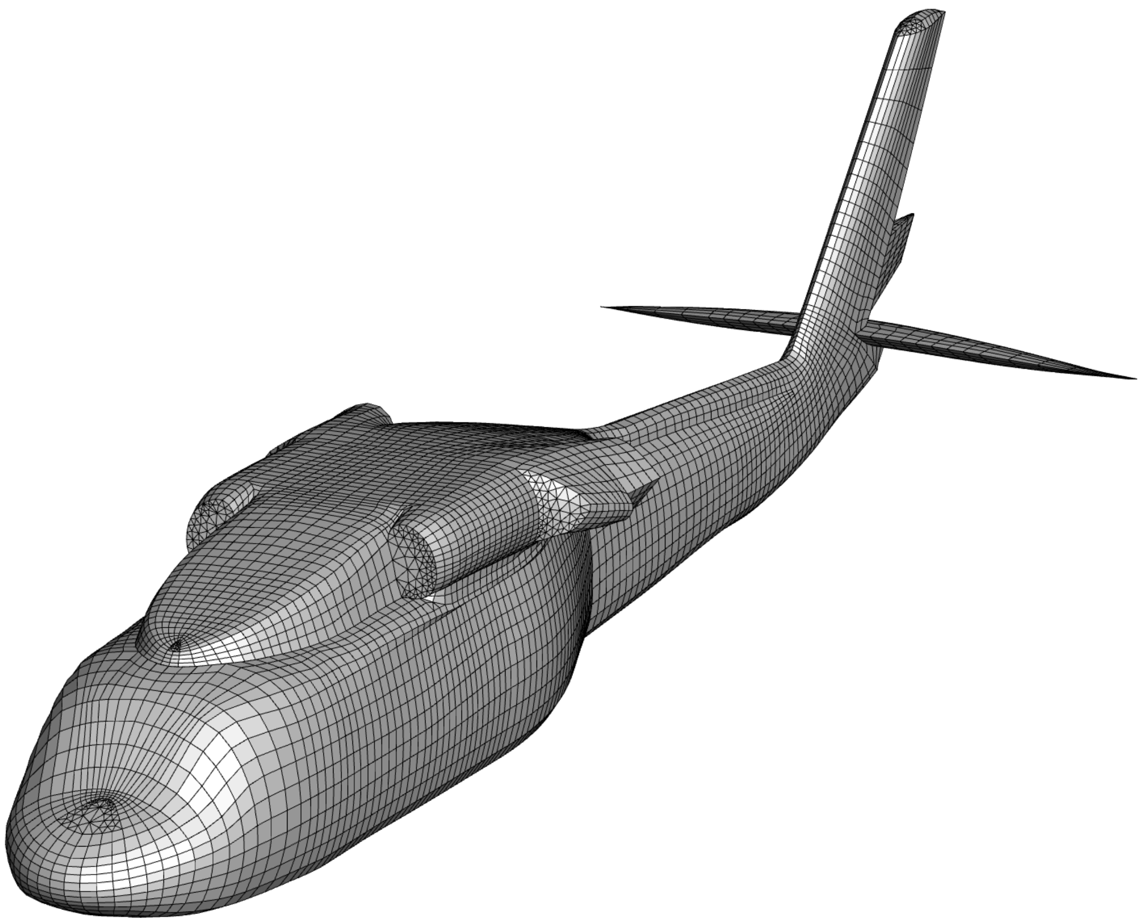

Figure 6.5: CHARM panels resolving the UH-60L fuselage.

6.5.2 Numerical Options

Numerical options are derived from the findings of the previous chapters. Time-advancement was performed with dual time stepping with forty subiterations and a minimum CFL number of five, which provided a residual drop of at least one order of magnitude. The physical time step was chosen so that the rotor advances 0.5 degrees per time step. The right-hand-side terms were discretized using fourth-order Roe upwind spatial differencing with 4/2 dissipation where the fourth- and second-order dissipation constants were 0.04 and 10.0, respectively. The left-hand-side terms were discretized using a diagonalized Beam-Warming scalar pentadiagonal scheme with fourth-order dissipation. The one-equation thin-layer Spalart-Allmaras (SA) turbulence model was applied with a rotational correction.

The CHARM model consisted of the EFP and UH-60L panels described earlier along with an image plane at ground level to resolve wake-body interactions. The CHARM rotor wake model was updated every five degrees of rotor rotation, retaining ten revolutions of full-span vortex elements and 20 revolutions of tip vortex elements. Artificial dissipation was applied near the ground plane to model the viscous interactions of the wake with the ground, as recommended by Continuum Dynamics, Inc. (CDI). The CHARM solution was initialized for six revolutions from blade loads predicted by a two-revolution OVERFLOW simulation. To prevent initial unsteady Reynolds-Averaged Navier-Stokes (uRANS) transients from disrupting the CHARM solution, blade loads were blended from the input loads beginning after one blade passage of coupled simulation and proceeding over the second blade passage, after which loads come solely from the uRANS solution.

6.6 Results

6.6.1 EFP Airwake Predictions

The airwake simulations were performed on the HPCMP computing cluster "Onyx" on 704 Intel®E5-2699v4 Broadwell processors at 2.8 GHz. Each calculation took approximately sixty hours of wall time, translating to about 42,000 CPU-hours. 92% of this time was spent initializing the flow field before airwake database extraction. Because the airwake extraction portion of the simulation constitutes such a small fraction of the total, lengthening the record length of the airwake database would not incur significant additional cost in the airwake simulations for applications where long record lengths of airwake data are required, i.e. a fully simulated shipboard approach.

Slices of the flow field after each stage of flow field initialization are illustrated in Figure 6.6 and Figure 6.7. Because mesh refinement only extends 172 feet in the x-direction behind the EFP, the steady-state simulation of the downwind case is unable to develop the airwake beyond this distance. The unsteady initialization simulations further develop the airwake and time-accurately resolve the unsteadiness in the separated flow. At the sideslip condition, the unsteady initialization also resolves the secondary wake that is shed from the lower corner of the EFP, observed directly below the UH-60L position in Figure 6.7.

The fully developed airwakes for the downwind and sideslip conditions are illustrated in Figure 6.8, with the location of the UH-60L in the coupled simulations displayed for reference. At the downwind condition, the UH-60L is fully immersed in the airwake of the EFP, whereas in the sideslip condition, the shear layer at the boundary of the airwake impinges directly on the UH-60L fuselage. As observed in Figure 6.9, which illustrates a time-history of the cardinal velocities along the center line of the eventual UH-60L fuselage position, full immersion within the airwake results in velocity fluctuations of approximately six ft/s. In Figure 6.10, velocities are much more variable in both space and time, with fluctuations as much as ten ft/s. The dominant period for oscillations is approximately 1-2

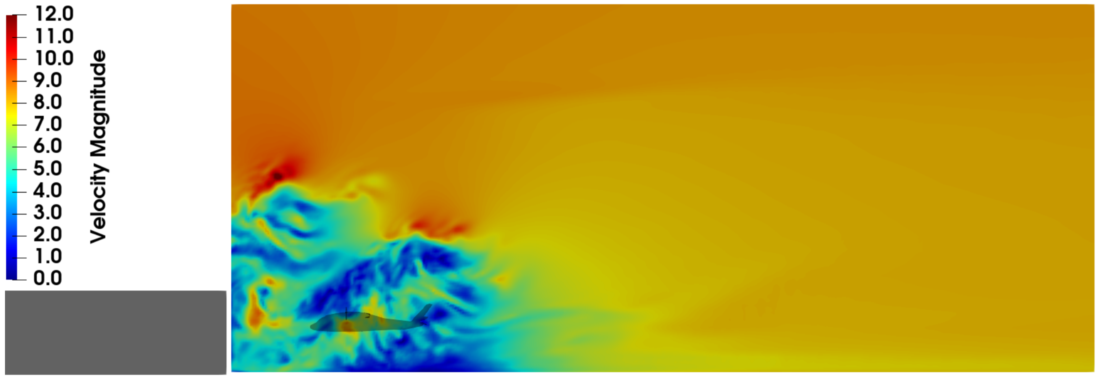

(a) Steady Restart

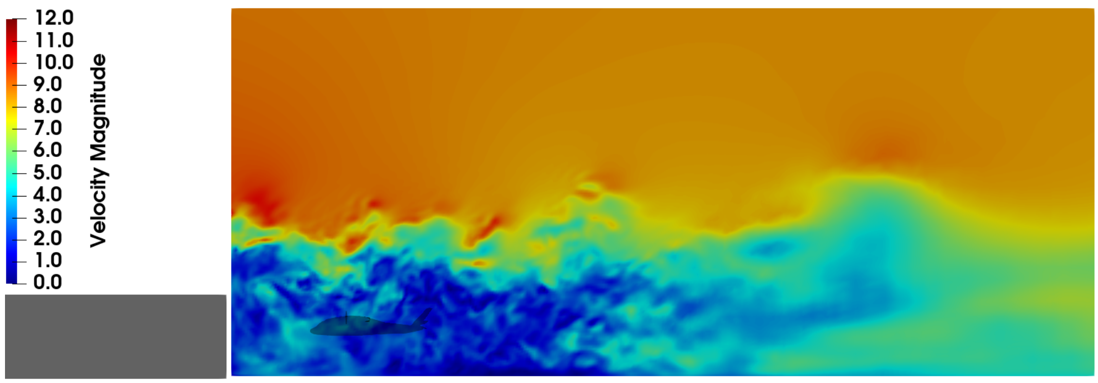

(b) Unsteady Restart

Figure 6.6: Slice of solution after steady-state and unsteady initialization calculations for the downwind airwake (fuselage not present in the simulation). EFP shown in gray.

seconds in time and 5-10% of the fuselage length in space. The magnitude and temporal and spacial frequencies of these oscillations indicate that strong forces and moments are expected to be imparted on the fuselage in the coupled simulation at the sideslip condition, particularly side force and yawing moment from the airwake impinging on the nose of the fuselage.

(a) Steady Restart

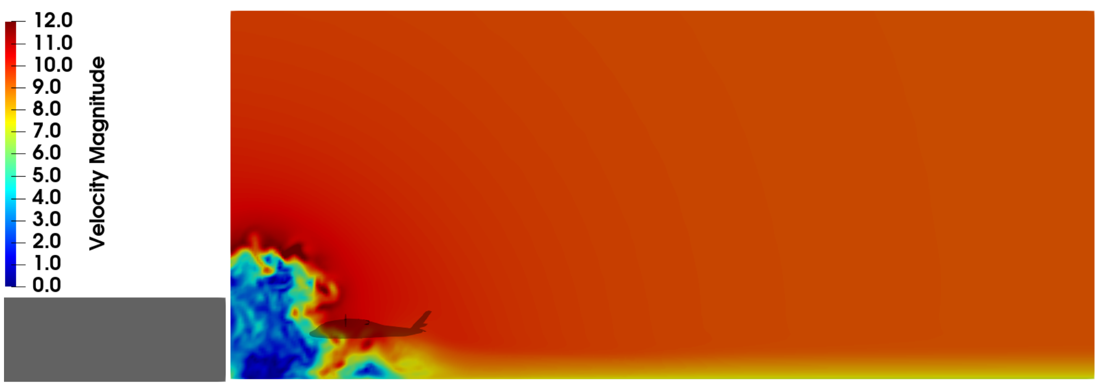

(b) Unsteady Restart

Figure 6.7: Slice of solution after steady-state and unsteady initialization calculations for the sideslip airwake (fuselage not present in the simulation). EFP shown in gray.

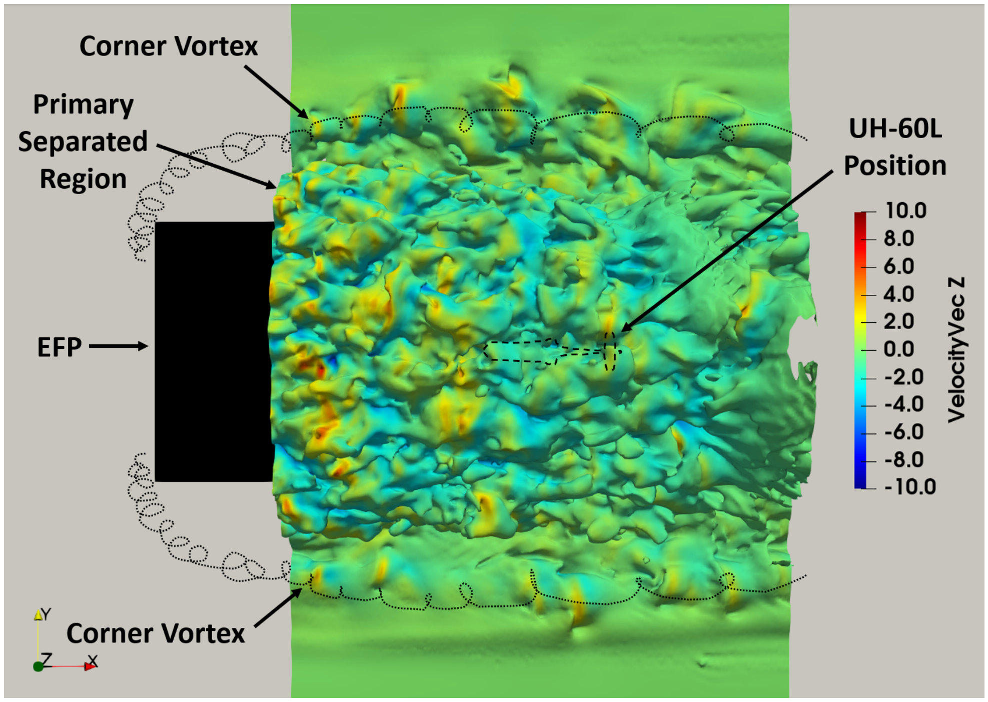

(a) Downwind Condition

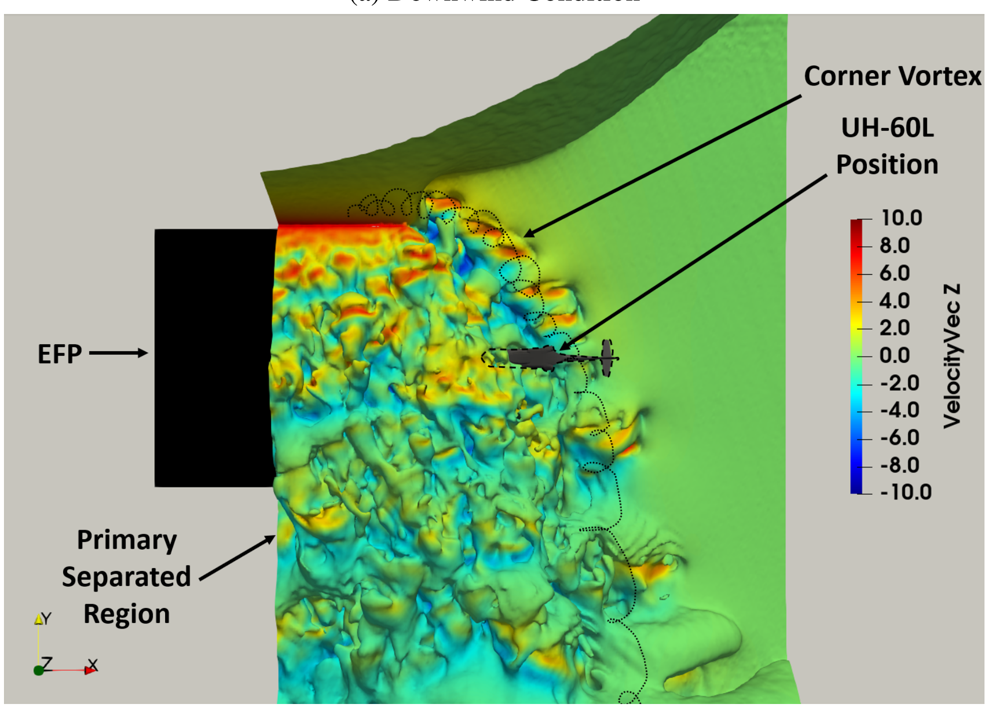

(b) Sideslip Condition

Figure 6.8: Isosurfaces of velocity magnitude equal to the free-stream wind speed colored by upwash velocity at the midpoint of the airwake database record (fuselage not present in the simulation). EFP shown in black.

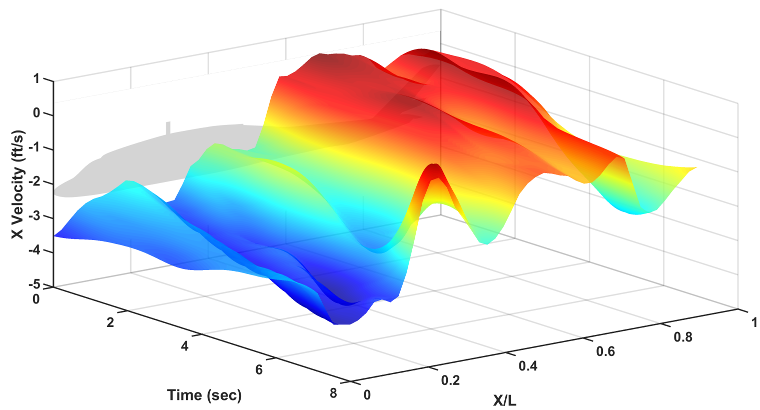

(a) X Velocity

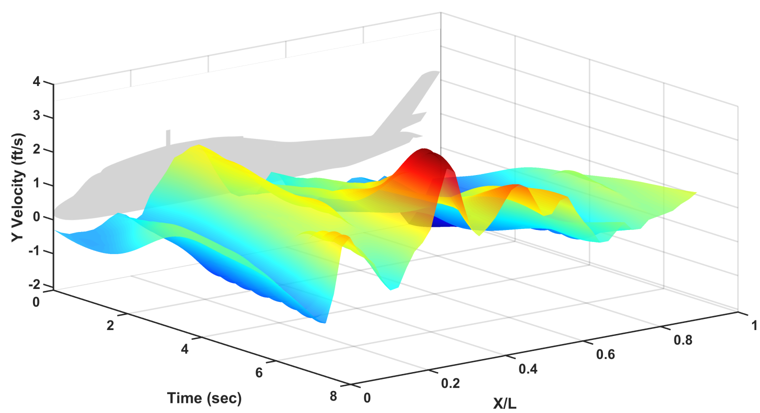

(b) Y Velocity

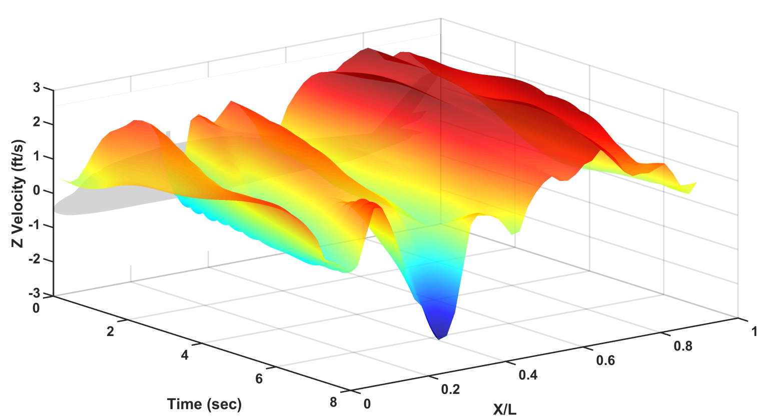

(c) Z Velocity

Figure 6.9: Time history of airwake velocities extracted along the centerline of the hover position of the UH-60L fuselage for the downwind airwake (fuselage not present in the simulation).

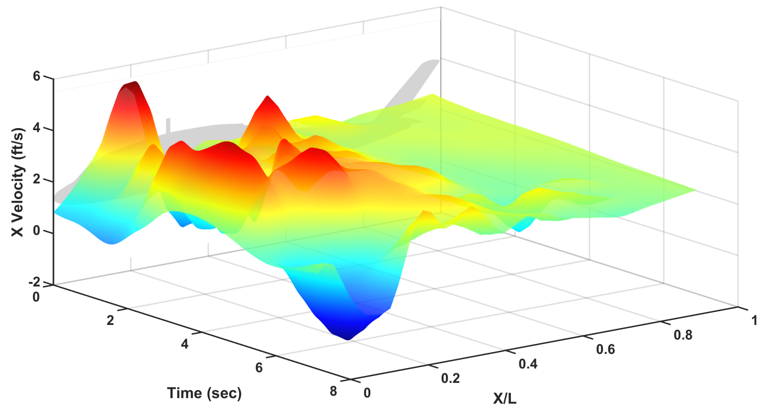

(a) X Velocity

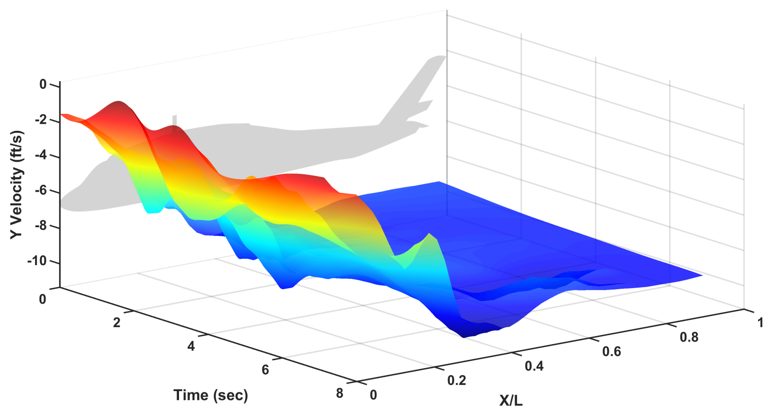

(b) Y Velocity

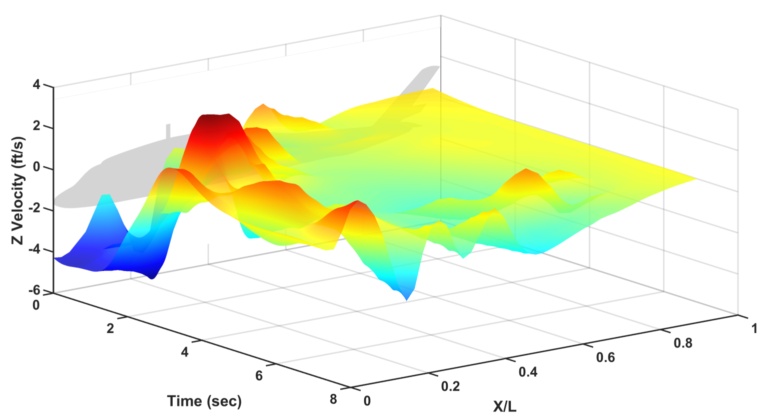

(c) Z Velocity

Figure 6.10: Time history of airwake velocities extracted along the centerline of the hover position of the UH-60L fuselage for the sideslip airwake (fuselage not present in the simulation).

6.6.2 OVERFLOW-CHARM Downwind Condition Simulations

Flow Field

Observing the CHARM-induced flow fields after 1.6 seconds of simulated time at the downwind condition condition in Figure 6.11, the effect of airwake coupling is most clearly visible by its effect on the trajectory of the rotor wake. Without airwake coupling, the CHARM vortex wake elements are convected by the full freestream velocity, and the rotor wake behaves as if it were in a forward flight, with some impingement of the blade tip vortices on the nose of the fuselage. With airwake coupling, the CHARM vortex wake elements are instead immersed in the wake of the EFP and are convected by the low-speed flow in this separated region. As a result, the wake behaves more like a hover condition, and wake spreading due to the ground effect causes the blade tip vortices to pass well in front of the fuselage nose. The change in wake trajectory also determines how the blade tip vortices interact with the stabilator. Some recirculation of the rotor wake is observed in the high velocity region near the EFP face, but blade tip vortices are generally dissipated by the time they rise to the rotor plane. While this effect is partially due to vortex elements older than six revolutions being truncated (increased to ten revolutions in the sideslip simulations), the panel method at the EFP face does not provide a sufficient boundary condition to prevent vortex elements from entering the EFP, particularly when they approach the intersection of the EFP with the ground plane. Increasing the resolution of the EFP panels does not prevent this from occurring.

Fuselage Loads

The metric of interest during DI operations is pilot workload, which is generally quantified with subjective pilot assessments during flight tests and are not part of this work. When attempting to correlate wind tunnel or computational aerodynamic predictions to pilot workload, previous authors have determined that the most important factor is unsteadiness in the

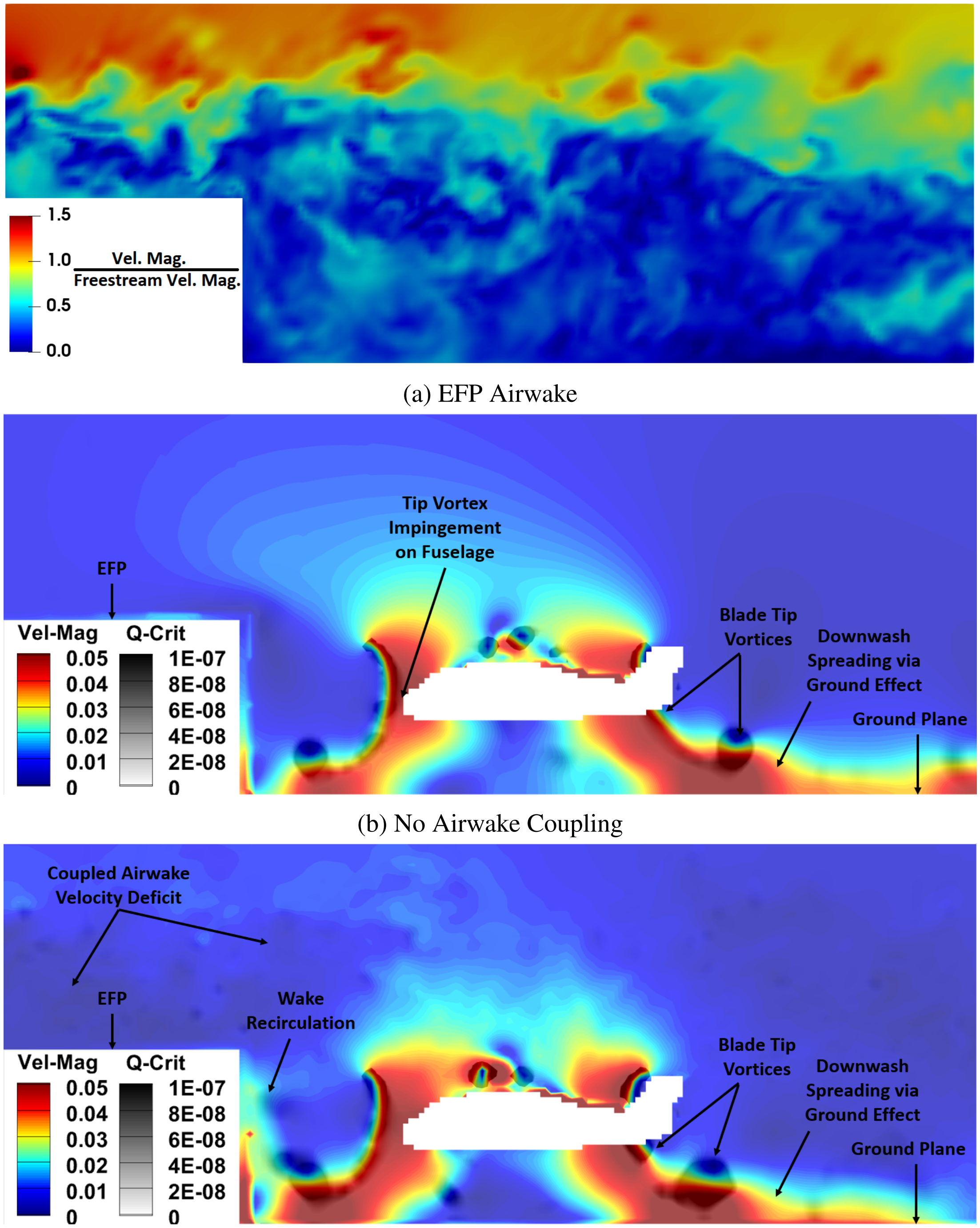

(a) EFP Airwake

(b) No Airwake Coupling

(c) With Airwake Coupling

Figure 6.11: Comparison of CHARM-induced flow fields at t = 1.6 seconds for OVERFLOW-CHARM simulations of the downwind condition with and without airwake coupling.

helicopter fuselage loads, particularly side and drag forces [56]. Making quantitative correlations of predictions of fuselage loads by OVERFLOW-CHARM to vehicle motion, pilot control inputs, and workload is left for future work, but qualitative comparison is made to investigate the capabilities of airwake-coupled OVERFLOW-CHARM simulations. The fuselage loads were filtered using a moving average filter:

$$F_{filtered}(t) = \overline{F_{raw}\left(t - t_b/2 : t + t_b/2\right)}. \tag{6.2}$$

where t_b is the temporal length of one blade passage. This equation filters out oscillations at and above the blade passage frequency, which dominate the time histories of the fuselage loads. Because the blade passage frequency (16.9 Hz) is high enough that the resulting oscillations do not require a pilot response to counteract and are instead perceived as vibrations and structural noise, the filtered loads provide a better indication of variations in forces and moments that will affect aircraft motion. The reference point for reported moments is the origin of the computational domain, located at the center of the rotor disk.

The impact of including airwake coupling in the OVERFLOW-CHARM simulations was investigated by comparing fuselage loads predicted with and without airwake coupling at the downwind condition. The most prominent influence on the statistics (see Table 6.2) is a drop in the mean longitudinal force, resulting from the immersion of the fuselage within the separated flow region of the EFP. The Root-Mean-Squared (RMS) forces and moments are also reduced by about 39% with the inclusion of airwake coupling, likely due to the reduced velocity magnitudes within the EFP airwake and the difference in the rotor wake trajectory. The reduction in fuselage force variation may indicate that airwake coupling is necessary for accurate characterization of aircraft motion when the helicopter is operating in large regions of separated flow.

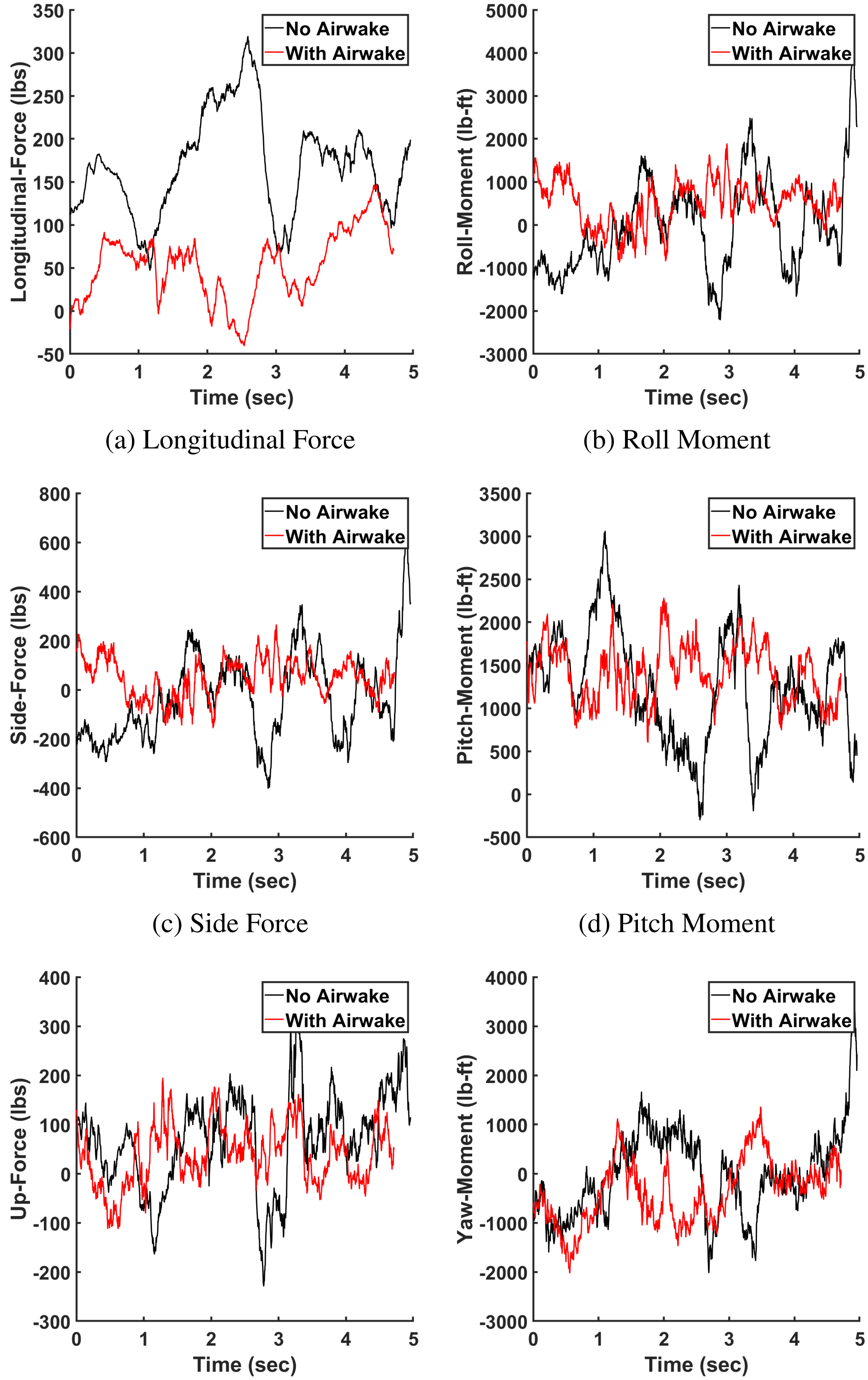

Figure 6.12: Filtered time histories of OVERFLOW-CHARM-predicted fuselage forces with and without airwake coupling at the downwind condition (see Equation 6.2).

Table 6.2: Table of OVERFLOW-CHARM-predicted fuselage force and moment statistics at the sideslip condition. Forces are in lbs, moments are in lb-ft.

Simulation	**Long. Force**		**Side Force**		**Vertical Force**	
Configuration	**Mean**	**RMS**	**Mean**	**RMS**	**Mean**	**RMS**
No Airwake	181	100	-39	159	48	111
With Airwake	53	44	45	72	21	84
Simulation	**Roll Moment**		**Pitch Moment**		**Yaw Moment**	
Configuration	**Mean**	**RMS**	**Mean**	**RMS**	**Mean**	**RMS**
No Airwake	-66	983	1305	790	-66	983
With Airwake	474	469	1345	700	-262	607

6.6.3 OVERFLOW-CHARM Sideslip Condition Simulations

Flow Field

Figure 6.13 compares the OVERFLOW-CHARM-predicted flow fields after 2.8 seconds of simulated time at the sideslip condition without the EFP, with the EFP and no airwake coupling, and with the EFP including airwake coupling. Without the EFP, the flow field closely in front of the fuselage resembles that of the isolated rotor in ground effect predictions of the previous chapter. Behind the fuselage, interactions of the blade tip vortices and the UH-60L tail result in more dispersed vortices than at the nose. When the EFP panels are included in the model, rotor wake upwash is observed at the face of the EFP and tip vortices recirculate towards the rotor plane. Tip vortices at the front of the aircraft coalesce into larger vortices, whereas without the EFP, they remain spread along the slipstream boundary. When airwake coupling is included, these tip vortices again become spread along the slipstream boundary, and more pronounced rotor wake recirculation is observed. The velocity deficit within the separated flow region of the EFP airwake is clearly visible in the region around the EFP. The fully coupled flow fields at both the sideslip and downstream conditions contain the major features of the DI including separated flow from bluff body structures, deflection of the rotor wake with solid surfaces, rotor wake recirculation at solid walls, and rotor wake interactions with the helicopter fuselage. To improve the consistency of achieving these promising results, methods for preventing the ingestion of the rotor wake

Table 6.3: Table of OVERFLOW-CHARM-predicted fuselage force and moment statistics at the sideslip condition. Forces are in lbs, moments are in lb-ft.

Simulation Configuration	Long. Force		Side Force		Vertical Force	
	Mean	**Variance**	**Mean**	**Variance**	**Mean**	**Variance**
No EFP	76	148	-192	179	71	102
EFP, No Airwake	74	150	-124	212	73	84
EFP, With Airwake	31	89	-197	161	69	90
Simulation Configuration	**Roll Moment**		**Pitch Moment**		**Yaw Moment**	
	Mean	**Variance**	**Mean**	**Variance**	**Mean**	**Variance**
No EFP	-1195	1072	893	1835	37	604
EFP, No Airwake	-775	1313	776	1882	-61	639
EFP, With Airwake	-1262	962	1090	1502	-84	354

at concave corners in the CHARM panel method should be investigated. Artifacts in the induced flow field, observed at points very near the fuselage and EFP, are the result of the panel method enforcing no slip across the panels. Because this is an induced flow field and not directly representative of the CHARM solution, these artifacts do not impact the fidelity of the CHARM solution.

Fuselage Loads

At the sideslip condition, the differences in predicted fuselage loads between simulations with and without the EFP and with and without airwake coupling are less pronounced than for the downwind condition. No clear trend is visible for the influence of the EFP on the fuselage force statistics in Table 6.3, though the instantaneous forces are heavily influenced by the presence of the EFP, as observed in Figure 6.14. When airwake coupling is included, the mean longitudinal force drops from about 75 lbs to 31 lbs. As with the downwind condition, RMS forces and moments are generally reduced when airwake coupling is included, though only by 17% at this condition.

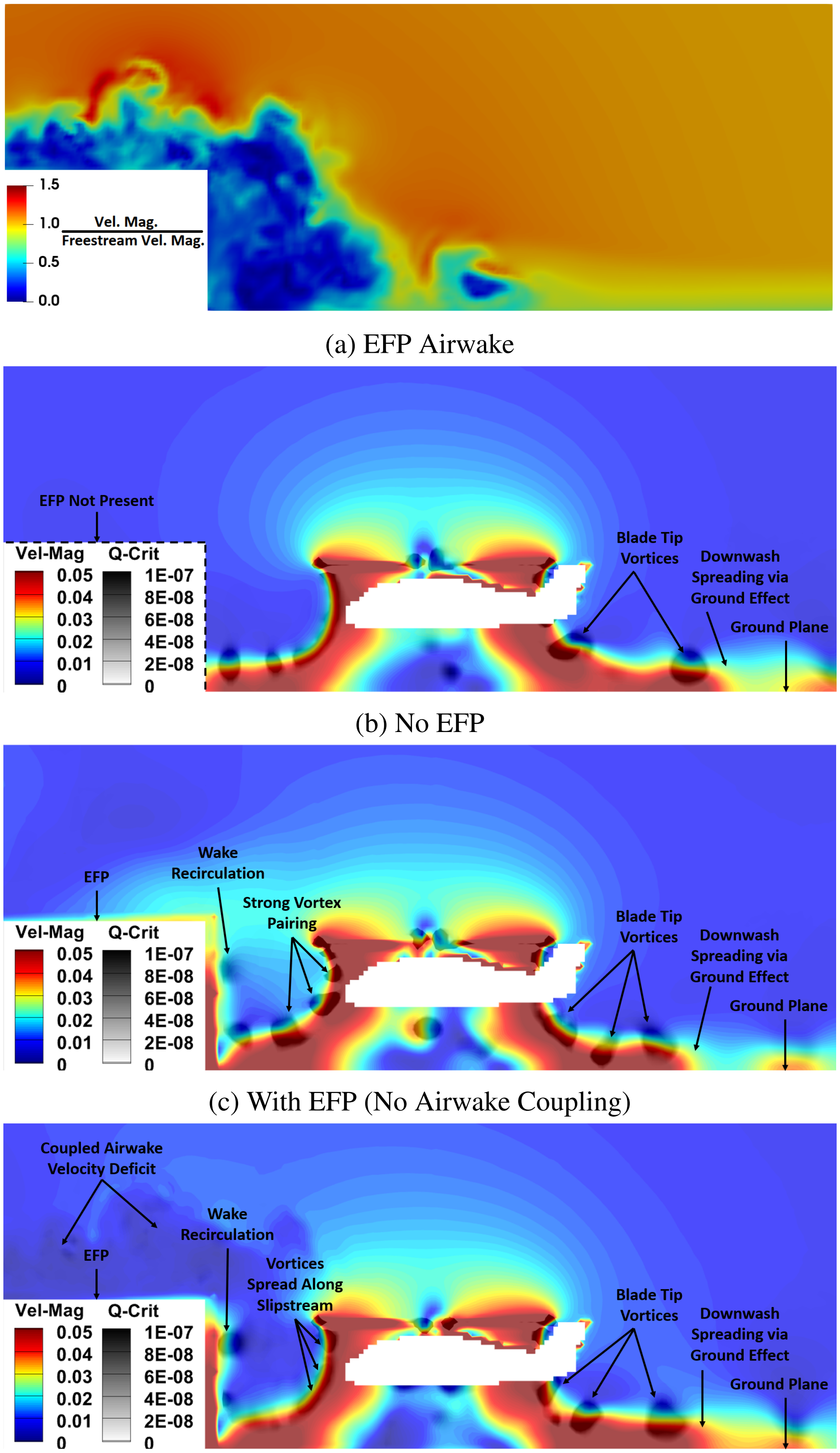

(a) EFP Airwake

(b) No EFP

(c) With EFP (No Airwake Coupling)

(d) With EFP (With Airwake Coupling)

Figure 6.13: Comparison of CHARM-induced flow fields at t = 2.8 seconds for OVERFLOW-CHARM simulations of the sideslip condition with and without the EFP present and with and without airwake coupling.

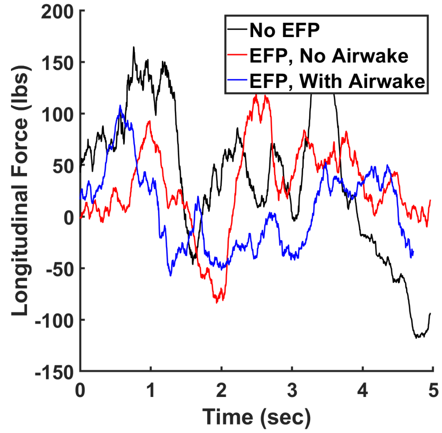

(a) Longitudinal Force

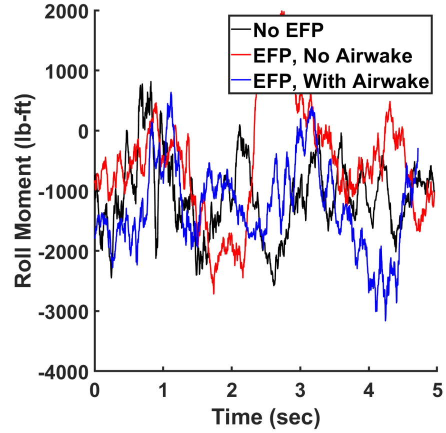

(b) Roll Moment

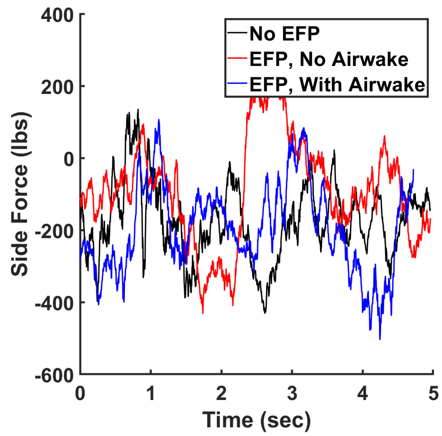

(c) Side Force

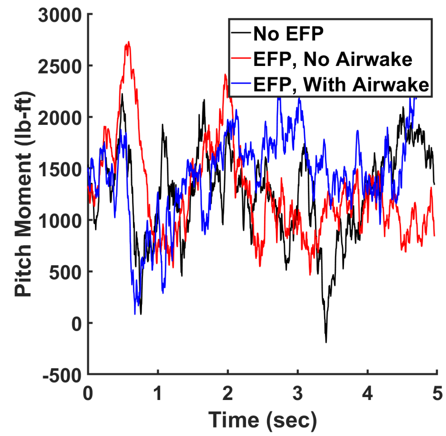

(d) Pitch Moment

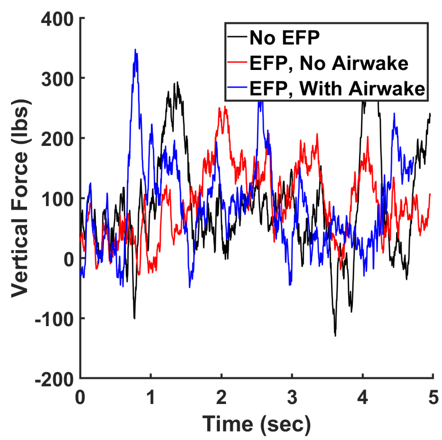

(e) Vertical Force

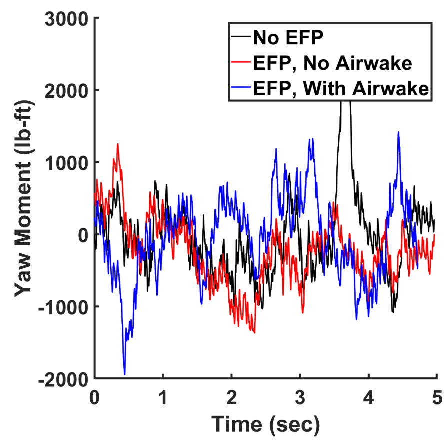

(f) Yaw Moment

Figure 6.14: Filtered time histories of OVERFLOW-CHARM-predicted fuselage forces with and without the EFP at the sideslip condition (see Equation 6.2).

6.6.4 Correlating Fuselage Loads to Flight Test Acceleration Measurements

The flight test data provides time histories of aircraft acceleration at the sideslip condition with and without the EFP. As a preliminary step towards correlating the fuselage forces to aircraft motion, "events" in the fuselage forces and flight test accelerations are compared. Events are classified by their temporal length t_e, and are are defined as deviations of length t_e from the trend in the signal. The below algorithm is employed to identify the frequency of events in a signal (fuselage forces or acceleration data) having temporal lengths between $t1$ and $t2$.

$t1\_Filtered\_Signal(t) \leftarrow mean(Signal(t - t1/2 : t + t1/2))$

$t2\_Filtered\_Signal(t) \leftarrow mean(Signal(t - t2/2 : t + t2/2))$

$Filter\_Difference \leftarrow (t2\_Filtered\_Signal - t1\_Filtered\_Signal)$

$Zeros \leftarrow find\_roots(Filter\_Difference)$

for $i = 1 : N\_Zeros$ **do**

  if $t1 < (Zeros(i + 1) - Zeros(i)) < t2$ **then**

    $Event\_Count = Event\_Count + 1$

  end if

end for

$Event\_Frequency \leftarrow (Event\_Count/Signal\_Length)$

An example of the result of this procedure for $t1 = 0.2$ seconds and $t2 = 0.4$ seconds is provided in Figure 6.15. Events are categorized by their length in seconds and the frequency of events having various lengths are compared between the fuselage longitudinal and side forces and flight test longitudinal and lateral accelerations, illustrated in Figure 6.16. The most common events in both the flight test and computational data have lengths between 0.2 and 0.8 seconds, generally decreasing in frequency as event length increases. OVERFLOW-CHARM generally overpredicts the frequency of events, likely due to somewhat exaggerated unsteadiness in the CHARM vortex wake method, which

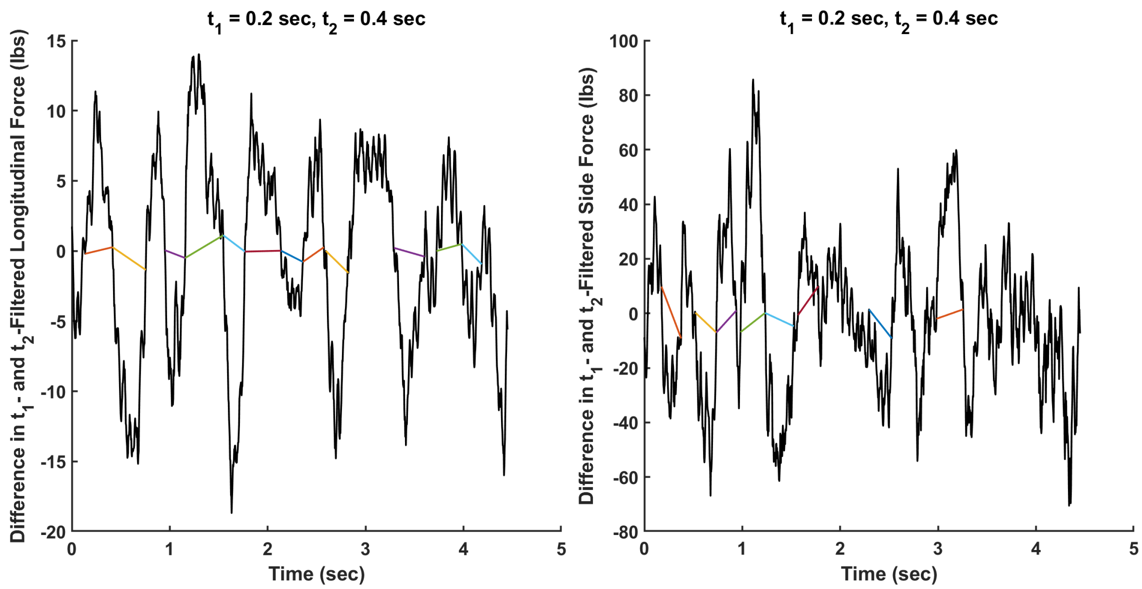

(a) Longitudinal Force

(b) Side Force

Figure 6.15: An example of how events of lengths 0.2-0.4 seconds (colored lines) are identified in the OVERFLOW-CHARM fuselage force time histories.

was observed in the previous chapters. Events longer than one second occur infrequently in all data sets, and due to the relatively short record length of the OVERFLOW-CHARM data (4.7 seconds compared to 50 seconds for the flight test), these longer events are more difficult to correlate to the flight test controls data. The most prominent effect of the EFP in the flight test data is the increase in occurrence rate of events between 0.2 and 0.4 seconds, which is also predicted by OVERFLOW-CHARM. The occurrence rate of longer events in both the flight test data and OVERFLOW-CHARM predictions are less affected by the presence of the EFP and its airwake.

6.6.5 Computational Cost

Conventional uRANS simulations of configurations such as this one have the primary downside that the rotor and ship (in this case, replaced with the EFP) airwakes must be developed using the same time step. While the ship airwake can be initialized at a larger time step before the helicopter is placed into the simulation, once the rotor blades are turning, the entire fluid domain must be computed at the time step constrained by the motion

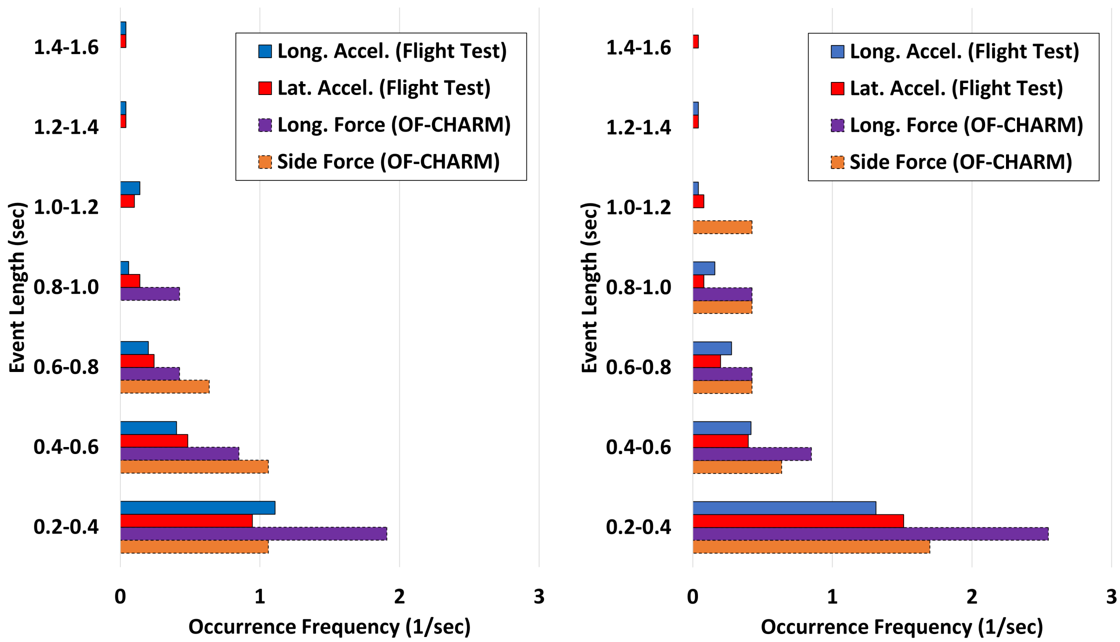

(a) No EFP

(b) With EFP

Figure 6.16: Occurrence rate of events of various lengths in time histories of OVERFLOW-CHARM-predicted fuselage longitudinal and side forces and flight test longitudinal and lateral accelerations with and without the EFP.

of the rotor blades. For such simulations to be tractable, the rotor-constrained time step must be increased with the use of actuator disk methods, which sacrifice the time-accurate capture of rotor wake physics. With this OVERFLOW-CHARM methodology, the "ship" airwake is initialized ahead of time, but during the time period of interest, the ship airwake solver is constrained to the time step of the free-wake solution (e.g. five degrees of rotor rotation), rather than the uRANS time step of the rotor (e.g. 0.5 degrees of rotor rotation).

An additional source of computational cost in pure uRANS simulations is performing domain connectivity of the overlapping grids as the helicopter moves relative to the ship and as the blades move relative to the helicopter. Polsky et al. reported that this procedure alone accounted for 54% of the CPU-hours per step of uRANS DI analysis when the helicopter is close to the ship. With the non-contiguous OVERFLOW-CHARM methodology utilized in this research, domain connectivity is only performed between the grids for each blade and amounts to less than 1% of the CPU-hours per step.

In total, the analyses presented here required 2,800 CPU-hours per second of simulated time for each test point. If the UH-60L were to be included in the airwake simulation, employing the same blade grids and an additional 20 million point uRANS fuselage grid, the computational cost would be approximately 19,000 CPU-hours per second of simulated time, including the additional cost of performing domain connectivity. As such, OVERFLOW-CHARM constitutes an estimated 85% cost savings compared to an equivalent uRANS simulation of the same configuration. The analyses of Polsky et al. required 5,000 CPU-hours per second of simulated time *for an actuator disk rotor model and a relatively coarse mesh of only 17 million total points.

The addition of airwake coupling to the OVERFLOW-CHARM simulation increased the CHARM step time from 26.26 seconds to 27.18 seconds, demonstrating that the interface between CHARM and the airwake database is highly computationally efficient.

6.7 Concluding Remarks

This demonstration of OVERFLOW-CHARM's application to analysis of the physics of the DI provides valuable insight into the capabilities of a state-of-the-art hybrid uRANS/free-wake solver for characterizing DI aerodynamics. OVERFLOW-CHARM can capture the fundamental physical features of the DI at approximately 85% less computational cost than conventional uRANS methods. The effect of DI interactions on unsteady fuselage loads are also correlated with those predicted by flight test data. Analysis of predictions of fuselage force variation indicates that airwake coupling may be vital for accurate characterization of aircraft motion when the helicopter is operating in large regions of separated flow. Improvements to panel method settings in the free-wake solver are recommended to avoid intermittent non-physical solutions when blade tip vortices approach convex corners of solid bodies. Coupling OVERFLOW-CHARM to a precomputed airwake database is highly cost efficient, with a less than 0.5% impact on the computational cost compared to uncoupled simulations. The precomputed the airwake can also be re-used for various helicopter positions or for different aircraft models, making it more efficient for routine DI analysis than a unified approach to DI simulation.

CHAPTER 7
CONCLUSIONS

7.1 Technical Findings

7.1.1 Hybrid Solver Extensions

To facilitate high quality predictions of the relevant aerodynamics in Dynamic Interface (DI) analysis, several improvements to the state-of-the art in hybrid Computational Fluid Dynamics (CFD) methods were necessary. First, the coupling interface should to be generalized to handle arbitrary rotor transformations and number of rotors in the simulation due to the complexity of the flow physics in realistic configurations and flight conditions. Second, blade deformation needed to be made agnostic to the structural coupling method to simplify rigid motion cases and further generalize this category of methodologies. Third, Single-Gridded-Blade (SGB) capabilities were added to maximize potential cost savings. Fourth, initialization of the unsteady Reynolds-Averaged Navier-Stokes (uRANS) solution to wake-induced values was developed to improve the convergence rate and minimize initial uRANS transients. Fifth, improvements to the near-body free-wake boundary condition for highly unsteady conditions were required, including the unsteady potential function's contribution to pressure, more thoughtful treatment of incoming characteristics, and advanced boundary value interpolation methods. Finally, airwake coupling was integrated into the solver. The benefits of each improvement were demonstrated and quantified.

7.1.2 Rotor-Wing Aerodynamic Interactions

The study of OVERFLOW-CHARM's application to aerodynamic analysis of wing-integrated propulsion system demonstrates its ability to provide accurate predictions of interactional aerodynamic effects at reduced computational cost when compared to conventional uRANS methods. It was determined that the off-body grids can be reduced to a disk encompassing the blades, and that OVERFLOW-CHARM can predict nonlinear aerodynamic effects of static lifting bodies on rotor/propeller performance within 1% of conventional uRANS methods. OVERFLOW-CHARM was also able to predict detailed interactional aerodynamic effects of the rotor/propeller on the static body pressure distribution, and provided cost savings of 70% over conventional uRANS methods.

7.1.3 Ground Effect

This research demonstrated that OVERFLOW-CHARM can be applied to rotor performance analysis at a range of scales where wake impingement on an external surface is present. Accuracy of integrated loads is within 6% of conventional uRANS methods. Best practices established in this analysis include the recommendation for blade chord-wise refinement of approximately 400 points, radial refinement of approximately 100 points, low-Mach number preconditioning with a β_{min} parameter of $3M_{ref}^2$, and the use of a non-contiguous uRANS domain and SGB simulation where appropriate. These advanced hybrid coupling approaches can be effectively employed for as much as 80% cost savings compared to pure uRANS approaches. The level of accuracy of OVERFLOW-CHARM predictions is the same as that of conventional uRANS predictions, generally within 10%, when compared to experimental data. These results establish confidence in OVERFLOW-CHARM's ability to be applied to shipboard landing scenarios where wake impingement on the ship deck is expected to impact rotor performance.

7.1.4 Ground Obstacles and Airwake Coupling

This demonstration of OVERFLOW-CHARM's application to analysis of the physics of the DI provides valuable insight into the capabilities of a state-of-the-art hybrid uRANS/free-wake solver for characterizing DI aerodynamics. OVERFLOW-CHARM can capture the fundamental physical features of the DI at approximately 85% less computational cost than conventional uRANS methods. The effect of DI interactions on unsteady fuselage loads are also correlated with those predicted by flight test data. Improvements to panel method settings in the free-wake solver are recommended to avoid intermittent non-physical solutions when blade tip vortices approach convex corners of solid bodies. One-way coupling of OVERFLOW-CHARM to a precomputed airwake database is highly cost efficient, with a less than 0.5% impact on the computational cost compared to uncoupled simulations. The precomputed the airwake can also be re-used for various helicopter positions or for different aircraft models, making it more efficient for routine DI analysis than a unified approach to DI simulation.

7.1.5 Final Conclusions

The state-of-the art in hybrid CFD solvers has been expanded from a class of niche research codes for idealized rotor analysis to a production-ready tool for analysis of a wide range of modern vertical lift aircraft configurations and conditions. This advanced solver has been applied to scenarios which contain physics relevant to the challenging problem of DI characterization, and its capabilities relative to standard CFD tools were quantified. The results of these studies establish the necessary capability and implementation requirements for hybrid uRANS/free-wake solvers to be a viable alternatives to conventional methods where high fidelity resolution of rotor wake physics and computational efficiency are both essential requirements.

7.2 Recommendations for Future Work

7.2.1 Resolve Limitations of Potential Solver

Some limitations in the CHARM library utilized in the OVERFLOW-CHARM code have resulted in some unnecessary capability limitations of OVERFLOW-CHARM. An advancement in the CHARM solution methodology is suggested which could enhance the accuracy of OVERFLOW-CHARM simulations.

CHARM Restart Capability

The ability to restart numerical simulations that require long wall clock times is essential for a smooth workflow. Restart capability provides analysts with the ability to correct mistakes, alter conditions, and initialize solutions without the need to re-compute the entire solution history. While CHARM was originally developed to provide fast turn-around times or real-time simulation capabilities, it's role as a part of a hybrid uRANS/free-wake framework necessitates the inclusion of solution restart capability if OVERFLOW-CHARM is to be adopted into existing workflows.

Dynamic Evaluation Point Allocation

The CHARM module provides the capability to dynamically allocate evaluation points as the simulation progresses, which permits some of the novel features of OVERFLOW-CHARM like CHARM-induced uRANS solution initialization and cost-effective flow field visualization. This capability has not been implemented for airwake-coupled CHARM operation, however, and thus the aforementioned OVERFLOW-CHARM features are not possible when an external airwake is employed. While flow field visualization can still be performed, it requires the evaluation of induced velocities on the visualization points at every CHARM step, including during CHARM initialization, which incurs some additional computational cost. The ability to initialize the uRANS solution to CHARM-induced values was also demonstrated to reduce initial transients in the uRANS solution, which is important when correlating data early in the simulation to flight test data.

Improve CHARM Temporal Resolution

During this research, much effort was expended towards resolving the discrepancy between time steps of OVERFLOW and CHARM through two different interpolation methods. Both of these methods assume that exact CHARM-induced velocities are only available at intermittent time steps during the simulation. Ideally, exact CHARM-induced velocities would be available at every uRANS time step, or at least at a customizable interval to improve the accuracy of interpolation. However, decreasing the CHARM time step requires releasing smaller and smaller wake elements, which drives up the computational expense of all CHARM functions and results in instability in the CHARM solution. If the CHARM time step could be decreased without impacting the number of wake elements, the temporal accuracy of the OVERFLOW-CHARM boundary condition could be improved. One suggested technique is to split CHARM time steps into primary and secondary time steps. At primary time steps, the functionality of CHARM would be as normal, where new wake elements are created at the blade and all wake elements are convected based on the new solution. At secondary time steps, no new wake elements would be created, but the wake would still be allowed to convect. For certain applications where the time to compute one CHARM step is significantly smaller than the time required to compute an OVERFLOW step, this would allow much higher temporal resolution at the OVERFLOW-CHARM boundary condition while adding minimal additional computational cost.

Allow Asynchronous Rotors

As OVERFLOW-CHARM modeling of the DI becomes more sophisticated, the resolution of the tail rotor will become necessary for accurate prediction vehicle of the aircraft dynamics. Currently the CHARM Wake/Panel Module that is utilized within OVERFLOW-CHARM requires the rotation speeds of modeled rotors to be integer multiples of the primary rotor speed. Techniques should be developed that either directly address this limitation or adapt around it to enable the inclusion of the tail rotor in OVERFLOW-CHARM simulations of the DI.

7.2.2 Suggested Improvements to OVERFLOW-CHARM Coupling Framework

While extensive improvements have been made to the OVERFLOW-CHARM coupling interface relative to its capabilities prior to this research, there are opportunities for additional expansions to meet the needs of DI and Advanced Air Mobility (AAM) analysis.

Add Vehicle/Ship Relative Motion and Flight Dynamics Coupling

To properly assess pilot workload, better more detailed analysis of the helicopter dynamics is necessary beyond inspecting the fuselage loads. A major advantage of computational modeling over wind tunnel testing is the ability to include a pilot model in the simulations. To achieve this capability, the coupling interface should first to be validated for cases that include relative motion of the helicopter and ship. It is recommended that this simple update be validated using the dynamic test points of the Elevated Fixed Platform (EFP) Low-Speed Object-Induced Downwash Recirculation (LOIDR) flight tests discussed in the previous chapter. Then, coupling to flight dynamics software should be developed so that OVERFLOW-CHARM can provide direct predictions of pilot response in the DI and pilot workload can be quantified

Implement Blade-Element Model to Initialize Rotor Loads

Initializing the CHARM wake in an OVERFLOW-CHARM wake currently requires an input file containing an estimate of the rotor loads. While these can be precomputed from a uRANS simulation, a previous OVERFLOW-CHARM simulation, or through an analytical script, it would be convenient for the user to have an option of computing these loads at run time by employing a blade element or other momentum-theory-based model of the rotor.

Enhance Airwake Coupling

While the airwake coupling method employed in this research was sufficient for this initial implementation and is highly computationally efficient, the general coupling approach permits much more advanced modeling of the airwake's impact on the CHARM solution. For example, implementing a vortex particle representation of the airwake may result in more accurate aerodynamic interactions between the airwake and rotor wake and improve the accuracy of OVERFLOW-CHARM predictions of the DI.

Fully Implement Helios Coupling for Aeroelastic and Aircraft Trim Capabilities

OVERFLOW-CHARM was implemented as a near-body solver in HPCMP CREATE™-AV Helios in a related effort. This permits coupling to all of the tools available in Helios, including the structural solver Rotorcraft Comprehensive Analysis System (RCAS). This capability, including more recent improvements to OVERFLOW-CHARM should be validated with updated predictions of rotor aeroelasticity similar to the analysis of Wilbur et al. [128].

Fully Parallel CHARM computation

The implementation of Force-Predictive Interpolation (FPI) has demonstrated that the CHARM and OVERFLOW solutions can be updated asynchronously. This fact could be leveraged to address less than optimal parallel scaling of OVERFLOW-CHARM when large numbers of wake elements are present in the simulation. The most costly CHARM procedure is the Biot-Savart computation of induced velocities. The cost of this procedure is proportional to $n \times n + n \times m$, where n is the number of vortex elements (filaments or panels in the CHARM model) and m is the number of boundary points on any particular processor. When n is larger than m, the second term dominates the computational cost, and it is efficient to compute induced velocities directly on the local processor. This is the case for simple rotor configurations where only a small number of wake elements and panels are required. For full vehicle analysis, or when the uRANS boundary points are clustered onto a small number of processors, n is typically larger than m, and it would be more efficient to reserve one processor that computes the CHARM solution and induced velocities on all boundary points while the OVERFLOW solution progresses. This capability would only be valid for FPI, so significant development would be required for its implementation.

7.2.3 Recommended Expansion of DI Analysis

Expand Correlation of Simulations to Flight Test Data

Due to the unavailability of critical metadata in the flight test data, much of it was unable to be correlated to simulated results. When the flight test data is ready to be fully processed, OVERFLOW-CHARM simulations of the LOIDR configuration should be further validated with flight test aircraft motion, pilot control inputs, Stability Augmentation System (SAS) signals, and anemometer data. In particular, this data should be utilized to identify the cause of the over-prediction of high-frequency longitudinal events observed in the OVERFLOW-CHARM simulations at the sideslip condition.

Quantify Effects of Various OVERFLOW-CHARM Modeling Approaches

While this research extends the capabilities of hybrid approaches such as OVERFLOW-CHARM to the DI problem using best practices established in previous chapters, further optimization of modeling options in OVERFLOW-CHARM should be performed to identify any effects specific to DI analysis.

Investigate Capabilities for Dynamic Aircraft Motion

To better match flight test data and simulate full shipboard landing trajectories, OVERFLOW-CHARM must be able to handle relative body motion. While this capability is present in both OVERFLOW and CHARM separately, it has not yet been attempted with OVERFLOW-CHARM. Small modifications to the coupling interface may be required to communicate the necessary information when relative motion is present, which should be validated with an experiment where relative body motion plays an important role in the flow field aerodynamics.

REFERENCES

[1] Michael Roscoe and Colin Wilkinson. *DIMSS–JSHIP's M&S Process for Ship/Helicopter Testing & Training*. AIAA Paper, AIAA-2002-4597, AIAA Modeling and Simulation Technologies Conference and Exhibit, Monterey, California. Aug. 2002.

[2] Bruce R. Lumsden, Colin H. Wilkinson, and Gareth D. Padfield. "Challenges at the Helicopter-Ship Dynamic Interface". In: *Proceedings of the 24th European Rotorcraft Forum*. 2. Council of European Aerospace Societies. Marseilles, France, Sept. 1998.

[3] Sunjoo K. Advani and Colin H. Wilkinson. "Dynamic Interface Modelling and Simulation - A Unique Challenge". In: *Proceedings of the Royal Aeronautical Society Conference on Heliocopter Flight Simulation*. Royal Aeronautical Society. London, United Kingdom, Nov. 2001.

[4] Wajih A. Memon, Ieuan Owen, and Mark D. White. "Motion Fidelity Requirements for Helicopter-Ship Operations in Maritime Rotorcraft Flight Simulators". In: *Journal of Aircraft* 56.6 (Nov. 2019), pp. 2189–2209.

[5] Mark J. Silva and James K. Barber. *Truth Data for DIVE V&V*. AIAA Paper, AIAA-2021-2482, AIAA AVIATION Forum 2021, Virtual Event. Aug. 2021.

[6] Murray Snyder et al. *USNA Ship Air Wake Program Overview*. AIAA Paper, AIAA-2011-3153, 29th AIAA Applied Aerodynamics Conference, Honolulu, Hawaii. June 2011.

[7] Luksa Luznik et al. "Influence of the Atmospheric Surface Layer on a Turbulent Flow Downstream of a Ship Superstructure". In: *Journal of Atmospheric and Oceanic Technology* 30.8 (Aug. 2013), pp. 1803–1819.

[8] Cody J. Brownell et al. "In Situ Velocity Measurements in the Near-Wake of a Ship Superstructure". In: *Journal of Aircraft* 49.5 (Sept. 2012), pp. 1440–1450.

[9] William Reddy, Jr. *Ship Airwake Measurement and Flow Visualization*. AIAA Paper, AIAA-92-4088-CP, 6th AIAA Biennial Flight Test Conference, Hilton Head, South Carolina. Aug. 1992.

[10] Alan W. Schwartz et al. *Experimental Investigation of Aerodynamic Interactions During Shipboard Lauch & Recovery of Unconventional UAVs*. AIAA Paper, AIAA-2021-1536, AIAA SCITECH 2021 Forum, Virtual Event. Jan. 2021.

[11] Theodore S. Garnett Jr. *Investigation to Study the Aerodynamic Ship Wake Turbulence Generated by a DD963 Destroyer*. Tech. rep. 77-214-30. NADC, Oct. 1979.

[12] Michael K. Johns. "Flow Visualization of the Airwake Around a Model of a DD-963 Class Destroyer in a Simulated Atmospheric Boundary Layer". https://calhoun.nps.edu/handle/10945/23240. MA thesis. Monterey, California: Naval Postgraduate School, Sept. 1988.

[13] P. R. Kulkarni, S. N. Singh, and Seshadri V. "Flow Visualization Studies of Exhaust Smoke-Superstructure Interaction on Naval Ships". In: *Naval Engineers Journal* 117.1 (Jan. 2005), pp. 41–56.

[14] R Vijayakumar et al. "A Wind Tunnel Study on the Interaction of Hot Exhaust from the Funnel with the Superstructure of a Naval Ship". In: *Proceedings of OCEANS 2008 - MTS/IEEE Kobe Techno-Ocean*. 978-1-4244-2126. IEEE Oceanic Engineering Society. Kobe, Japan, Apr. 2008.

[15] M. M. Rhoades and J. Val. Healey. "Flight Deck Aerodynamics of a Nonaviation Ship". In: *Journal of Aircraft* 29.4 (July 1992), pp. 619–626.

[16] William H. III Daley. "Flow Visualization of the Airwake Around a Model of a TARAWA Class LHA in a Simulated Atmospheric Boundary Layer". https://calhoun.nps.edu/handle/10945/23238. MA thesis. Monterey, California: Naval Postgraduate School, June 1988.

[17] Rafael Mora. "Experimental Investigation of the Flow on a Simple Frigate Shape (SFS)". In: *The Scientific World Journal* 2014 (Jan. 2014), p. 818132.

[18] Dhuree Seth et al. "Time-Resolved Ship Airwake Measurements in a Simulated Atmospheric Boundary Layer". In: *Journal of Aircraft* 58.3 (May 2021), pp. 624–649.

[19] Ebenezer P. Gnanamanickam et al. *Structure of the Ship Airwake in a Simulated Atmospheric Boundary Layer*. AIAA Paper, AIAA-2020-2702, AIAA AVIATION Forum 2020, Virtual Event. June 2020.

[20] Nicholas Zhu et al. *Dynamics of Large-Scale Flow Structures in Ship Airwakes*. AIAA Paper, AIAA-2022-2532, AIAA SCITECH 2022 Forum, San Diego, California. Jan. 2022.

[21] S. Zan, Jerry Syms, and B. Cheney. "Analysis of Patrol Frigate Air Wakes". In: *Proceedings of the NATO RTO Symposium on Fluid Dynamics Problems of Vehicles Operating near or in the Air-Sea Interface*. NATO Research and Technology Organization. Oct. 1998.

[22] David B. Findlay and Terence A. Ghee. *Experimental Investigation of Ship Airwake Flow Control for a US Navy Flight II-A Class Destroyer (DDG)*. AIAA Paper, AIAA-2006-3501, 3rd AIAA Flow Control Conference, San Francisco, California. June 2006.

[23] Daniel M. Shafer and Terence A. Ghee. *Active and Passive Flow Control over the Flight Deck of Small Naval Vessels*. AIAA Paper, AIAA-2005-5265, 35th AIAA Fluid Dynamics Conference and Exhibit, Toronto, Canada. June 2005.

[24] S. Polsky. *A Computational Study of Unsteady Ship Airwake*. AIAA Paper, AIAA-2002-1022, 40th AIAA Aerospace Sciences Meeting and Exhibit, Reno, Nevada. Jan. 2002.

[25] G. F. Syms. "Numerical Simulation of Frigate Airwakes". In: *International Journal of Computational Fluid Dynamics* 18.2 (Feb. 2004), pp. 199–207.

[26] Anupam Sharma and Lyle Long. *Airwake Simulations on an LPD 17 Ship*. AIAA Paper, AIAA-2001-2589, 15th AIAA Computational Fluid Dynamics Conference, Anaheim, California. June 2001.

[27] N. Sezer-Uzol, A. Sharma, and L. N. Long. "Computational Fluid Dynamics Simulations of Ship Airwake". In: *Proceedings of the Institution of Mechanical Engineers, Part G: Journal of Aerospace Engineering* 219.5 (May 2005), pp. 369–392.

[28] Zhao Rui et al. "Entropy-Based Detached-Eddy Simulation of the Airwake Over a Simple Frigate Shape". In: *Advances in Mechanical Engineering* 7.11 (Nov. 2015), p. 1687814015616930.

[29] G.F. Syms. "Simulation of Simplified-Frigate Airwakes Using a Lattice-Boltzmann Method". In: *Journal of Wind Engineering and Industrial Aerodynamics* 96.6 (June 2008). 5th International Colloquium on Bluff Body Aerodynamics and Applications, pp. 1197–1206.

[30] K.R. Reddy, R. Toffoletto, and K.R.W. Jones. "Numerical Simulation of Ship Airwake". In: *Computers and Fluids* 29.4 (May 2000), pp. 451–456.

[31] Martin Guillot and Monica Walker. *Unsteady Analysis of the Air Wake Over the LPD-17*. AIAA Paper, AIAA-2000-4125, 18th Applied Aerodynamics Conference, Denver, Colorado. Aug. 2000.

[32] Jacob van Muijden et al. *Computational Ship Airwake Determination to Support Helicopter-Ship Dynamic Interface Assessment*. AIAA Paper, AIAA-2013-3078, 21st AIAA Computational Fluid Dynamics Conference, San Diego, California. June 2013.

[33] Ryan M. Czerwiec, Bradford E. Green, and Susan A. Polsky. *CREATE Kestrel CFD Predictions of LPD 17 Airwake with Comparisons to Wind Tunnel Data*. AIAA Paper, AIAA-2021-2479, AIAA AVIATION Forum 2021, Virtual Event. Aug. 2021.

[34] Susan A. Polsky and Terence A. Ghee. "Application and Verification of Internal Boundary Conditions for Antenna Mast Wake Predictions". In: *Journal of Wind Engineering and Industrial Aerodynamics* 96.6–7 (June 2008). 5th International Colloquium on Bluff Body Aerodynamics and Applications, pp. 817–830.

[35] B. Thornber, M. Starr, and D. Drikakis. "Implicit Large Eddy Simulation of Ship Airwakes". In: *The Aeronautical Journal (1968)* 114.1162 (Dec. 2010).

[36] James S. Forrest and Ieuan Owen. "An Investigation of Ship Airwakes Using Detached-Eddy Simulation". In: *Computers and Fluids* 39.4 (Apr. 2010), pp. 656–673.

[37] Jeremy Shipman et al. *Ship Airwake Sensitivities to Modeling Parameters*. AIAA Paper, AIAA-2005-1105, 43rd AIAA Aerospace Sciences Meeting and Exhibit, Reno, Nevada. Jan. 2005.

[38] James R. Forsythe et al. *Coupled Flight Simulator and CFD Calculations of Ship Airwake using Kestrel*. AIAA Paper, AIAA-2015-0556, 53rd AIAA Aerospace Sciences Meeting, Kissimmee, Florida. Jan. 2015.

[39] D. Lee and J. F. Horn. "Simulation of Pilot Workload for a Helicopter Operating in a Turbulent Ship Airwake". In: *Proceedings of the Institution of Mechanical Engineers, Part G: Journal of Aerospace Engineering* 219.5 (May 2005), pp. 445–458.

[40] Derek Bridges et al. *Coupled Flight Dynamics and CFD Analysis of Pilot Workload in Ship Airwakes*. AIAA Paper, AIAA-2007-6485, AIAA Atmospheric Flight Mechanics Conference and Exhibit, Hilton Head, South Carolina. Aug. 2012.

[41] Charles Tinney and Lawrence Ukeiley. "A Study of a 3-D Double Backward-Facing Step". In: *Experiments in Fluids* 47.3 (Sept. 2009), pp. 427–438.

[42] Regis Thedin, Michael P. Kinzel, and Sven Schmitz. "An Evaluation of the Effects of Resolved Shear-Driven Atmospheric Turbulence on Ship Airwakes". In: *Journal of the American Helicopter Society* 63.2 (Apr. 2018), pp. 1–16.

[43] Regis Thedin et al. "Coupled Simulations of Atmospheric Turbulence-Modified Ship Airwakes and Helicopter Dynamics". In: *Journal of Aircraft* 57.3 (May 2020), pp. 534–546.

[44] Regis Thedin et al. “Effects of Atmospheric Turbulence Unsteadiness on Ship Airwakes and Helicopter Dynamics”. In: *Journal of Aircraft* 57.3 (May 2020), pp. 534–546.

[45] Susan Polsky. *CFD Prediction of Airwake Flowfields for Ships Experiencing Beam Winds*. AIAA Paper, AIAA-2003-3657, 21st AIAA Applied Aerodynamics Conference, Orlando, Florida. June 2003.

[46] Jeremy D. Shipman and Jonghoon Bin. *Atmospheric Boundary Layer Turbulence Simulation for Ship Airwake CFD Applications*. AIAA Paper, AIAA-2021-2481, AIAA AVIATION Forum 2021, Virtual Event. Aug. 2021.

[47] Colin Wilkinson, Gery VanderVliet, and Michael Roscoe. “Modeling and Simulation of the Ship-Helicopter Environment”. In: *Proceedings of the Modeling and Simulation Technologies Conference*. AIAA-2000-4583. American Institute of Aeronautics and Astronautics Inc. Denver, CO, Aug. 2000.

[48] Stargel R. Doane and Drew Landman. *A Wind Tunnel Investigation of Ship Airwake/Rotor Downwash Coupling using Design of Experiments Methodologies*. AIAA Paper, AIAA-2012-0767, 50th AIAA Aerospace Sciences Meeting including the New Horizons Forum and Aerospace Exhibition, Nashville, Tennessee. Jan. 2012.

[49] Chen Friedman, Julie Duplessis, and Murray Snyder. *Measurements of Dynamic Interface Between Ship and Helicopter Air Wakes*. AIAA Paper, AIAA-2016-0039, 54th AIAA Aerospace Sciences Meeting, San Diego, California. Jan. 2016.

[50] Richard G. Lee and Steven J. Zan. “Unsteady Aerodynamic Loading on a Helicopter Fuselage in a Ship Airwake”. In: *Journal of the American Helicopter Society* 49.2 (Apr. 2004), pp. 149–159.

[51] S. J. Zan. “Experimental Determination of Rotor Thrust in a Ship Airwake”. In: *Journal of the American Helicopter Society* 47.2 (Apr. 2002), pp. 100–108.

[52] Christopher H. Kääriä et al. “Aerodynamic Loading Characteristics of a Model-Scale Helicopter in a Ship’s Airwake”. In: *Journal of Aircraft* 49.5 (Sept. 2012), pp. 1271–1278.

[53] Yaxing Wang et al. “AirDyn: An Instrumented Model-Scale Helicopter for Measuring Unsteady Aerodynamic Loading in Airwakes”. In: *Measurement Science and Technology* 22.4 (Mar. 2011), p. 045901.

[54] S. J. Zan. “On Aerodynamic Modelling and Simulation of the Dynamic Interface”. In: *Proceedings of the Institution of Mechanical Engineers, Part G: Journal of Aerospace Engineering* 219.5 (May 2005), pp. 393–410.

[55] Fidel Khouli, Fred F. Afagh, and Robert G. Langloi. "Design, Simulation, and Experimental Results for Flexible Rotors in a Ship Airwake". In: *Journal of Aircraft* 53.1 (Sept. 2016), pp. 262–275.

[56] Richard G. Lee and Steven J. Zan. "Wind Tunnel Testing of a Helicopter Fuselage and Rotor in a Ship Airwake". In: *Journal of the American Helicopter Society* 50.4 (Oct. 2005), pp. 326–337.

[57] P Tattersall et al. "Prediction of Ship Air Wakes over Flight Decks using CFD". In: *Proceedings of the NATO RTO Applied Vehicle Technology Panel (AVT) Symposium on Fluid Dynamics Problems of Vehicles Operating Near or in the Air-Sea Interface*. 1. NATO Research and Technology Organization. Amsterdam, The Netherlands, Oct. 1988.

[58] Emre Alpman et al. "Fully-Coupled Simulations of the Rotorcraft / Ship Dynamic Interface". In: *Proceedings of the American Helicopter Society 63rd Annual Forum*. 63-2007-000206. Virginia Beach, Virginia: American Helicopter Society Inc., Aug. 2007.

[59] C. Crozon, R. Steijl, and G. N. Barakos. "Numerical Study of Helicopter Rotors in a Ship Airwake". In: *Journal of Aircraft* 51.6 (Nov. 2014), pp. 1813–1832.

[60] C. Crozon, R. Steijl, and G.N. Barakos. "Coupled Flight Dynamics and CFD – Demonstration for Helicopters in Shipborne Environment". In: *The Aeronautical Journal* 122.1247 (Nov. 2018), pp. 42–82.

[61] Auriane Bottai et al. "Fully Coupled Flight Dynamics/CFD Simulations of a Helicopter with Actuator Disk Models for the Main Rotor and Tail Rotor". In: *Proceedings of the American Helicopter Society Technical Conference on Aeromechanics Design for Transformative Vertical Flight*. sm_aeromech_2018_03. American Helicopter Society Inc. San Francisco, California, Jan. 2018.

[62] Alexandra Landsberg et al. *Analysis of the Nonlinear Coupling Effects of a Helicopter Downwash With an Unsteady Ship Airwake*. AIAA-95-0047, 33rd Aerospace Sciences Meeting and Exhibit, Reno, Nevada. Jan. 1995.

[63] Ilker Oruc et al. "Towards Real-Time Fully Coupled Flight Dynamics and CFD Simulations of the Helicopter/Ship Dynamic Interface". In: *Proceedings of the American Helicopter Society 72nd Annual Forum*. 72-2016-131. American Helicopter Society Inc. West Palm Beach, Florida, May 2016.

[64] Susan A. Polsky. "Progress Towards Modeling Ship/Aircraft Dynamic Interface". In: *Proceedings of the 2006 HPCMP Users Group Conference (HPCMP-UGC'06)*. 9398888. United States Department of Defence High Performance Computing Modernization Program. Denver, Colorado, June 2006.

[65] Kyle A. Schau, Gopal H. Gaonkar, and Susan A. Polsky. “Helicopter Downwash Effects on Ship Airwake: Predictions, Modeling from a Database, and Simulation”. In: *Proceedings of the American Helicopter Society 70th Annual Forum*. 70-2014-0173. American Helicopter Society Inc. Montréal, Canada, May 2014.

[66] N. H. Wakefield, Newman S. J., and Wilson P. A. “Helicopter Flight Around a Ship’s Superstructure”. In: *Proceedings of the Institution of Mechanical Engineers, Part G: Journal of Aerospace Engineering* 216.1 (Jan. 2002), pp. 13–28.

[67] Yongjie Shi et al. “An Investigation of Coupling Ship/Rotor Flowfield Using Steady and Unsteady Rotor Methods”. In: *Engineering Applications of Computational Fluid Mechanics* 11.1 (Apr. 2017), pp. 417–434.

[68] Ilker Oruc et al. “Coupled Flight Dynamics and CFD Simulations of the Helicopter/Ship Dynamic Interface”. In: *Proceedings of the American Helicopter Society 71st Annual Forum*. 71-2015-283. American Helicopter Society Inc. Virginia Beach, Virginia, Jan. 2015.

[69] Daniel Linton and Ben Thornber. *An Actuator Surface Method for Ship-Helicopter Dynamic Interface Simulations*. AIAA Paper, AIAA-2021-1828, AIAA Scitech 2021 Forum, Virtual Event. Jan. 2021.

[70] Jakob Bludau et al. *Real-Time Simulation of Dynamic Inflow Using Rotorcraft Flight Dynamics Coupled With a Lattice-Boltzmann Based Fluid Simulation*. AIAA Paper, AIAA-2017-0050, 55th AIAA Aerospace Sciences Meeting, Grapevine, Texas. Jan. 2017.

[71] Bastian Horvat, Manfred Hajek, and Juergen Rauleder. *Analysing Rotorcraft Vortex Encounter Methods with a Lattice-Boltzmann Method Based GPU Framework*. AIAA Paper, AIAA-2020-0539, AIAA Scitech 2020 Forum, Orlando, Florida. Jan. 2020.

[72] Andreas Lintermann and Wolfgang Schröder. “Lattice–Boltzmann Simulations for Complex Geometries on High-Performance Computers”. In: *CEAS Aeronautical Journal* 11.3 (Sept. 2020), pp. 745–766.

[73] Aniruddhe Pradhan and Sumedh Yadav. “Large Eddy Simulation Using Lattice Boltzmann Method Based on Sigma Model”. In: *Procedia Engineering* 127.1 (Nov. 2015). International Conference on Computational Heat and Mass Transfer (ICCHMT)–2015, pp. 177–184.

[74] N. Frapolli, S. S. Chikatamarla, and I. V. Karlin. “Entropic Lattice Boltzmann Model for Gas Dynamics: Theory, Boundary Conditions, and Implementation”. In: *Physical Review E* 93.6 (June 2016), p. 063302.

[75] NASA. *Vortex-Lattice Utilization in Aeronautical Engineering and Aircraft Design*. Tech. rep. NASA-SP-405. NASA, May 1976.

[76] Donald B. Bliss, Milton E. Tenske, and Todd R. Quackenbush. *A New Methodology for Free Wake Analysis Using Curved Vortex Elements*. Tech. rep. NASA-CR-3958. NASA, Dec. 1987.

[77] Robert M. McKillip Jr. et al. "Dynamic Interface Simulation Using a Coupled Vortex-Based Ship Airwake and Rotor Wake Model". In: *Proceedings of the American Helicopter Society 58th Annual Forum*. 58-2002-00058. American Helicopter Society Inc. Montréal, Canada, May 2002.

[78] Dooyong Lee et al. "Simulation of Helicopter Shipboard Launch and Recovery with Time-Accurate Airwakes". In: *Journal of Aircraft* 42.2 (Mar. 2005), pp. 448–461.

[79] Susan Polsky and Stephen Naylor. *CVN Airwake Modeling and Integration: Initial Steps in the Creation and Implementation of a Virtual Burble for F-18 Carrier Landing Simulations*. AIAA Paper, AIAA-2005-6298, AIAA Modeling and Simulation Technologies Conference and Exhibit, San Francisco, California. Aug. 2005.

[80] Dooyong Lee et al. *Simulation of Pilot Control Activity During Helicopter Shipboard Operations*. AIAA Paper, AIAA-2003-5306, AIAA Atmospheric Flight Mechanics Conference and Exhibit, Austin, Texas. Aug. 2003.

[81] John Bunnell. *An Integrated Time-Varying Airwake in a UH-60 Black Hawk Shipboard Landing Simulation*. AIAA Paper, AIAA-2001-4065, AIAA Modeling and Simulation Technologies Conference and Exhibit, Montréal, Canada. Aug. 2001.

[82] S. J. Zan. "Analysis of Rotor Forces in a Ship Airwake". In: *Proceedings of the 75th AGARD FDP Meeting on Aerodynamics and Aeroacoustics of Rotorcraft*. 153693. Advisory Group for Aerospace Research and Development Fluid Dynamics Panel. Berlin, Germany, Oct. 1994.

[83] D.M. Roper et al. "Integrating CFD and Piloted Simulation to Quantify Ship-Helicopter Operating Limits". In: *CEAS Aeronautical Journal* 110.1109 (July 2006), pp. 419–428.

[84] Abhinav Sharma. "Development and Application of a Comprehensive Simulation for Modeling Helicopter Ship Landing". https://deepblue.lib.umich.edu/handle/2027.42/153342. PhD thesis. Ann Arbor, Michigan: University of Michigan, Dec. 2019.

[85] C.H. Kääriä, James Forrest, and Ieuan Owen. "Using Flight Simulation to Improve Ship Designs for Helicopter Operations". In: *Proceedings of the RINA International*

Conference on Computer Applications in Shipbuilding, Vol. 2. 8. Royal Institution of Naval Architects. Trieste, Italy, Sept. 2011.

[86] James Forrest, C.H. Kääriä, and Ieuan Owen. "Evaluating Ship Superstructure Aerodynamics for Maritime Helicopter Operations Through CFD and Flight Simulation". In: *CEAS Aeronautical Journal* 120.1232 (Oct. 2016), pp. 1578–1603.

[87] C. Kääriä, James Forrest, and Ieuan Owen. "The Virtual AirDyn: A Simulation Technique for Evaluating the Aerodynamic Impact of Ship Superstructures on Helicopter Operations". In: *CEAS Aeronautical Journal* 117.1233 (Dec. 2013), pp. 1233–1248.

[88] Susan A. Polsky et al. *Development and Application of the SAFEDI Tool for Virtual Dynamic Interface Ship Airwake Analysis*. AIAA Paper, AIAA-2016-1771, 54th AIAA Aerospace Sciences Meeting, San Diego, CA. Jan. 2016.

[89] J. P. Boris et al. "New Insights Into Large Eddy Simulation". In: *Fluid Dynamics Research* 10.4 (Dec. 1992), pp. 199–228.

[90] Yin Yu et al. *Reduced-Order Modeling of Ship Airwakes with Atmospheric Turbulence Effects using Dynamic Graph Networks*. AIAA Paper, AIAA-2022-2533, AIAA SCITECH 2022 Forum, San Diego, California. Jan. 2022.

[91] Andrew M. Wissink et al. "A Dual-Mesh Unstructured Adaptive Cartesian Computational Fluid Dynamics Approach for Hover Prediction". In: *Journal of the American Helicopter Society* 61.1 (Jan. 2016), pp. 1–19.

[92] Richard E. Brown and Andrew J. Line. "Efficient High-Resolution Wake Modeling Using the Vorticity Transport Equation". In: *AIAA Journal* 43.7 (July 2005), pp. 1434–1443.

[93] Glen R. Whitehouse et al. "Novel Eulerian Vorticity Transport Wake Module for Rotorcraft Flow Analysis". In: *Proceedings of the American Helicopter Society 58th Annual Forum*. 58-2002-00026. American Helicopter Society Inc. Virginia Beach, Virginia, May 2007.

[94] Eliot Quon et al. "Hierarchical Variable Fidelity Methods for Rotorcraft Aerodynamic Design and Analysis". In: *Proceedings of the American Helicopter Society 67th Annual Forum*. 67-2011-000309. American Helicopter Society Inc. Virginia Beach, Virginia, Jan. 2011.

[95] Eliot W. Quon et al. "Unsteady Reynolds-Averaged Navier-Stokes-Based Hybrid Methodologies for Rotor-Fuselage Interaction". In: *Journal of Aircraft* 49.3 (May 2012), pp. 961–965.

[96] Marilyn J. Smith et al. “Investigation of Ship Airwakes Using a Hybrid Computational Methodology”. In: *Proceedings of the American Helicopter Society 67th Annual Forum*. 70-2014-0171. American Helicopter Society Inc. Montréal, Canada, May 2014.

[97] Chengjian He and Jinggen Zhao. “Modeling Rotor Wake Dynamics with Viscous Vortex Particle Method”. In: *AIAA Journal* 47.4 (Apr. 2009), pp. 902–915.

[98] P. Anusonti-Inthra. *Developments and Validations of Fully Coupled CFD and Particle Vortex Transport Method for High-Fidelity Wake Modeling in Fixed and Rotary Wing Applications*. Tech. rep. NASA/CR-2010-216696. NASA, May 2010.

[99] Jinggen Zhao and Chengjian He. “A Hybrid Solver with Combined CFD and Viscous Vortex Particle Method”. In: *Proceedings of the American Helicopter Society 67th Annual Forum*. 67-2011-000280. American Helicopter Society Inc. Virginia Beach, Virginia, May 2011.

[100] Jinggen Zhao and Chengjian He. “Coupled CSD/CFD and Viscous Vortex Particle Method for Rotorcraft Comprehensive Analysis”. In: *Proceedings of the American Helicopter Society 68th Annual Forum*. 68-2012-000215. American Helicopter Society Inc. Fort Worth, Texas, May 2012.

[101] Jinggen Zhao and Chengjian He. “Rotor Blade Structural Loads Analysis Using Coupled CSD/CFD/VVPM”. In: *Proceedings of the American Helicopter Society 69th Annual Forum*. 69-2013-040. American Helicopter Society Inc. Phoenix, Arizona, May 2013.

[102] Alex M. Moushegian et al. “Accurate and Flexible Formulation of a Dual-Solver Hybrid CFD Framework”. In: *Proceedings of the 47th European Rotorcraft Forum*. No. 88. Council of European Aerospace Societies. Virtual Event, Sept. 2021.

[103] K. B. Collins. “A Multi-Fidelity Framework for Physics Based Rotor Blade Simulation and Optimization”. https://smartech.gatech.edu/handle/1853/26481. PhD thesis. Atlanta, Georgia: Georgia Institute of Technology, Nov. 2008.

[104] T. Egolf et al. “A Hybrid CFD Method for Coaxial Rotor Performance Prediction in Forward Flight”. In: *Proceedings of the AHS Aeromechanics Specialists’ Conference 2010*. sm_aeromech_2010_EgolfTA. American Helicopter Society Inc. San Francisco, California, Jan. 2010.

[105] Po-Wei Chen and Lakshmi Sankar. “A Hybrid Navier Stokes-Free Wake Method for Modeling Tandem Rotors”. In: *Proceedings of the 7th Asian/Australian Rotorcraft Forum*. sm_arf_2018_aerodynamics_018. American Helicopter Society Inc. Jeju Island, Korea, Nov. 2018.

[106] Nischint Rajmohan. “Application of Hybrid Methodology to Rotors in Steady and Maneuvering Flight”. https://smartech.gatech.edu/handle/1853/34756. PhD thesis. Atlanta, Georgia: Georgia Institute of Technology, Aug. 2010.

[107] Sebastian Thomas, Shreyas Ananthan, and James D. Baeder. “Wake-Coupling CFD-CSD Analysis of Helicopter Rotors in Steady and Maneuvering Flight Conditions”. In: *Proceedings of the American Helicopter Society Aeromechanics Specialists Conference*. sm_aeromech_2010_ThomasS. American Helicopter Society Inc. San Francisco, California, Jan. 2010.

[108] Robert H. Nichols and Pieter G. Buning. *User’s Manual for OVERFLOW 2.3*. https://overflow.larc.nasa.gov/users-manual-for-overflow-2-3. NASA Langley Research Center. Hampton, VA, Mar. 2021.

[109] Todd R. Quackenbush et al. *Computation of Rotor Aerodynamic Loads in Forward Flight Using a Full-Span Free Wake Analysis*. Tech. rep. NASA-CR-177611. NASA, Oct. 1990.

[110] Jou-Young Choi, Matthew Summers, and John J. Corrigan. “Validation of CHARM Wake Methodology for Computation of Loads and Vibrations”. In: *Proceedings of the American Helicopter Society 65th Annual Forum*. 65-2009-000143. American Helicopter Society Inc. Grapevine, Texas, May 2009.

[111] Daniel A. Wachspress et al. “Helicopter Rotor Airload Predictions with a Comprehensive Rotorcraft Analysis”. In: *Proceedings of the American Helicopter Society 68th Annual Forum*. 68-2012-000157. American Helicopter Society Inc. Fort Worth, Texas, May 2012.

[112] Jeffrey D. Keller, Daniel A. Wachspress, and Jacques C. Hoffler. “Real Time Free Wake and Ship Airwake Model for Rotorcraft Flight Training Applications”. In: *Proceedings of the American Helicopter Society 71st Annual Forum*. 71-2015-275. American Helicopter Society Inc. Virginia Beach, Virginia, May 2015.

[113] Jeffrey D. Keller, Daniel A. Wachspress, and Jacques C. Hoffler. “Pilot Evaluation of a Real-Time Free Wake Model in a Rotorcraft Fleet Trainer”. In: *Proceedings of the American Helicopter Society 73rd Annual Forum*. 73-2017-0308. American Helicopter Society Inc. Fort Worth, Texas, May 2017.

[114] Jeffrey D. Keller et al. *Modular High Fidelity Real Time Rotor Wake Software for Modeling of Shipboard Interactions*. AIAA Paper, AIAA-2007-6618, AIAA Modeling and Simulation Technologies Conference and Exhibit, Hilton Head, South Carolina. Aug. 2007.

[115] Jeffrey D. Keller, Robert M. McKillip Jr., and Daniel. A. Wachspress. *Physical Modeling of Aircraft Upsets for Real-Time Simulation Applications*. AIAA Paper,

AIAA-2008-6205, AIAA Atmospheric Flight Mechanics Conference and Exhibit, Honolulu, Hawaii. Oct. 2008.

[116] Todd R. Quackenbush, Daniel A. Wachspress, and Christine L. Solomon. “Design Studies for Performance and Noise of VTOL UAV Rotors and Proprotors”. In: *Proceedings of the American Helicopter Society International Specialists’ Meeting on Unmanned Rotorcraft Design, Control, and Testing*. sm_uas_2007_028_Quackenbush. American Helicopter Society Inc. Chandler, Arizona, Jan. 2007.

[117] Todd R. Quackenbush et al. “Aeroacoustic Modeling of an eVTOL Slowed Rotor Winged Compound Aircraft”. In: *Proceedings of the Vertical Flight Society 75th Annual Forum*. 75-209-0408-Quackenbush. Vertical Flight Society Inc. Philadelphia, Pennsylvania, May 2019.

[118] Daniel A. Wachspress, Michael K. Yu, and Kenneth S. Brentner. “Rotor/Airframe Aeroacoustic Prediction for eVTOL UAM Aircraft”. In: *Proceedings of the Vertical Flight Society 75th Annual Forum*. 75-209-0352-Wachspress. Vertical Flight Society Inc. Philadelphia, Pennsylvania, May 2019.

[119] Todd R. Quackenbush et al. “Analysis Methods for Tilting Wing and Tailsitter e-VTOL Configurations”. In: *Proceedings of the Vertical Flight Society Autonomous VTOL Technical Meeting and Electric VTOL Symposium*. sm_8VTOL_2019_05_Quackenbush. Vertical Flight Society Inc. Mesa, Arizona, Jan. 2019.

[120] Steven Spoldi and Paul Ruckel. “High Fidelity Helicopter Simulation using Free Wake, Lifting Line Tail, and Blade Element Tail Rotor Models”. In: *Proceedings of the American Helicopter Society 59th Annual Forum*. 59-2003-000126. American Helicopter Society Inc. Phoenix, Arizona, May 2003.

[121] Daniel A. Wachspress, Todd R. Quackenbush, and Alexander H. Boschitsch. “Rotorcraft Interactional Aerodynamics Calculations with Fast Vortex/Fast Panel Methods”. In: *Proceedings of the American Helicopter Society 56th Annual Forum*. 56-00096. American Helicopter Society Inc. Virginia Beach, Virginia, May 2000.

[122] Todd R. Quackenbush, Donald B. Bliss, and Daniel A. Wachspress. “New Free-Wake Analysis of Rotorcraft Hover Performance Using Influence Coefficients”. In: *Journal of Aircraft* 26.12 (Dec. 1989), pp. 1090–1097.

[123] Glen R. Whitehouse, Daniel A. Wachspress, and Todd R. Quackenbush. *Predicting the Influence of Blade Tip Shape on Hovering Rotor Performance with Comprehensive Analyses*. AIAA Paper, AIAA-2015-1248, 53rd AIAA Aerospace Sciences Meeting, Kissimmee, Florida. Jan. 2015.

[124] Glen R. Whitehouse, Daniel A. Wachspress, and Todd R. Quackenbush. “Predicting the Influence of Blade Shape on Hover Performance with Comprehensive Analyses”. In: *Journal of Aircraft* 55.1 (Jan. 2018), pp. 111–121.

[125] Luigi Morino and Ching-Chiang Kuo. “Subsonic Potential Aerodynamics for Complex Configurations: A General Theory”. In: *AIAA Journal* 12.2 (Feb. 1974), pp. 191–197.

[126] Marilyn J. Smith et al. *Evaluation of Rotor Hover Performance With Differing Blade Tip Shapes Using A Carefree Hybrid Methodology*. AIAA Paper, AIAA-2015-1713, 53rd AIAA Aerospace Sciences Meeting, Kissimmee, Florida. Jan. 2015.

[127] Kevin E. Jacobson, Amanda Grubb, and Marilyn J. Smith. *Performance and Physics of a S-76 Rotor in Hover With Non-Contiguous Hybrid Methodologies*. AIAA Paper, AIAA-2016-0302, 54th AIAA Aerospace Sciences Meeting, San Diego, California. Jan. 2016.

[128] Isaac C. Wilbur et al. “UH-60A Rotor Analysis with an Accurate Dual-Formulation Hybrid Aeroelastic Methodology”. In: *Journal of Aircraft* 57.1 (Jan. 2020), pp. 113–127.

[129] Isaac C. Wilbur et al. “Complex Vehicle Design and Analysis with Hybrid Methodologies”. In: *Proceedings of the AHS Aeromechanics Design for Transformative Vertical Flight Meeting*. sm_aeromech_2018_44. American Helicopter Society Inc. San Francisco, California, Jan. 2018.

[130] Scott A. Morton et al. *Kestrel - A Fixed Wing Virtual Aircraft Product of the CREATE Program*. AIAA Paper, AIAA-2009-338, 47th AIAA Aerospace Sciences Meeting Including the New Horizons Forum and Aerospace Exposition, Orlando, Florida. Jan. 2009.

[131] David R. McDaniel and Scott A. Morton. *HPCMP CREATE(TM)-AV Kestrel Architecture, Capabilities, and Future Directions*. AIAA Paper, AIAA-2018-0025, 2018 AIAA Aerospace Sciences Meeting, Kissimmee, Florida. Jan. 2018.

[132] David R. McDaniel. *A Summary of New and Emerging Features in HPCMP CREATE(TM)-AV Kestrel*. AIAA Paper, AIAA-2021-0234, AIAA Scitech 2021 Forum, Virtual Event. Jan. 2021.

[133] David R. McDaniel et al. *Accuracy and Performance Improvements to Kestrel’s Near-Body Flow Solver*. AIAA Paper, AIAA-2016-1051, 54th AIAA Aerospace Sciences Meeting, San Diego, California. Jan. 2016.

[134] R. Forsythe James et al. *Fundamental Physics Validation Using HPCMP CREATE(TM)-AV Kestrel: Part II*. AIAA Paper, AIAA-2014-0919, 52nd AIAA Aerospace Sciences Meeting, National Harbor, Maryland. Jan. 2014.

[135] Marshall C. Galbraith et al. *Comparisons of HPCMP CREATE(TM)-AV Kestrel-COFFE, SU2, and MIT SANS RANS Solutions using Output-Based Adapted Meshes for a Multi-Element Airfoil*. AIAA Paper, AIAA-2021-1080, AIAA Scitech 2021 Forum, Virtual Event. Jan. 2021.

[136] David Stookesberry and Robert Narducci. *Industry Assessment of HPCMP CREATE(TM)-AV Kestrel*. AIAA Paper, AIAA-2015-0552, 53rd AIAA Aerospace Sciences Meeting, Kissimmee, Florida. Jan. 2015.

[137] Andrew M. Wissink et al. *Recent Advancements in the Helios Rotorcraft Simulation Code*. AIAA Paper, AIAA-2016-0563, 54th AIAA Aerospace Sciences Meeting, San Diego, California. Jan. 2016.

[138] Alex M. Moushegian et al. *Implementation of a Dual-Solver Hybrid Approach for Rotating System Simulations in HPCMP CREATE(TM)-AV HELIOS*. AIAA Paper, AIAA-2021-1077, AIAA Scitech 2021 Forum, Virtual Event. Jan. 2021.

[139] John R. Hooker et al. *Overview of Low Speed Wind Tunnel Testing Conducted on a Wingtip Mounted Propeller for the Workshop for Integrated Propeller Prediction*. AIAA Paper, AIAA-2020-2673, AIAA Aviation 2020 Forum, Virtual Event. June 2020.

[140] Pooneh Aref et al. *Comparison of Multi-Fidelity Prediction Methods for an Integrated Propeller*. AIAA Paper, AIAA-2021-2512, AIAA Aviation 2021 Forum, Virtual Event. Aug. 2021.

[141] Guido S. Baruzzi et al. *Numerical Simulation of an Integrated Propeller with Models of Progressively Increasing Fidelity*. AIAA Paper, AIAA-2020-2682, AIAA Aviation 2020 Forum, Virtual Event. June 2020.

[142] P. R. Spalart and S. R. Allmaras. “A One-Equation Turbulence Model for Aerodynamic Flows”. In: *La Recherche Aérospatiale* 1 (1994), pp. 5–21.

[143] F. R. Menter. “Two-Equation Eddy-Viscosity Turbulence Models for Engineering Applications”. In: *AIAA Journal* 32.8 (Aug. 1994), pp. 1598–1605.

[144] Pooneh Aref et al. *Application of the HPCMP CREATETM-AV Kestrel to the 1st AIAA Workshop for Integrated Propeller Prediction*. AIAA Paper, AIAA-2020-2674, AIAA Aviation 2020 Forum, Virtual Event. June 2020.

[145] Timothy E. Lee, J. Gordon Leishman, and Manikandan Ramasamy. “Fluid Dynamics of Interacting Blade Tip Vortices with a Ground Plane”. In: *Journal of the American Helicopter Society* 55.2 (Apr. 2010), p. 22005.

[146] Terry L. Holst and Thomas H. Pulliam. “Optimization of Overset Solution Adaptive Grids for Hovering Rotorcraft Flows”. In: *Proceedings of the American Helicopter Society Aeromechanics Specialists’ Conference*. sm_aeromech_2010_HolstT. American Helicopter Society Inc. San Francisco, California, Jan. 2010.

[147] Neal M. Chaderjian. “Advances in Rotor Performance and Turbulent Wake Simulation using DES and Adaptive Mesh Refinement”. In: *Proceedings of the Seventh International Conference on Computational Fluid Dynamics*. ICCFD7-1201. International Conference on Computational Fluid Dynamics. Big Island, Hawaii, July 2012.

[148] Tarandeep S. Kalra. “CFD Modeling and Analysis of Rotor Wake in Hover Interacting with a Ground Plane”. https://drum.lib.umd.edu/handle/1903/16086. PhD thesis. College Park, Maryland: University of Maryland, College Park, Dec. 2014.

[149] Kevin E. Jacobson and Marilyn J. Smith. “Carefree Hybrid Methodology for Rotor Hover Performance Analysis”. In: *Journal of Aircraft* 55.1 (Feb. 2018), pp. 52–65.

[150] Andrew M. Wissink et al. *Cartesian Adaptive Mesh Refinement for Rotorcraft Wake Resolution*. AIAA Paper, AIAA-2010-4554, 28th AIAA Applied Aerodynamics Conference, Chicago, Illinois. July 2010.

[151] Jonathan M. Weiss and Wayne A. Smith. “Preconditioning Applied to Variable and Constant Density Flows”. In: *AIAA Journal* 33.11 (Nov. 1995), pp. 2050–2057.

[152] Mark A. Potsdam, Venkatswaran Sankaran, and Shishir A. Pandya. *Unsteady Low Mach Preconditioning with Application to Rotorcraft Flows*. AIAA Paper, AIAA-2007-4473, 18th AIAA Computational Fluid Dynamics Conference, Miami, Florida. June 2007.

[153] Shishir A. Pandya, Sankaran Venkateswaran, and Thomas H. Pulliam. *Implementation of Preconditioned Dual-Time Procedures in OVERFLOW*. AIAA Paper, AIAA-2003-72, 41st Aerospace Sciences Meeting and Exhibit, Reno, Nevada. Jan. 2003.

[154] Thomas Renaud et al. “Evaluation of Isolated Fuselage and Rotor-Fuselage Interaction Using CFD”. In: *Proceedings of the American Helicopter Society 60th Annual Forum*. 60-2004-000079. American Helicopter Society Inc. Baltimore, Maryland, June 2004.

[155] D. T. Balch and J. Lombardi. *Experimental Study of Main Rotor Tip Geometry and Tail Rotor Interactions in Hover. Volume 1. Text and Figures*. Tech. rep. NASA-CR-177336-Vol-1. NASA, Feb. 1985.

[156] D. T. Balch and J. Lombardi. *Experimental Study of Main Rotor Tip Geometry and Tail Rotor Interactions in Hover. Volume 2. Run Log and Tabulated Data*. Tech. rep. NASA-CR-177336-Vol-2. NASA, Feb. 1985.

[157] Rohit Jain. "Hover Predictions for the S-76 Rotor with Tip Shape Variation Using CREATE-AV Helios". In: AIAA Paper, AIAA-2015-1244, 53rd Aerospace Sciences Meeting, Kissimmee, Florida. Jan. 2015.

[158] Helden Aerospace Corporation. *HeldenMesh User Manual, Version 3.08*. Helden Aerospace Corporation. Jan. 2020.

[159] *Helden Aerospace Website*. https://heldenaero.com/heldenmesh/. Accessed: 2022-03-24.

[160] Nalin A. Ratnayake et al. *Unstructured Grid Development for the Space Launch System Liftoff and Transition Lineloads Computational Analysis*. AIAA Paper, AIAA-2020-0672, AIAA SciTech Forum, Orlando, Florida. Jan. 2020.

[161] T. R. Quackenbush, A. H. Boschitsch, and D. A. Wachspress. "Fast Analysis Methods for Surface-Bounded Flows with Applications to Rotor Wake Modeling". In: *Proceedings of the American Helicopter Society 52nd Annual Forum*. American Helicopter Society Inc. Washington, D. C., June 1996.

VITA

Alex Moushegian was born on September 24, 1994 in McKinney, TX to Ken and Cindy Moushegian. He graduated summa cum laude from Rensselaer Polytechnic Institute in the spring of 2017 with a degree in aeronautical engineering. He received a Master's degree in aerospace engineering from the Georgia Institute of Technology in the spring of 2019 and continued work on his doctoral degree at Georgia Tech as a NAVAIR-sponsored SMART scholar until his graduation in the spring of 2022. He is subsequently working as an aerospace engineer at NAVAIR in Patuxent River, MD. He enjoys playing the guitar, piano, soccer, and strategy/competitive games in his spare time.